FACULTY
OF MATHEMATICS
AND PHYSICS
Charles University

DOCTORAL THESIS

Kristupas Kazimieras Tikuišis

Optical and magneto-optical properties of topological and Dirac materials

Department of Optoelectronics and Magneto-optics

Supervisor of the doctoral thesis:	RNDr. Martin Veis, Ph.D.
Study programme:	Quantum Optics and Optoelectronics
Study branch:	(P4F6)

Prague 2023

I declare that I carried out this doctoral thesis independently, and only with the cited sources, literature and other professional sources. It has not been used to obtain another or the same degree.

I understand that my work relates to the rights and obligations under the Act No. 121/2000 Sb., the Copyright Act, as amended, in particular the fact that the Charles University has the right to conclude a license agreement on the use of this work as a school work pursuant to Section 60 subsection 1 of the Copyright Act.

In .... date ....

Author's signature

May Charlotte always have a green salad to bite.

Title: Optical and magneto-optical properties of topological and Dirac materials

Author: Kristupas Kazimieras Tikuišis

Institute of Physics of Charles University: Department of Optoelectronics and Magneto-optics

Supervisor: RNDr. Martin Veis, Ph.D., Department of Optoelectronics and Magneto-optics

Advisers:
RNDr. Roman Antoš, Ph.D., Department of Optoelectronics and Magneto-optics;
Milan Orlita, Ph.D., National Laboratory of High Magnetic Fields LNCMI - Grenoble, CNRS (France)

Abstract: Dirac materials exhibit unusual properties that attract interest both for practical applications and fundamental reseach of exotic and relativistic physics. This thesis aims to systematically study basic optical and magneto-optical properties of several members of these materials, namely the lead tin salts crystalline topological insulators and graphene. Non-destructive experimental techniques of spectroscoipic ellipsometry and FTIR magneto-optical spectroscopy were used to perform measurements from IR to UV spectral regions. A four-band Hamiltonian model was derived to describe the most important band structure features of PbSnSe system placed in a magnetic field. This allowed to extract the band structure and topological parameters of the investigated samples. Extensive modeling results based on Kubo-Greenwood formalism and ab-initio simulations are presented to help validate the measurement results and predict the appearance of the topologically protected surface states. Despite excellent quality of the samples, the surface states were not observed, and the potential reasons are discussed. The epitaxial graphene grown by intercalation of graphitized silicon carbide offers a cheap and easily mass-produced source of graphene for novel optoelectronic devices. An efficient parametrised model dielectric function over a wide spectral region from IR to UV is presented. The spectral response in terms of the sharpness of the excitonic peak suggests intercalated graphene to be optically similar to exfoliated graphene and suitable candidate for potential applications.

Keywords: Dirac materials, topological crystalline insulators, graphene, spectroscopic ellipsometry, Landau level spectroscopy

Contents

I Introduction

Topology, a branch of mathematics exploring continuous transformation of spaces, usually deals with questions rather detached from everyday life, such as 'how can you define the holes in a torus or sphere' [1]? Yet it has experienced a dramatic growth in interest in the last two decades, best reflected by the 2016 nomination of the Nobel prize in physics [2, 3]. The award went for discoveries in the topological classification of matter. Different states of matter, besides the traditional gas, liquid, etc., can be additionally classified by topological invariants such as Chern numbers. They are topological in the sense that they are invariant under small deformations of the Hamiltonian [4].

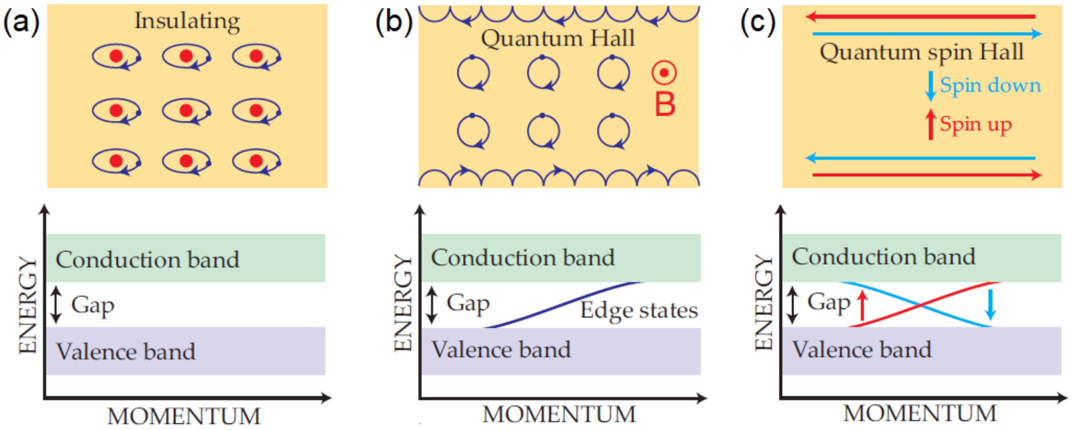

Figure 1.1: Topologically distinct classification of matter. A regular semiconductor with a gap at all values of the momentum and electrons (blue arrows) symbolically revolving around the red nucleus (a). Magnetic field induces edge states carrying current (b). Quantum spin Hall effect exhibits counterpropagating fully polarised currents with spin-up and spin-down electrons (c). It also features the signature linearly dispersing Dirac cones (blue and red lines) with massless fermions moving at relativistic speeds. [5].

Topological insulator (TI) is a distinct phase of matter first predicted just less than two decades ago [6]. In this class of materials strong spin-orbit coupling inverts the energy bands at the vicinity of the band-gap to create Dirac-like metallic conducting states at the edge or surface (in 2D or 3D case, respectively) of a bulk insulator. It is analogous to the quantum spin Hall effect, just that it is maintained by the spin-orbit coupling of the very material itself. The regular, quantum Hall and the related quantum spin Hall cases are sketched in fig. 1.1. These metallic states in TIs are topologically protected against small perturbations by the time-reversal symmetry and exhibit many interesting properties that are of great scientific and practical use. For example, owing to the strict distinction of the possible spin currents, backscattering in TIs would require a spin-flip which is energetically costly. Thus, owing to the forbidden backscattering and U-turns [7], the current flow in TIs would be disipationless, opening possibilities for next generation ultra-low energy consumption electronics. For scientists, on the other hand, TIs could serve as tabletop setups for relativistic experiments owing to charge carriers moving at $\approx c/300$, such as in graphene [8, 9]. Furthermore, TIs in contact with other materials can open doors to explore rather exotic states of matter such as electron-monopole composites called dyons or Majorana fermnions which are their own antiparticles [10]. TI states have been first proven to exist in HgTe [11] and later extended for other materials like BiSb [12].

However, the requirement of strong spin-orbit coupling limits the choice of suitable materials to those with high atomic numbers like Bi, Sb, Hg, Te. On the other hand, it was predicted in 2011 that TI phase is also possible in materials without any intrinsic spin-orbit coupling. Instead, the band inversion is achieved and topologically protected by the presence of mirror symmetry with respect to certain crystallographic plane of the crystal lattice instead of the time-reversal symmetry. This phase of matter is therefore titled Crystalline Topological Insulator (CTI) [13]. These states of matter were first predicted for SnTe material class and also related semiconductors PbTe and PbSe [14]. However, the topological states would be difficult to observe in pure SnTe due to low occupation of surface states. Since breaking the crystalline symmetry is easy by means of strain engineering, pressure or application of in-plane magnetic field, the band structure of CTIs could be in principle continuously tuned and have applications in thermoelectrics, infrared detection and tunable electronics [14].

Materials with conical conducting Dirac states and nontrivial topology are a relatively new and promptly emerging class, where new materials are proposed and subject of intensive scientific research. **This dissertation is aimed at exploring the general fundamental properties of several Dirac materials with topologically nontrivial states - lead tin salts and graphene**.
The particular goals are:

- investigate the optical properties of these materials using non-destructive spectroscopic ellipsometry and magneto-optical spectroscopy;
- develop and test a theoretical framework able to predict and explain the properties of the magneto-optical response;
- characterize the band structure of bulk and surface electrons.

II Dirac materials

The main feature connecting all materials investigated in this thesis is the so-called Dirac states. They are a natural outcome of the Dirac equation that aims to explore relativistic effects of moving electrons in the framework of quantum mechanics. Therefore, an introduction to this topic will be given in the next sections. Afterwards, the general properties of the investigated materials will be presented.

2.1 The Dirac equation

The standard Schrödinger equation does not deal with relativistic effects. In relativistic physics, the total energy of a particle is related to both the momentum p and the rest mass m_0:

$$E^2_{total} = (m_0c^2)^2 + (pc)^2, \tag{2.1}$$

where c is the speed of light. Purely algebraically, the energy then would be just the square root of the previous expression:

$$E_{total} = \sqrt{m_0^2c^4 + p^2c^2}, \tag{2.2}$$

which could be expanded into

$$E_{total} = m_0c^2\sqrt{1 + \frac{p^2}{m_0^2c^2}} \approx \underbrace{m_0c^2}_{\text{Rest mass energy}} + \underbrace{\frac{p^2}{2m_0}}_{\text{Kinetic energy}} - \underbrace{\frac{p^4}{8m_0^3c^2} + ...}_{\text{Relativistic corrections}} . \tag{2.3}$$

Paul Dirac took a different approach and was looking for a systematic method to examine relativistic effects up to the first order. He found an expression that made it especially easy to take the root. This turned out to be possible if it was a linear combination of the momentum and the rest mass:

$$m_0^2c^4 + p^2c^2 = (c\vec{\alpha} \cdot \vec{p} + \beta m_0c^2)^2. \tag{2.4}$$

To exclude the mixture between different terms, the newly introduced coefficient β and vector $\vec{\alpha}$ must satisfy

$$\alpha_x^2 = \alpha_y^2 = \alpha_z^2 = \beta^2 = 1, \tag{2.5}$$

and they must also mutually anticommute:

$$\alpha_i\alpha_j + \alpha_j\alpha_i = 0 \text{ for } i \neq j; \tag{2.6}$$

$$\alpha_i\beta + \beta\alpha_i \text{ for all } i. \tag{2.7}$$

It turns out that α and β satisfying the above conditions are matrices:

$$\vec{\alpha} = \begin{pmatrix} 0 & \vec{\sigma} \\ \vec{\sigma} & 0 \end{pmatrix} \tag{2.8}$$

and

$$\beta = \begin{pmatrix} I_{2x2} & 0 \\ 0 & -I_{2x2} \end{pmatrix}, \tag{2.9}$$

where $\vec{\sigma} = \{\sigma_x, \sigma_y, \sigma_z\}$ is a symbolic notation of a vector composed of the usual 2x2 Pauli spin matrices:

$$\sigma_x = \begin{pmatrix} 0 & 1 \\ 1 & 0 \end{pmatrix}, \sigma_y = \begin{pmatrix} 0 & -i \\ i & 0 \end{pmatrix}, \sigma_x = \begin{pmatrix} 1 & 0 \\ 0 & -1 \end{pmatrix}, \tag{2.10}$$

and I_{2x2} are 2x2 identity matrices. Thus, the resulting equation is four-dimensional at the end.

2.1.1 The Dirac Hamiltonian

Having established what the square of the energy is, it is trivial to get its root; having established the expression for the energy, it is straightforward to adapt it to the quantum Hamiltonian:

$$E_{Dirac} = c\vec{\alpha} \cdot \vec{p} + \beta m_0 c^2 \to \hat{H}_{Dirac}. \tag{2.11}$$

In explicit form, it reads

$$\hat{H}_{Dirac} = \begin{pmatrix} m_0 c^2 & 0 & p_z c & (p_x - ip_y)c \\ 0 & m_0 c^2 & (p_x + ip_y)c & -p_z c \\ p_z c & (p_x - ip_y)c & -m_0 c^2 & 0 \\ c(p_x + ip_y) & -p_z c & 0 & -m_0 c^2 \end{pmatrix} \tag{2.12}$$

with eigen energies

$$E_{eig}(p) = \pm\sqrt{(m_0 c^2)^2 + (pc)^2}, \tag{2.13}$$

just as expected. The dispersion relation is, in general, non-parabolic. There is a gap of $2m_0c^2$ separating the two branches (fig. 2.1).

The general solution is of the form

$$\Psi(\vec{r}, t) = \psi(\vec{r}) e^{-Et/\hbar}, \tag{2.14}$$

where $\Psi(\vec{r}, t)$ is, in general, a four-component wave function and $\psi(\vec{r})$ are free-particle (plane-wave) solutions:

$$\psi(\vec{r}) = u_p e^{i\vec{p}\cdot\vec{r}/\hbar}. \tag{2.15}$$

u_p is a four-component vector satisfying

$$\left[c\vec{\alpha} \cdot \vec{p} + \beta m_0 c^2\right] = E u_p. \tag{2.16}$$

The above equation can be written in a 2x2 matrix form:

$$\begin{pmatrix} m_0 c^2 & c\vec{\sigma} \cdot \vec{p} \\ c\vec{\sigma} \cdot \vec{p} & -m_0 c^2 \end{pmatrix} = E u_p, \tag{2.17}$$

which means that u_p can be expressed as a vector composed of 2 two-component vectors Φ and χ:

$$u_p = \begin{pmatrix} \Phi \\ \chi \end{pmatrix}. \tag{2.18}$$

Equation 2.17 can be interpreted and solved in two ways:

- $\vec{p} = 0$, $m_0 \neq 0$, describing a particle at its rest frame;
- $m_0 = 0$, $\vec{p} \neq 0$, describing a massless particle moving at relativistic speeds.

Interestingly, the Dirac equation allows negative energies to exist, predicting the existence of particle and antiparticle pairs such as electrons and positrons [15, 16].

2.1.2 General particle solutions of the Dirac Hamiltonian

For positive energies, the appropriate general solution is

$$\Phi = \begin{pmatrix} 1 \\ 0 \end{pmatrix}, \begin{pmatrix} 0 \\ 1 \end{pmatrix}, \tag{2.19}$$

describing a spin-1/2 particle propagating forward in time with an energy equal to the rest mass energy. The full four-component solution is

$$u_p = \begin{pmatrix} 1 \\ 0 \\ cp_z/(E + m_0c^2) \\ c(p_x + ip_y)/(E + m_0c^2) \end{pmatrix}, \begin{pmatrix} 0 \\ 1 \\ c(p_x - ip_y)/(E + m_0c^2) \\ -cp_z/(E + m_0c^2) \end{pmatrix}. \tag{2.20}$$

For negative energies, the solutions is

$$\chi = \begin{pmatrix} 1 \\ 0 \end{pmatrix}, \begin{pmatrix} 0 \\ 1 \end{pmatrix}, \tag{2.21}$$

or the full component version:

$$u_p = \begin{pmatrix} -cp_z/(|E| + m_0c^2) \\ -c(p_x + ip_y)/(|E| + m_0c^2) \\ 1 \\ 0 \end{pmatrix}, \begin{pmatrix} -c(p_x - ip_y)/(|E| + m_0c^2) \\ cp_z/(|E| + m_0c^2) \\ 0 \\ 1 \end{pmatrix}, \tag{2.22}$$

describing spin-1/2 particle moving backwards in time. Thus, the wave function components Φ and χ correspond to the *particle* and *anti-particle* components and are in general called **spinors**.

In the **non-relativistic limit**, when the speed of the particle is much lower than the speed of light, the dispersion closely resembles parabolic with the same gap of $2m_0c^2$ (fig. 2.1):

$$E_{non-rel}(p) \approx \pm \left(m_0c^2 + \frac{\vec{p}^2}{2m_0} \right). \tag{2.23}$$

Since $m_0c^2 > \vec{p}^2/2m_0$, the Ψ component dominates while χ becomes redundant. The eigenfunctions correspond to those of a free particle, just with a spin eigenfunction $\begin{pmatrix} 1 \\ 0 \end{pmatrix}$ for $m_s = \hbar/2$ or $\begin{pmatrix} 0 \\ 1 \end{pmatrix}$ for $m_s = -\hbar/2$. For positive energies, the upper component Ψ is called the *major component* and the lower component χ is called the *minor component* [15].

2.1.3 Ultra-relativistic massless Dirac fermions

When the particle mass is negligible, $m_0 = 0$, the **ultra-relativistic regime** applies, in which the energy dispersion simplifies to

$$E_{rel}(p) \approx \pm c|p|. \tag{2.24}$$

The particles move effectively at the speed of light. The signature shape of the ultra-relativistic dispersion is conic and gapless, with positive and negative

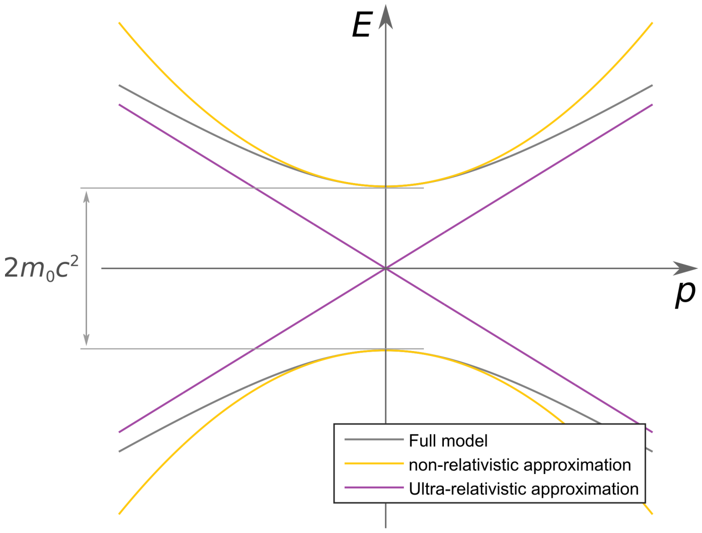

Figure 2.1: Relativistic energy dispersion: full model, non-relativistic and ultra-relativistic approximations. The full and non-relativistic models include a forbidden gap equal to $2m_0c^2$. The non-relativistic approximation gives the parabolic dispersion while the ultra-relativistic approximation gives rise to the gapless chiral Dirac cones intersecting at the origin.

energy dispersion lines touching at the origin (fig. 2.1). The fermions are said to be **massless Dirac fermions**.

The eigenvalue problem can be expressed by removing the rest mass m_0 from eq. 2.17 and taking into account the naming convention of the eigen functions introduced in eq. 2.18:

$$\begin{pmatrix} 0 & c\vec{\sigma}\cdot\vec{p} \\ c\vec{\sigma}\cdot\vec{p} & 0 \end{pmatrix} \begin{pmatrix} \Phi \\ \chi \end{pmatrix} = E \begin{pmatrix} \Phi \\ \chi \end{pmatrix}. \tag{2.25}$$

The solutions are then

$$E\Phi = c\vec{\sigma}\cdot\vec{p}\chi, \tag{2.26}$$

$$E\chi = c\vec{\sigma}\cdot\vec{p}\Phi. \tag{2.27}$$

They can be decoupled by taking these linear combinations of the newly defined two-component spinors:

$$N_R = \chi + \Phi, \tag{2.28}$$

$$N_L = \chi - \Phi, \tag{2.29}$$

leading to

$$EN_R = c\vec{\sigma}\cdot\vec{p}N_R, \tag{2.30}$$

$$EN_L = -c\vec{\sigma}\cdot\vec{p}N_L. \tag{2.31}$$

We know that in the ultra-relativistic regime, $E_{rel} \approx \pm c|p|$, therefore, we can further simplify to

$$\frac{\vec{\sigma}\cdot\vec{p}}{|\vec{p}|}N_L = -N_L, \tag{2.32}$$

$$\frac{\vec{\sigma}\cdot\vec{p}}{|\vec{p}|}N_R = N_R. \tag{2.33}$$

The term with $\vec{\sigma} \cdot \vec{p}$ can be explicitly written as

$$\vec{\sigma} \cdot \vec{p} = \begin{pmatrix} p_z & p_x - ip_y \\ p_x + ip_y & p_z \end{pmatrix}, \tag{2.34}$$

and its eigenvalues are $\pm|\vec{p}|$. The operator $\frac{1}{2}\frac{\vec{\sigma}\cdot\vec{p}}{|\vec{p}|}$ is known as the **helicity operator** and it is clear from the above equation that its eigenvalues are $\pm 1/2$: it is the spin operator projected in the direction of motion of the particle momentum. Therefore, N_R corresponds to solutions with negative helicity (right-handed particle) and N_L to positive helicity (left-handed particle) [16].

2.2 PbX materials and their properties

2.2.1 PbX (X=Sn, Se, Te) parent compounds

The lead chalcogenides or lead salts PbX (where X = Sn, Se or Te) are members of IV-VI semiconductors. They are the parent compounds of PbSnSe material investigated in this thesis. Hence, PbSnSe naturally inherits many of their properties. Therefore, it is worthwhile to properly introduce them, which is the main purpose of this chapter. This part of the thesis is closely related to the article on the same topic [17].

2.2.1.1 General features

Lead salts exhibit narrow band gaps in the order of 0.3 meV at room temperature. Compared with the usual III–V compounds, these IV–VI chalcogens present atypical electronic and transport properties: high carrier mobilities, high dielectric constants and positive temperature coefficients. These properties make the IV–VI compounds particularly useful electro-optical devices in the range of 3–30 um, corresponding to the medium and far infrared spectral region [18].

These materials have been known and intensively investigated for over 60 years. Their thermoelectric properties were extensively studied in both the USA and the Soviet Union for military and space applications in the 1950's and early 1960's. For instance, the Radioisotope Thermoelectric Generator based on PbTe thermoelectric generator was used in NASA's Apollo-12 mission. Fueled by the Pu-238 isotope, it provided 73 W of power for lunar surface experiments for nearly eight years [19].

Thus, owing to their narrow bandgap at room temperature, lead salts found use primarily in thermoelectric heat to power generation, IR detection, and as IR light sources in diodes and lasers.

As an example of another family of materials, HgCdTe has been the predominant material of choice for IR detection given its high performance to date. On the other hand, the cost of HgCdTe photodetector devices remains extremely high due to expensive molecular beam epitaxy growth involved in device fabrication. PbTe is a promising material candidate because of its superior chemical stability and the ease of film deposition [20]. PbTe is especially suitable for thermoelectric power generation at high temperatures [21] owing to its high thermoelectric efficiency (expressed as the figure of merit - FoM) surpassing 1.5 at 800 Kelvins [22]. Moreover, since both modern thermal engines and electronics alike still waste a considerable amount of power in a form of heat, thermoelectric heat-to-power generation is an attractive option for robust and environmentally friendly renewable energy production [23].

As another example, 2D materials such as boron nitride, transition metal dichalcogenides and black phosphorus are investigated for applications in high-performance electronic devices in field-effect transistors (FETs). Candidate 2D materials have to satisfy three requirements: a moderate electronic band gap, high carrier mobility and excellent electrode-channel contacts. The direct narrow gaps make PbX important in FETs, both from predicted and experimentally verified improvements in performance [24, 25]. Two-dimensional PbS nanosheets could be used in solar cells [26]. In the PbX family, the effects of quantum confinement are expected to be strong due to the low effective masses of the electrons and holes [27].

2.2.1.2 Structural properties

All three lead salts are polar semiconductors. The crystals are bonded via electrostatic forces between the anions. The ionicity is indicated both by well-defined reststrahlen reflectivity bands, as well as the effective charge present on the ions [28]:

$$e^* = (\epsilon_0 - \epsilon_\infty)(3/[\epsilon_\infty + 2])v_t(\pi M/N), \tag{2.35}$$

where ϵ_0 is the static and ϵ_∞ is the high-frequency dielectric constants, v_t is the transverse optical phonon frequency, M is the reduced mass of a PbX ion pair, N is the number of PbX units per unit volume. For a completely ionic compound, the effective charge on the ions would be $2e$, where e is the electron charge. Taking experimentally measured quantities, the e^* values for the PbX family are between 0.5-0.7. For comparison, although LiF is expected to be completely ionic, its $e^* = 0.82e$ [28]. Thus, lead salts exhibit a strong ionic contribution to the bonding.

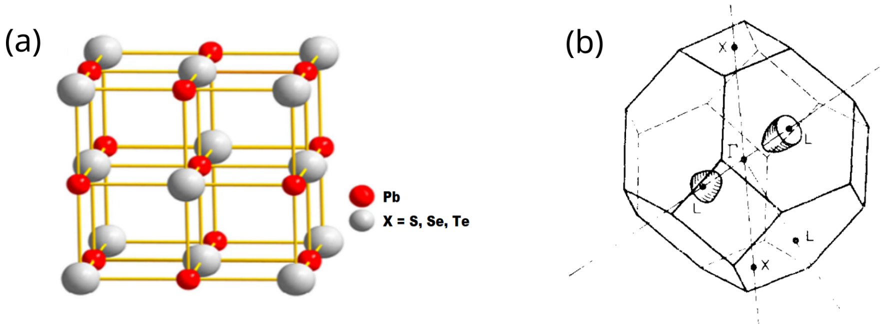

Figure 2.2: PbSe crystall structure (a, modified from [29]). The first Brillouin zone of PbX material family only showing one pair out of 4 equivalent valleys/Fermi pockets at the L point (b, from [28]). The exact band structure calculated for PbSe parent compound can be seen in fig. 4.39 on page 96.

The PbX family has the sodium chloride, or **rocksalt structure** at ambient temperature and pressure (fig. 2.2). The crystal lattice is of the face-centered cubic (FCC) type and the space group is *Fm3m*. The lattice basis consists of one atom of lead and X, respectively. The unit cube is formed out of eight lead and eight X atoms. In terms of the customary lattice constant a, the positions of the ions in the unit cell are:

$$\begin{array}{rl} \text{Pb}: & (000); \quad \left(\frac{a}{2}\frac{a}{2}0\right); \quad \left(\frac{a}{2}0\frac{a}{2}\right); \quad \left(0\frac{a}{2}\frac{a}{2}\right); \\ \text{X}: & \left(\frac{a}{2}\frac{a}{2}\frac{a}{2}\right); \quad \left(00\frac{a}{2}\right); \quad \left(0\frac{a}{2}0\right); \quad \left(\frac{a}{2}00\right). \end{array} \tag{2.36}$$

For an adequate description, the basis consisting of lead at (0,0,0) and X at (a/2,a/2,a/2) can be associated with the lattice point (0,0,0). The PbX lattice may also be considered as a simple cubic lattice in which lead ions and X ions occupy alternate lattice points. The number of PbX units in each unit cube of volume a^3 is four. Various sources and numerous theoretical calculations consistently report lattice constants of approximately 6 Å for PbX family [28, 30–32]. Explicit lattice constants for each distinct compound obtained from experimental and theoretical approaches are summarized in table 2.1.

Table 2.1: PbX lattice parameters at 299 K

Compound	Lattice constant (Å)
PbS	5.94
PbSe	6.12-6.13
PbTe	6.46-6.48

Taken from [28, 30–32].

2.2.1.3 Mechanical and thermal properties

Even though the thermal performance does not have a direct connection with this thesis, it is one of the main features of this material class. The most important thermal parameters are listed in table 2.2.

Thermoelectric performance is quantified by the figure of merit (FoM) $ZT = \sigma S^2 T/\kappa$. Here, σ is the electric conductivity, S is the Seebeck coefficient, T is the temperature and κ is thermal conductivity. Figure of merit is a strong function of doping and temperature. For the highest quality PbTe compounds, it reaches 1.4-1.5 [19]. PbSe was long thought to be much inferior to PbTe due to the smaller band gap and higher thermal conductivity expected from the lighter PbSe compared with PbTe. Nonetheless, with appropriate doping (for example, Na as it provides high hole concentration but does not interfere with PbSe valence bands), it can be an excellent thermoelectric material, comparable in performance to PbTe. Several other strategies to increase the FoM, such as alloying, nanostructuring and band modification, have been proposed. Being a more abundant material than Te, Se could be a cheaper alternative [32].

2.2.1.4 Electronic and optical properties

The general features of the band structures of the three compounds are similar. There are eight equivalent L points each at the center of a hexagonal Brillouin zone face, at its intersection with a [111] direction. The six equivalent X points are each at the center of a square zone face at its intersection with an [001] direction. The Gamma point is at the zone center [28]. There is a direct gap between the

Table 2.2: PbX lattice thermal and mechanical parameters at room temperature

Parameter	Unit	PbS	PbSe	PbTe
Density ρ	(g cm^{-3})	-	8.27	8.18
Seebeck coefficient S	(μV/K)	-	281	
Debye temperature Θ @ 25 K	(K)	159	144	128
Debye temperature Θ @ 300 K	(K)	-	191	163
Longitudinal speed of sound v_L	(m/s)	-	3220	2900
Transversal speed of sound v_T	(m/s)	-	1760	1600
Grüneisen parameter[1] γ	(arb.u.)	-	1.65	1.45
Longitudinal optical phonon energy $\hbar\omega_{LP}$	(eV)	0.0263	0.0165	0.0136
Transversal optical honon energy $\hbar\omega_{LP}$	(eV)	0.0083	0.0055	0.0040
Heat capacity C_p @ 25 K	(cal mole^{-1} deg^{-1})	2.81	8.44	4.24
Heat capacity C_p @ 240 K	(cal mole^{-1} deg^{-1})	11.6	11.9	12.0
Bulk modulus B	(MBar)	-	X	X
Pressure coefficient B'	(arb.u.)	-	3.6-4.6	3.9-4.3
Linear expansion coefficient a @ 30 K	(10^{-6}K^{-1})	7.54	7.56	9.02
Linear expansion coefficient a @ 300 K	(10^{-6}K^{-1})	20.27	19.40	19.80

Taken from [30, 32].
Comments: [1]Acoustic phonon Grüneisen parameter is a measure of anharmonic nature of lattice vibration.

L points. In each case, the valence band maximum and the conduction band minimum both occur at the L point. The bandgap is in the order of 0.3-0.4 eV at room temperature but falls down by half at cryogenic temperatures [28, 33](see table 2.3).

Table 2.3: PbX bandgaps at different temperatures

Temperature	PbS	PbSe	PbTe
4.2 K	0.286	0.165	0.190
77 K	0.280-0.307	0.150-0.176	0.200-0.217
300 K	0.410	0.270	0.310
373 K	0.440	0.310	0.340

Taken from [28, 34].

Properties connected with this gap can only be explained by taking into account the effective mass anisotropy and the strong nonparabolicity of the bands around the gap energy [35, 36]. The bands also deviate from Kane models at energies of relevance for their thermoelectric properties [37]. There is a large difference in the anisotropy of the effective masses for longitudinal (parallel to $\Gamma - L$) and transverse (perpendicular to the $\Gamma - L$) direction between the two salts [35, 36].

Table 2.4: PbX mass anisotropy at 4 K

Compound	Band	m_T/m_0	m_L/m_0	$K = m_L/m_T$	m_{eff}/m_0
PbS	conduction	0.080	0.015	1.3	0.087
	valence	0.075	0.015	1.4	0.083
PbSe	conduction	0.040	0.070	1.75	0.047
	valence	0.034	0.068	2.0	0.041
PbTe	conduction	0.024	0.240	10	0.034
	valence	0.022	0.310	14	0.032

Taken from [28].
Abbreviations:
m_0 is the free electron mass;
K is a mass anisotropy parameter.

The experimental results indicate that the surfaces of constant energy for both the conduction and valence bands are prolate ellipsoids of revolution (table 2.4). The centers of the ellipsoids are at L points and the major axes are in [1 1 1] directions. There are therefore eight equivalent constant energy ellipsoids for the conduction band states and eight for the valence band states. The ellipsoids can be represented by the following equation:

$$E(k) = \frac{\hbar^2}{2}\left(\frac{k_1^2}{m_T} + \frac{k_2^2}{m_T} + \frac{k_3^2}{m_L}\right). \tag{2.37}$$

k_l, k_2, and k_3 are the components of the wave vector k along three directions in k space. k_3 lies along a [1 1 1] direction. The equation of the constant energy surface is determined by the longitudinal and transverse effective masses m_L and m_T. The average conductivity effective mass m_{eff} used in transport equations is given by the equation $m_{eff} = (3m_L m_T)/(2m_L + m_T)$ for ellipsoidal constant energy surfaces.

The band gaps have negative pressure coefficients, i.e., they decrease with increase in pressure, in contrast to what is observed in III-V and II-VI semiconductors. Also, PbSe and PbTe provide a case in which the minimum energy gap of a compound semiconductor increases as the atomic number of the anion increases [30].

One well-known anomaly of PbX compound family is the unusual positive temperature coefficient $\mathrm{d}E_g/\mathrm{d}T$ of the direct gap E_g. It is approximately the same for all three compounds between a temperature range of 80 K and 373 K with a value of $(4.2 - 4.5) \times 10^{-4}$ eV/K. It is anomalous compared to other semiconductors usually having negative values. Another anomaly in the sequence of PbS, PbSe and PbTe is that the value of E_g for PbSe is smaller than for PbTe. This is contrary to the usual decrease of energy gap with increasing anion atomic number (e.g., GaP, GaAs, GaSb) [28].

The static and high-frequency dielectric constants, which are know from various experiments, are summarized in table 2.5.

Carrier concentrations and mobilities of these materials have been extracted from the Hall coefficient R_H measurements. They are notably independent of

Table 2.5: PbX dielectric constants

Compound	ϵ_0	ϵ_∞
	77 K	
PbS	184	17.6-19.2
PbSe	227	23.5-26.9
PbTe	428	35.3-38.5
	300 K	
PbS	172	16.9-17.4
PbSe	206	22.1-23.6
PbTe	380	32.2-33.4
	373 K	
PbS	162	15.8-16.5
PbSe	200	21.6-22.8
PbTe	371	31.3-32.6

Taken from [28, 34].

temperature over a wide range from 40 K to 300 K, implying that the extrinsic carrier concentration $n(p) = (1/eR_H)$ is independent of temperature as well. PbX are, in general, not intrinsic at room temperature [28]. Transport parameters are summarized in table 2.6.

Table 2.6: PbX transport properties

Compound	Carrier mobility μ (cm^2/V sec)		Typical carrier concentration n (10^{18} cm^{-3})
	77 K	300 K	
PbS	6 000-14 000	500-700	0.5-2
PbSe	11 000-16 000	1 000-1 200	0.7-3
PbTe	16 000-20 000	900-1 800	0.5-2

Taken from [28, 32, 34].

It is interesting to note that according to one theoretical study, few-layer PbX compounds might exhibit several-fold increase in these values. For instance, electron mobility could spike up to 252×10^3 cm^2/V.s for a two-layer case of PbS [24].

2.2.2 PnSnX (X=Se,Te) compunds

Substituting part of lead (Pb) by tin (Sn) produces a new material family, $\mathrm{Pb}_x\mathrm{Sn}_{1-x}\mathrm{X}$. Naturally, it maintains many of the properties of the parent compound class, PbX.

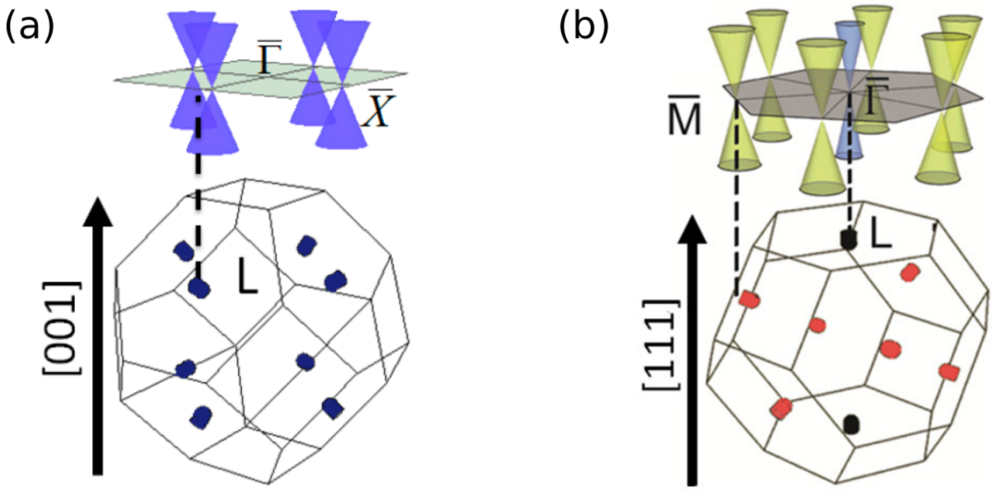

Figure 2.3: Possible orientations of $Pb_{1-x}Sn_xSe$ first Brillouin zone: [001] surface (a) and [111] surface (b) together with the constant energy ellipsoids (from [40, 41]).

2.2.2.1 Crystal structure

It was known early on that when the amount of introduced tin, x, is between 0 and 0.33-0.43, the new material **retains the rocksalt structure**. The lattice constant, on the other hand, changes linearly with the changing composition, as noticed by Krebs and other researchers in the late 60s [38, 39]. According to them, the change can be described by a linear law, with the lattice constant a_0 decreasing with increasing Sn content:

$$a_0(\text{Å}) = 6.12 - 0.12 \cdot x. \tag{2.38}$$

Apart from the difference in the lattice constant, the direct and k spaces otherwise hold the same parameters as the parent class PbX. Although changing the composition and consequently lattice structure inevitably does reflect in the change of the band structure, **the gap remains direct and located at the L point**.

Of particular importance is the first Brillouin zone, especially its orientation. The *fcc* crystal lattice contains 8 facets with L points. Thus, **PbSnX material family has 4 equivalent valleys**. This is crucial information for correctly interpreting optical experiments as well as theoretical results (e.g. interpreting carrier density, light absorption intensity and their multiplication factors).

The crystalline orientation can be controlled by preparing (either by growth, deposition or other methods) the material on an appropriately oriented substrate. There are two most prominent orientations for this material class, namely [001] and [111]. The [001] surface has the bandgap along the $\bar{\Gamma} - \bar{\text{X}}$ linecuts, while the [111] surface has it at one $\bar{\Gamma}$ point and three $\bar{\text{M}}$ points (fig. 2.3). The L point is longitudinal to the surface whereas the other points are oblique to it, see fig. 2.3 [40, 41]. They corresponding valleys are referred to as the longitudinal and oblique, respectively.

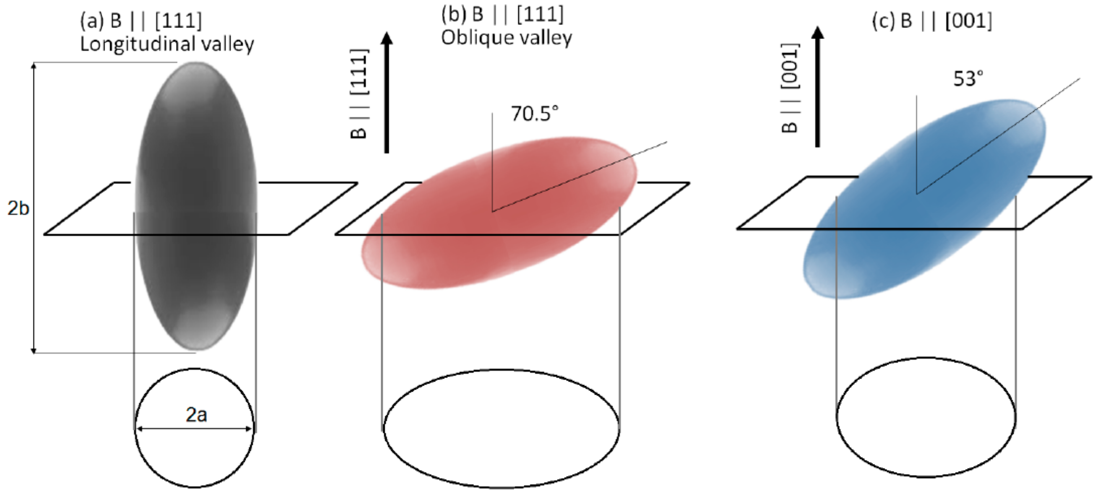

Figure 2.4: The orientation of the constant energy ellipsoids in PbSnX first Brillouin zone. The longitudinal valleys (a) are perpendicular while oblique valleys (b) are tilted 70.5 degrees to the [111] direction. At [001] surface, all valleys are tilted by 53 degrees (c). Circles below the ellipsoids mark the 2D cross-section surface around which the electrons would move in cyclotron motion under the applied magnetic field (from [41]).

2.2.2.2 Band closing and inversion

With the increasing interest in the PbSnX materials, another alluring feature was discovered. The unusual characteristic in PbSnX is the closing and re-opening of the band gap depending on the amount of tin and on temperature. In particular, for PbSnSe which is investigated in this thesis, the dependence of the bandgap can be described by the following formula [39]:

$$E_g(\mathrm{eV}) = 0.13 + (4.5 \times 10^{-4})T - 0.89 \cdot x. \tag{2.39}$$

Experimental data and their fit to this model are shown in figure 2.5. The closing of the gap can be achieved by **composition, temperature, as well as pressure**. Negative values signify the **band inversion** first proposed for $\mathrm{Pb}_x\mathrm{Sn}_{1-x}\mathrm{Te}$ as early as 1966 [42].

The valence band edge is an L_6^+ state and the conduction band edge is an L_6^- state. With increasing Sn composition, the energy gap initially decreases as these L_6 states approach each other. At some intermediate composition, the gap goes to zero (closes), and then reappears. Yet this time, valence band is the L_6^- state while the conduction band is L_6^+. The L_6 bands have only a two-fold spin degeneracy. Therefore, their crossover does not result in a semimetal but in a semiconductor with the valence and conduction bands interchanged [42]. According to early experiments, the critical concentration of Sn at which the band closes is between approximately $x = 0.2 - 0.3$, depending on temperature [39]. At the time of these experiments, there was no notion of topological states, the main feature of PbSnX material family. It was *partially* correctly assumed that band inversion arises because of relativistic effects in Pb and Sn (referring to the conical shape of the bands upon closing of the gap) [39, 42].

As for applications, the PbSnX compound family is used for similar purposes as the parent compound family PbX, namely, IR generation and detection. **The**

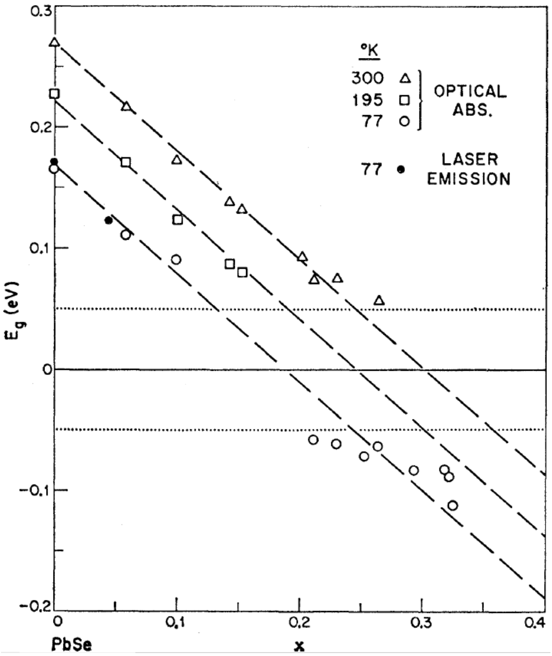

Figure 2.5: $Pb_{1-x}Sn_xSe$ band gap dependency on the amount of introduced tin and temperature; experimental data (scattered points) and fit to (2.39) formula (lines) (from [39]).

added benefit is undoubtedly the ability to adjust the band structure by simply changing the stoichiometric composition, temperature, pressure or strain. As an example, laser action has been demonstrated in PbSnTe [42]. For applications to optical switching with a CO_2 lasers, Fabry-Perot cavity switching was observed in PbSnSe [43]. Owing to their strong absorption of more than 2500 cm^{-1} and a relatively low Auger recombination probability, using the modern thin layer engineering technology has the potential to make high temperature lase operations possible in the mid-infrared and terahertz regions [44, 45]. At cryogenic temperatures, PbSnX in combination with quantum well structures could be used to detect various gasses [46] or generate THz radiation [47].

2.3 Monolayer graphene

The thesis part about graphene is based on [48]. As the current electronics industry is approaching its limits in terms of speed, size and bandwidth, graphene stands as a solid candidate for the basis of the next-generation devices. Its most alluring properties are high electron mobility surpassing 10 000 $\mathrm{cm^2V^{-1}s^{-1}}$ (or even tenfold higher in suspended graphene devices or graphene placed on h-BN) [49–51], carrier density tuning by an external electric field [49, 52], pico- and femtosecond timescales of carrier heating and cooling [53] etc. Graphene can be used as a transparent electrode enhancing the effectiveness of transparent conductors for future flexible devices [54, 55] or power conversion efficiency for solar cells [56].

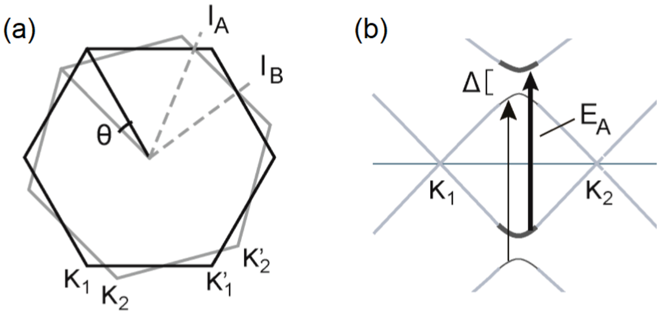

Figure 2.6: Brillouin zones of two graphene layers rotated by θ (a). Energy bands along the direction crossing K_1 and K_2 (b). A minigap Δ opens at I_A [57].

Graphene offers the possibility to fine-tune the van Hove singularities, something unattainable in other regular materials except changing E_F by doping or gating. The singularities are related to the joint density of states (jDOS) which is defined as

$$jDOS(\omega) = \frac{1}{4\pi^3}\int \delta[E_c(\vec{k}) - E_v(\vec{k}) - \hbar\omega]\mathrm{d}\vec{k}, \tag{2.40}$$

where E_c and E_v are the conduction and valence band energies [58]. It can be alternatively expressed not through the integral over k space but over energy in terms of a constant energy surface S_k:

$$jDOS(\omega) \propto \int \frac{\mathrm{d}S_k}{\nabla_{\vec{k}}(E_C - E_V)}. \tag{2.41}$$

The singularities arise where the jDOS diverge, i.e. where $E_C - E_V$ is constant. This drastically increases the light-matter interaction. In 2D materials such as graphene, this is determined by the curvature of the energy bands. The joint density of states is warped by twisting graphene multilayers with respect to each other as new states emerge at the crossing points of the sublattices of the two layers (fig. 2.6). Twisting is also observable as Moiré patterns in AFM pictures [57–59].

2.3.1 Graphene crystal structure

Structurally, graphene is composed entirely of carbon atoms arranged in a honeycomb lattice. It consists of two interpenetrating triangular sublattices. A unit cell consists of 2 carbon atoms A and B. Each atom has one s and three p orbitals [60, 61]. The lattice vectors can be defined as [8]

$$\vec{a}_1 = \frac{a}{2}\left(3, \sqrt{3}\right), \ \vec{a}_2 = \frac{a}{2}\left(3, -\sqrt{3}\right) \tag{2.42}$$

with interatomic distance $a \approx 1.42$Å. It follows that the Brillouin zone is also hexagonal (fig. 2.7), with the reciprocal lattice vectors

$$\vec{b}_1 = \frac{2\pi}{3a}\left(1, \sqrt{3}\right), \ \vec{b}_2 = \frac{2\pi}{3a}\left(1, -\sqrt{3}\right) \tag{2.43}$$

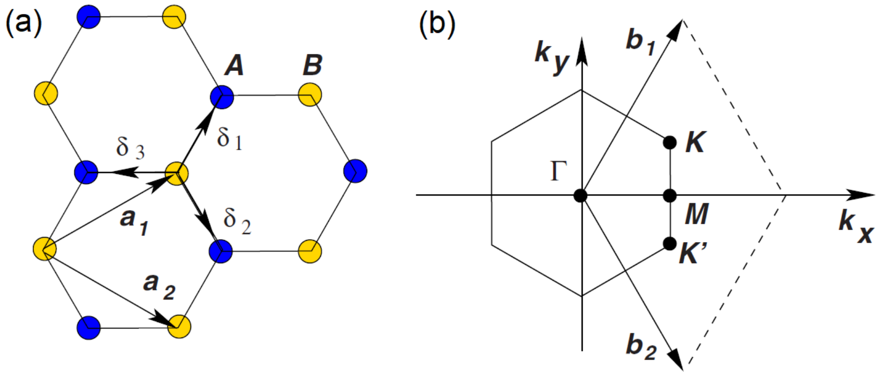

Figure 2.7: Graphene honeycomb lattice is consisting entirely of carbon atoms arranged out of two interpenetrating triangular lattices (a). A unit cell consists of one atom from each. The reciprocal lattice is also hexagonal (b) [8].

2.3.2 Graphene Hamiltonian

The first band model was developed for the graphite parent material [9]. It contains 4 valence electrons with wavefunctions of the form

$$\frac{1}{\sqrt{3}}(\psi_e(2s) + \sqrt{2}\psi_e(\sigma_i 2p)) \ (i = 1, 2, 3), \tag{2.44}$$

with $\psi_e(2s)$ the $(2s)$ wave function for carbon. $\psi_e(\sigma_i 2p)$ are the $(2p)$ wavefunctions with axes in the directions of σ_i joining the graphite atom to its 3 in-plane neighbors. The last electron is considered to be in $2p_z$ state. Only this electron outside the co-planar bonds contributes to conductivity. It hybridizes to form π valence and π^* conduction bands. A tight-binding approximation is used. According to it, the electrons can only jump between the nearest- and second-nearest neighbors, and the corresponding Hamiltonian is [8]

$$H = -t \sum_{\langle i,j\rangle,\sigma} (a^\dagger_{\sigma,i} b_{\sigma,j} + h.c.) - t' \sum_{\langle\langle i,j\rangle\rangle,\sigma} (a^\dagger_{\sigma,i} a_{\sigma,j} + b^\dagger_{\sigma,i} b_{\sigma,j} + h.c.). \tag{2.45}$$

In these units, $\hbar = 1$. $a_{\sigma,i}$ annihilates and $a^\dagger_{\sigma,i}$ creates electrons with spins $\sigma = \uparrow$ and $\sigma = \downarrow$, respectively, and the nearest-neighbor hopping energy is $t \approx 2.8$ eV. The above Hamiltonian suggests the following band dispersion [9]:

$$E_\pm = \pm t\sqrt{3 + f(\vec{k})} - t' f(\vec{k}), \tag{2.46}$$

where

$$f(\vec{k}) = 2\cos\left(\sqrt{3}k_y a\right) + 4\cos\left(\frac{\sqrt{3}}{2}k_y a\right)\cos\left(\frac{3}{2}k_x a\right), \tag{2.47}$$

with $a = 1.24$Å carbon interatomic distance and the next-nearest neighbor jumping distance $t' = -0.2t$. It is responsible for the electron-hole asymmetry. In the vicinity of K and K' points, Dirac-like cones appear (fig. 2.8), which can be seen upon expanding the full dispersion around those points by $\vec{k} = \vec{K} + \vec{q}$, with $\vec{q}$ measured relative to K and K' points, $\vec{q} \ll \vec{K}$ [8, 9]:

$$E_\pm \approx \pm v_F|\vec{q}| + O[(q/K)^2]. \tag{2.48}$$

The velocity parameter, also called the Fermi velocity,

$$v_F = \frac{3at}{2} \approx 10^6 \text{ m/s} = \frac{c}{300} \tag{2.49}$$

is independent on energy. Thus, **graphene essentially provides ground for tabletop relativistic physics experiments**.

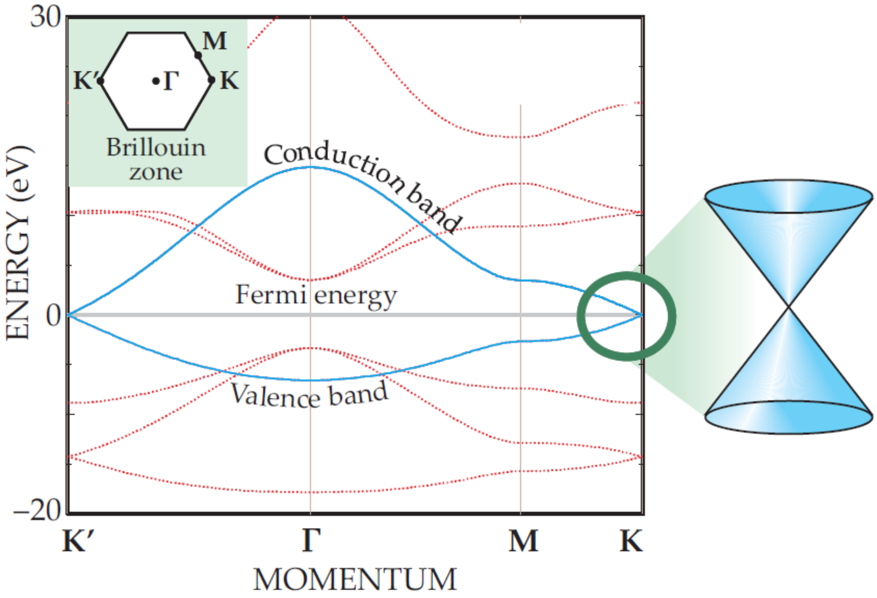

Figure 2.8: Graphene dispersion in the tight-binding approximation over the entire Brillouin zone. Note the gapless Dirac-like cones at K and K' points [61].

The dynamical conductivity is given by the Kubo-Greenwood formula [62, 63]:

$$\sigma(\omega, k) \sim \sigma_0 = \frac{e^2}{4\hbar}. \tag{2.50}$$

It is valid for $kv \ll k_b T \ll \hbar\omega$, where T is temperature and k_b is the Boltzmann constant. Remarkably, it is independent of any parameter of graphene, only defined by fundamental physical constants. It is worth noting that Suneya et al. came to an interesting generalized conclusion about the honeycomb lattices [60]. Starting from a general 2D honeycomb lattice with Dirac-like Hamiltonian, they derived the same linear dispersion condition around the K and K' points with $E = \pm\gamma|\vec{k}|$. In the self-consistent Born approximation, at $E_F = 0$, they got a slightly different result $\sigma(\omega = 0) = e^2/(\pi^2\hbar)$, even with broadening effects taken into account. **Thus the linear dispersion and optical conductivity independent of the material parameters seems to be the general property of honeycomb lattices**.

From the electromagnetic boundary conditions, the transmittivity of a single graphene sheet is [63]

$$T = \frac{1}{\left(1 + \frac{\pi\alpha}{2}\right)^2} \approx 1 - \pi\alpha \approx 97.7\%, \tag{2.51}$$

where

$$\alpha = \frac{e^2}{\hbar c} \approx \frac{1}{137} \tag{2.52}$$

is the fine structure constant independent of any graphene parameter. This was demonstrated experimentally. In other words, the absorption of a single graphene layer is 2.3%. For bilayer graphene, the absorption is $2\pi\alpha \approx 4.6\%$ in the visible range. The optical properties of graphene being defined by the fundamental constants is related to its 2D nature and zero energy gap, and does not directly involve the chiral properties of Dirac fermions [64].

III Experimental methods

3.1 Spectroscopic ellipsometry

In the broadest sense, ellipsometry is an experimental technique to measure the parameters of the ellipse of light polarisation, hence the name. Interaction with matter (for instance, reflection) changes the polarisation state of light. Applying a model reasonably describing the physical processes upon interaction, it is possible to determine the optical properties of that material if the parameters of the light beam are known. Ellipsometry is thus a non-contact, non-invasive and non-destructive method. This makes it especially popular in solid state physics, semiconductor industry and biophysics.

3.1.1 The main ellipsometric parameter ρ

One of the physical quantities describing light polarisation is the time-dependent vector of its electric field $\vec{E}$. The main quantity that the ellipsometry measures is the complex ratio ρ between the two orthogonal projections of this field reflected from the material, $\vec{E}_{\mathrm{R}}$. In terms of the Cartesian coordinate system, the electrical field can be separated into independent components parallel and perpendicular to the plane of incidence E_p and E_s. The parameter ρ then measures the ratio of their complex reflection coefficients $\tilde{R}_p$ and $\tilde{R}_s$:

$$\rho = \frac{\tilde{R}_p}{\tilde{R}_s} = \frac{E_p}{E_s}\frac{e^{i\phi_p}}{e^{i\phi_s}} = \tan(\Psi)e^{i\Delta}. \tag{3.1}$$

The angle between the projections of the amplitude is Ψ, while the phase difference is Δ. In order to understand this method better, we need to first recount how the ellipse of polarisation is characterized.

3.1.2 Ellipse of polarisation

The **ellipse of polarisation** describes the trajectory of the electric field vector which it traverses during one cycle at a fixed plane in space. Its two most important parameters are:

- the **azimuth** θ illustrating how much the major axis of the ellipse is tilted with respect to the x axis; it can take values between $-\pi/2$ and $\pi/2$. For linearly polarised light, this parameter would simply state the angle of polarisation;
- the **ellipticity or eccentricity** ϵ detailing how close the trajectory is to that of an ideal circle; can take values from $-\pi/4$ to $\pm\pi/4$. Zero value means *linear* polarisation. When the ellipse is traced in a clockwise direction (positive ellipticity), it defines the *right-handed circular polarisation*, and *left-handed circular polarisation* (negative ellipticity) in the counter-clockwise direction.

Any electric field vector can be decomposed into two orthogonal components. Two important bases are widely used:

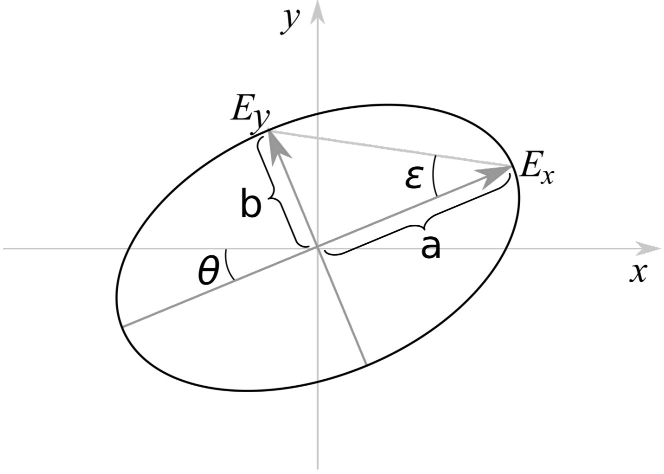

Figure 3.1: Ellipse of polarisation depicting the general trajectory of the electric field of polarised light. The main parameters are: major half-axis a, minor half-axis b, azimuth angle θ and ellipticity/eccentricity $\epsilon = \arctan(b/a)$. The intensity of this beam is proportional to $(a^2 + b^2)$.

- **The Cartesian basis**, or linear polarisation, offering a direct geometrical interpretation of the polarisation state. In this representation, the basis vectors are
$$E_x = \begin{pmatrix} 1 \\ 0 \end{pmatrix}, E_y = \begin{pmatrix} 0 \\ 1 \end{pmatrix} \tag{3.2}$$
;
- **The circular basis** with left- and right-handed polarisations LCP and RCP, the basis vectors being
$$E_{LCP} = \frac{1}{\sqrt{2}} \begin{pmatrix} 1 \\ -i \end{pmatrix}, E_{RCP} = \frac{1}{\sqrt{2}} \begin{pmatrix} 1 \\ i \end{pmatrix} \tag{3.3}$$
.

The transformation between the two basis takes this form:

$$T_{xy \to LR} = \frac{1}{\sqrt{2}} \begin{pmatrix} 1 & 1 \\ -i & i \end{pmatrix}. \tag{3.4}$$

In the case of circular polarisation, the azimuth is related to the phase difference of the circular basis fields:

$$\theta = \frac{\delta_L - \delta_R}{2}, \tag{3.5}$$

while the ellipticity is related to the difference of their amplitudes:

$$\tan \epsilon = \frac{E_L + E_R}{E_L - E_R}. \tag{3.6}$$

3.1.3 Jones formalism

Jones' mathematical framework is used to describe the polarisation state of a **perfectly polarised coherent** light and its transformation by linear optical elements. Since any absorption introduces depolarisation, Jones formalism is only suitable for transparent/reflective materials. Its strength is the simplicity (describing light and optical elements by simple 2D vectors and 2x2 matrices) and that it deals with the **electric field** directly. It quantifies the **phase information** and thus can describe interference.

The **Jones vector** $\boldsymbol{J}$ describes the polarisation state of light and is obtained by factoring out the axial and time dependencies of the monochromatic plane wave:

$$\vec{E}(\vec{r},t) = \begin{pmatrix} E_x(z,t) \\ E_y(z,t) \end{pmatrix} = \begin{pmatrix} E_{x0}e^{i(kz-\omega t+\phi_x)} \\ E_{y0}e^{i(kz-\omega t+\phi_y)} \end{pmatrix} = \underbrace{\begin{pmatrix} E_{x0}e^{i\phi_x} \\ E_{y0}e^{i\phi_y} \end{pmatrix}}_{\boldsymbol{J}} e^{i(kz-\omega t)}. \tag{3.7}$$

It is a complex number conveying information about the amplitude and phase of each orthogonal projection. The norm of $\boldsymbol{J}$ is thus equal to unity. Consequently, Jones vectors should be normalized to unit intensity so that they take the following form:

$$\boldsymbol{J} = \frac{1}{\sqrt{E_{x0}^2 + E_{y0}^2}} \begin{pmatrix} e^{i\phi_x} \\ e^{i\phi_y} \end{pmatrix}. \tag{3.8}$$

Jones vectors of the few most basic states of light are listed in table 3.1. Linear polarisations can be axially rotated by some angle θ using the rotation matrix $\boldsymbol{R}(\theta)$:

$$\boldsymbol{R(\theta)} = \begin{pmatrix} \cos\theta & -\sin\theta \\ \sin\theta & \cos\theta \end{pmatrix} \tag{3.9}$$

Table 3.1: Jones vectors in Cartesian coordinates

polarisation	Corresponding Jones vector
Linear x polarisation $\boldsymbol{J}_x$	$\begin{pmatrix} 1 \\ 0 \end{pmatrix}$
Linear y polarisation $\boldsymbol{J}_y$	$\begin{pmatrix} 0 \\ 1 \end{pmatrix}$
Linear polarisation rotated by θ degrees $\boldsymbol{J}_\theta$	$\boldsymbol{R}(\theta)\boldsymbol{J}_x = \begin{pmatrix} \cos\theta \\ \sin\theta \end{pmatrix}$
Circular right-handed polarisation $\boldsymbol{J}_{CRP}$	$\frac{1}{\sqrt{2}}\begin{pmatrix} 1 \\ +i \end{pmatrix}$
Circular left-handed polarisation $\boldsymbol{J}_{CLP}$	$\frac{1}{\sqrt{2}}\begin{pmatrix} 1 \\ -i \end{pmatrix}$
Elliptical polarisation (ellipticity ϵ) $\boldsymbol{J}_\epsilon^{ell}$	$\begin{pmatrix} \cos\epsilon \\ \sin(\epsilon)e^{\pm i\frac{\pi}{2}} \end{pmatrix}$
Elliptical polarisation (angle θ and ellipticity ϵ) $\boldsymbol{J}_{\theta,\epsilon}^{ell}$	$\boldsymbol{R}(\theta)\boldsymbol{J}_\epsilon^{ell} = \begin{pmatrix} \cos\theta\cos\epsilon \mp i\sin\theta\sin\epsilon \\ \sin\theta\cos\epsilon \pm i\cos\theta\sin\epsilon \end{pmatrix}$

Jones vectors are transformed by **Jones matrices** $\boldsymbol{M}$ representing various optical elements that are changing the polarisation of the light: mirrors, waveplates, poralisers etc. They are described by simple 2x2 matrices linearly altering $\boldsymbol{J}$'s components:

$$\boldsymbol{J} = \boldsymbol{M}\boldsymbol{J_0}. \tag{3.10}$$

Jones matrices for several usual optical elements are listed in table 3.2. In the reflection configuration, the matrix elements of $\boldsymbol{M_R}$ are the Fresnel amplitude reflection coefficients r_{ij}:

$$\boldsymbol{M_R} = \begin{pmatrix} r_{ss} & r_{sp} \\ r_{ps} & r_{pp} \end{pmatrix}. \tag{3.11}$$

Matrix elements r_{sp} and r_{ps} are the cross-polarisation coefficients.

Table 3.2: Jones matrices of popular optical elements

Optical element	Corresponding Jones matrix
x-polariser $\boldsymbol{P}_x$	$\begin{pmatrix} 1 & 0 \\ 0 & 0 \end{pmatrix}$
y-polariser $\boldsymbol{P}_y$	$\begin{pmatrix} 0 & 0 \\ 0 & 1 \end{pmatrix}$
Linear polariser $\boldsymbol{P}_\theta$ (polarizes at an angle θ)	$\boldsymbol{R}(-\theta)\boldsymbol{P}_x\boldsymbol{R}(\theta) = \begin{pmatrix} \cos^2\theta & \sin\theta\cos\theta \\ \sin\theta\cos\theta & \sin^2\theta \end{pmatrix}$
$\boldsymbol{P}_\theta \approx$ (small angle approximation)	$\begin{pmatrix} 1 & \theta \\ \theta & 0 \end{pmatrix}$
Phase retarder $\boldsymbol{C}_\delta$ (introduces phase delay $\delta_{x/y}$)	$\begin{pmatrix} e^{i\delta_x} & 1 \\ 1 & e^{i\delta_y} \end{pmatrix}$
Optically active material $\boldsymbol{A}_\theta$ (rotates polarisation by θ)	$\boldsymbol{R}(\theta)$
Generalized sample $\boldsymbol{S}$ (wiht its own Ψ and Δ)	$S = \begin{pmatrix} \sin\Psi e^{i\Delta} & 0 \\ 0 & \cos\Psi \end{pmatrix}$
Right circular polariser	$\frac{1}{2}\begin{pmatrix} 1 & i \\ -i & 1 \end{pmatrix}$
Left circular polariser	$\frac{1}{2}\begin{pmatrix} 1 & -i \\ i & 1 \end{pmatrix}$

Owing to their linearity, the overall effect of optical elements present in the system can be expressed as a single matrix, hiding the inner workings of a potentially complicated system:

$$\boldsymbol{J} = \underbrace{\boldsymbol{M}_1\boldsymbol{M}_2...\boldsymbol{M}_n}_{\boldsymbol{M}}\boldsymbol{J_0}. \tag{3.12}$$

For instance, the overall effect of crossing two polarisers is zero transmittivity, just as expected:

$$\boldsymbol{M}_{crossed} = \boldsymbol{P}_y\boldsymbol{P}_x = \begin{pmatrix} 0 & 0 \\ 0 & 1 \end{pmatrix}\begin{pmatrix} 1 & 0 \\ 0 & 0 \end{pmatrix} = \begin{pmatrix} 0 & 0 \\ 0 & 0 \end{pmatrix}; \tag{3.13}$$

Uncrossing them ever so slightly by a *small* angle θ results in the well-known **Malus' law**:

$$\boldsymbol{M}_{uncrossed}(\theta) = \boldsymbol{P}_y \boldsymbol{P}_x(\theta) \approx \begin{pmatrix} 0 & 0 \\ 0 & 1 \end{pmatrix} \begin{pmatrix} 1 & \theta \\ \theta & 0 \end{pmatrix} = \begin{pmatrix} 0 & 0 \\ \theta & 0 \end{pmatrix}, \tag{3.14}$$

and because

$$\begin{pmatrix} E_x \\ E_y \end{pmatrix} = \begin{pmatrix} 0 \\ \theta E_x \end{pmatrix}, \tag{3.15}$$

the measured intensity is $I \propto |E^2| \approx \theta^2 I_{in}$.

3.1.4 Stokes vectors

The Jones formalism is incapable of dealing with partially, randomly polarised or unpolarised light. To handle that, a more powerful mathematical apparatus is required.

A more general state of light is described by a four **Stokes parameters** $\{S\}$. The drawback is that Stokes vectors describe the **intensity** rather than the underlying electric field. They are, on the other hand, directly measurable. They do not keep the track of the phase and cannot describe interference. Stokes vectors are applicable to **incoherent** light.

Stokes parameters characterize the unpolarised, partially and completely polarised beams. To introduce Stokes vectors, assume an experimental setup with four independent light intensity detectors and four different filters in front of each:

- a netural density filter (affecting all polarisations) measuring I_0,
- horizontal polariser measuring I_{hor},
- linear polariser rotated by 45° degrees measuring I_{+45},
- right circular polariser measuring I_{RCP}.

The output of these measurements can be grouped into an abstract four-dimensional **Stokes vector**:

$$\begin{pmatrix} S_0 \\ S_1 \\ S_2 \\ S_3 \end{pmatrix} = \begin{pmatrix} I_0 \\ Q \\ U \\ V \end{pmatrix} = \begin{pmatrix} I_0 \\ 2I_{hor} - I_0 \\ 2I_{+45} - I_0 \\ 2I_{RCP} - I_0 \end{pmatrix} = \begin{pmatrix} I_{hor} + I_{ver} \\ I_{hor} - I_{ver} \\ I_{+45} - I_{-45} \\ I_{RCP} - I_{LCP} \end{pmatrix}. \tag{3.16}$$

The Stokes vector is always normalised so that $I_0 = 1$. The meaning of each coefficient is as follows:

- S_0, or I_0, measures total irradiance,
- S_1, or Q, measures the ratio of horizontally to vertically polarised light,
- S_2, or U, measures the ratio of light transmitted by +45° polariser to that transmitted by a +135° polariser,

- S_3, or V, measures the ratio of RCP to LCP light.

S can be directly related to the electric field components averaged over a suitable interval. Expressions in terms of the linear and circular polarisation basis are listed in table 3.3.

Table 3.3: Stokes coefficients in linear (x, y) and circular (L, R) basis

Linear	Circular
$I_0 = \|E_x\|^2 + \|E_y\|^2,$	$I_0 = \|E_L\|^2 + \|E_R\|^2,$
$I_1 = \|E_x\|^2 - \|E_y\|^2,$	$I_1 = 2\Re(E_L^* E_R),$
$I_2 = 2\Re(E_x E_y^*),$	$I_2 = -2\Im(E_L^* E_R),$
$I_3 = -2\Im(E_x E_y^*),$	$I_3 = \|E_R\|^2 - \|E_L\|^2,$

The Stokes vector expresses light polarisation in terms of known polarisations yet keeps the ability to describe partially or completely unpolarised light via the I_0 term. Therefore, the **degree of polarisation** p can be defined:

$$p = \frac{\sqrt{I_1^2 + I_2^2 + I_3^2}}{I_0}. \tag{3.17}$$

Its value would be 0 for a completely unpolarised, 1 for a perfectly polarised (be it linear, circular or elliptical) and intermediate values for partially polarised light. The relation between the Stokes parameters and the ellipse of polarisation are summarised in table 3.4. A few sample Stokes vectors are listed in table 3.5.

Table 3.4: Relation between the Stokes vector and the ellipse of polarisation [66]

Stokes parameters	polarisation ellipse
$S_1 = S_0 \cos 2\epsilon \cos 2\theta;$	$\theta = \frac{1}{2} \arctan\left(\frac{S_2}{S_1}\right);$
$S_2 = S_0 \cos 2\epsilon \sin 2\theta;$	$\epsilon = \frac{1}{2} \arcsin\left(\frac{S_3}{S_0}\right);$
$S_3 = S_0 \sin 2\epsilon;$	

Table 3.5: Sample Stokes vectors

Horizontally polarised	Vertically polarised	RCP	LCP	Unpolarised
$\begin{pmatrix}1\\1\\0\\0\end{pmatrix}$	$\begin{pmatrix}1\\-1\\0\\0\end{pmatrix}$	$\begin{pmatrix}1\\0\\0\\1\end{pmatrix}$	$\begin{pmatrix}1\\0\\0\\-1\end{pmatrix}$	$\begin{pmatrix}1\\0\\0\\0\end{pmatrix}$

3.1.5 Poincaré sphere

Disregarding the unpolarised portion of the intensity, I_0, the three remaining Stokes vector components can be parametrized and expressed in 3D coordinates of a unit (normalized) sphere representing all polarisation states:

- its poles represent the left/right circular polarisations;

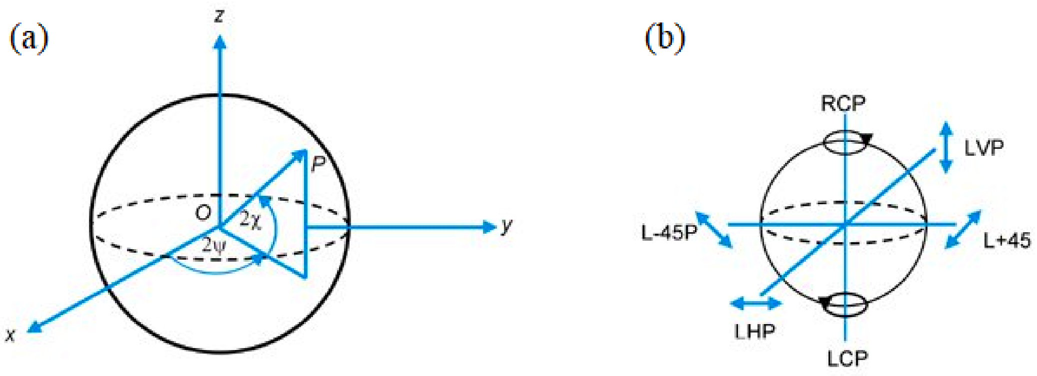

Figure 3.2: Poincaré sphere and its relation to the parameters of the polarisation ellipse (a). The meaning of the cardinal points and the poles (b). From [67].

- the cardinal points of the equator represent the linear horizontal/vertical and +45°/+135° polarisation pairs;
- intermediate equatorial points represent tilted linear polarisation;
- all other points represent *elliptical* polarisations.

Relation between this **Poincaré sphere** and the Stokes vector is described in table 3.6.

Table 3.6: Relation between the Poincaré sphere and Stokes vector

$I = S_0;$
$2\theta = \arctan \frac{S_2}{S_1};$
$2\epsilon = \arctan \frac{S_3}{\sqrt{S_1^2+S_2^2}};$

3.1.6 Muller matrices

Just like the Jones matrices describe how optical elements change Jones vectors, Mueller matrices represent the effect of optical elements on Stokes vectors. Being able to handle information about unpolarised light, they can represent various real-life objects such as absorbing materials. They are 4×4 matrices and a few basic of them are listed in table 3.7. Describing linear transformation, multiple optical elements can be combined into a single Muller matrix just like in eq. 3.12.

The Jones and Muller representations are related (on a condition that the sample does not depolarize the incident light beam, of course). The Muller matrix can then be obtained from the Jones matrix via this transformation [68]:

$$\boldsymbol{M}_{J\to M} = \boldsymbol{A}\left(\boldsymbol{J} \otimes \boldsymbol{J}^*\right)\boldsymbol{A}^{-1}, \tag{3.18}$$

where $\otimes$ denotes the tensor product and

$$\boldsymbol{A} = \begin{pmatrix} 1 & 0 & 0 & 1 \\ 1 & 0 & 0 & -1 \\ 0 & 1 & 1 & 0 \\ 0 & -i & i & 0 \end{pmatrix}. \tag{3.19}$$

Table 3.7: Sample Muller matrices

Horizontal polariser	Vertical polariser	RCP	LCP
$\frac{1}{2}\begin{pmatrix}1 & 1 & 0 & 0\\ 1 & 1 & 0 & 0\\ 0 & 0 & 0 & 0\\ 0 & 0 & 0 & 0\end{pmatrix}$	$\frac{1}{2}\begin{pmatrix}1 & -1 & 0 & 0\\ -1 & 1 & 0 & 0\\ 0 & 0 & 0 & 0\\ 0 & 0 & 0 & 0\end{pmatrix}$	$\frac{1}{2}\begin{pmatrix}1 & 0 & 0 & 1\\ 0 & 0 & 0 & 0\\ 0 & 0 & 0 & 0\\ 1 & 0 & 0 & 1\end{pmatrix}$	$\frac{1}{2}\begin{pmatrix}1 & 0 & 0 & -1\\ 0 & 0 & 0 & 0\\ 0 & 0 & 0 & 0\\ -1 & 0 & 0 & 1\end{pmatrix}$
Quarter wave plate (fast axis vertical)	Quarter wave plate (fast axis horizontal)	Half wave plate/ ideal mirror	
$\begin{pmatrix}1 & 0 & 0 & 0\\ 0 & 1 & 0 & 0\\ 0 & 0 & 0 & -1\\ 0 & 0 & 1 & 0\end{pmatrix}$	$\begin{pmatrix}1 & 0 & 0 & 0\\ 0 & 1 & 0 & 0\\ 0 & 0 & 0 & 1\\ 0 & 0 & -1 & 0\end{pmatrix}$	$\begin{pmatrix}1 & 0 & 0 & 0\\ 0 & 1 & 0 & 0\\ 0 & 0 & -1 & 0\\ 0 & 0 & 0 & -1\end{pmatrix}$	

For isotropic samples, in which $r_{sp} = r_{ps} = 0$, the normalized Jones-Muller matrix simplifies to

$$\boldsymbol{M}_{J\rightarrow M} = \begin{pmatrix}1 & -N & 0 & 0\\ -N & 1 & 0 & 0\\ 0 & 0 & C & S\\ 0 & 0 & -S & C\end{pmatrix}, \tag{3.20}$$

where the parameters N, S, C are given by:

$$N = \cos{(2\Psi)}, \tag{3.21}$$

$$S = \sin{(2\Psi)}\sin\Delta, \tag{3.22}$$

$$C = \sin{(2\Psi)}\cos\Delta, \tag{3.23}$$

and the main ellipsometric parameter

$$\rho = \frac{C + iS}{1 + N}. \tag{3.24}$$

Its components can then be easily determined [69]:

$$\Psi = \frac{1}{2}\arctan\left(\frac{\sqrt{C^2 + S^2}}{N}\right), \tag{3.25}$$

and

$$\Delta = \arctan\left(\frac{S}{C}\right). \tag{3.26}$$

Since $N^2 + S^2 + C^2 = 1$, this means that for isotropic sample, only two parameters are needed to fully specify $\boldsymbol{M}$.

For birefringent samples, $r_{sp} \neq r_{ps} \neq 0$. The off-diagonal elements of $\boldsymbol{M}$ no longer equal zero. As long as the sample is not depolarizing, equation 3.20 still applies. Yet, six elements are required to specify $\boldsymbol{M}$ as ρ is actually split into ρ_{ps} and ρ_{sp}, with the appropriate coefficients C_{sp}, C_{ps}, S_{sp} and S_{ps}, respectively [68].

3.1.7 Experimentally measured ellipsometric quantities

The main ellipsometric parameter ρ is never measured directly. Instead, it is usually a function of particular parameters directly available in the experiment, and must be recalculated from them.

Since ellipsometry deals with polarised light, it requires polarizing optical elements like polariser, analyzer, phase modulator and others. In typical optical experiments, these elements can be rotated at arbitrary angles according to the goal of the measurement. Let the angle of polariser, analyser, compensator and others be $P, A, C, ...$, respectively. Therefore, ρ is the function of the angles of those elements:

$$\rho = f(P, A, C, ...). \tag{3.27}$$

Which optical elements are used exactly depends on the design of a particular ellipsometer. There are many types of ellipsometers, each with its own advantages and drawbacks (fig. 3.3):

- the **nulling ellipsometer**, the first historical approach in ellipsometry, uses crossed polariser and analyzer with a compensator between them. The compensator is rotated so that it distinguishes the signal. Although being accurate with low systematic errors, it is slow to operate as it works on single wavelengths;

- **phase modulation ellipsometers** can operate at high modulation rates, in the order of tens of kHz, and can be used for a rapid acquisition of data. They, however, also operate at single wavelengths and require intensive light sources in order to achieve a satisfactory signal-to-noise ratio;

- **Rotating polariser/analyzer/compensator ellipsometers** use the same mathematical approach of Fourier transform as in FTIR spectrometers. They periodically modulate the polarisation state by continuously rotating certain optical elements. This encodes the polarisation-related signal in time domain which can be decomposed into frequency-dependent components during analysis. This allows obtaining data for a broad range of light spectrum in a single measurement cycle. These are the prevalent designs of modern ellipsometers and will be described in more detail.

Rotating polariser (RPE) and **rotating analyzer ellipsometers (RAE)** only have polariser and analyzer, one of which is made to rotate at a constant angular velocity, modulating the light (fig. 3.3). The two configurations are mathematically equivalent. The Jones matrices are arranged as follows:

$$\boldsymbol{E}_{out} = \boldsymbol{A}\boldsymbol{R}(A)\boldsymbol{S}\boldsymbol{R}(-P)\boldsymbol{P}\boldsymbol{E}_{in}, \tag{3.28}$$

with $\boldsymbol{E}$ representing the electric field Jones vectors at the ellipsometer input and output, and $\boldsymbol{P}$ and $\boldsymbol{A}$ represent the polariser and analyzer, each turned at arbitrary angles P and A. The sample is represented by $\boldsymbol{S}$. The general formula for detected intensity with arbitrary angles of all polarizing optical elements is

$$I_{RPE/RAE} \propto \boldsymbol{E}^*_{out}\boldsymbol{E}_{out} \propto 1 - N\cos(2P) + (\cos(2P) - N)\cos(2A) + C\sin(2P)\sin(2A). \tag{3.29}$$

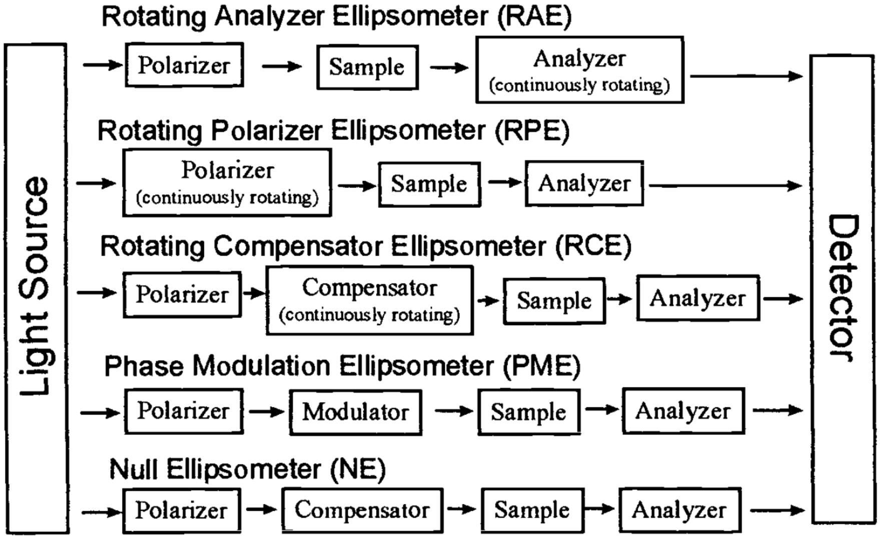

Figure 3.3: Block diagram of various ellipsometer configurations [70].

The parameters N and C are defined as in eqs. 3.21 and 3.23. In the case of analyzer rotating at a constant speed, $A = \omega t$ and $P = const$. It is vice versa in the case of rotating polariser (then it is $A = const$ and $P = \omega t$). The signal can be decomposed into harmonic sine and cosine components. Their amplitudes are a and b:

$$I = I_0(1 + a\cos 2\omega t + b\sin 2\omega t). \tag{3.30}$$

The double frequency appearing in the parenthesis represents the fact that when one polarizing elements (analyzer) rotates with respect to another (polariser), the crossing happens twice per full cycle. The normalized values of the frequency coefficients are [68, 71, 72]:

$$\alpha = \frac{a}{DC} = \frac{\cos(2P) - N}{1 - N\cos(2P)}, \beta = \frac{b}{DC} = \frac{C\sin(2P)}{1 - N\cos(2P)}. \tag{3.31}$$

For a specific case of $P = 45°$, the coefficients simplify to

$$\alpha = -N, \beta = C. \tag{3.32}$$

Thus, the N and C parameters can be directly extracted. In a more general case, the trigonometric double-angle formulas can be used to invert eqs. 3.31 and recover the ellipsometric angles:

$$\tan\Psi = \sqrt{\frac{1+\alpha}{1-\alpha}}|\tan P|, \cos\Delta = \frac{\beta}{\sqrt{1-\alpha^2}}. \tag{3.33}$$

Data processing is therefore done in a strict sequence in RAE/RPE ellipsometry: first, α and β are extracted by Fourier-transforming the raw experimental data. Then, formulas 3.33 are applied to extract the final ellipsometric quantities Ψ and Δ. However, RAE design suffers from large errors in Δ when it is near 0° or 180°. The S parameter is not measured, which is equivalent to saying that Δ is limited to $[0° : 180°]$ rather than the full range.

The limitations of RPE and RAE are overcome by introducing a **rotating compensator** between the polariser and the sample instead. The compensator can be a waveplate, for instance. The Jones formalism representation becomes [71]:

$$\boldsymbol{E}_{out} = \boldsymbol{A}\boldsymbol{R}(A)\boldsymbol{R}(-C)\boldsymbol{C}\boldsymbol{R}(C)\boldsymbol{S}\boldsymbol{R}(-P)\boldsymbol{P}\boldsymbol{E}_{in}, \tag{3.34}$$

with $\boldsymbol{C}$ representing the compensator and $\boldsymbol{R}(\pm C)$ an arbitrary rotation at an angle C that it introduces. The compensator introduces a phase delay δ:

$$\boldsymbol{C} = \begin{pmatrix} e^{-i\delta} & 0 \\ 0 & 1 \end{pmatrix}. \tag{3.35}$$

With the compensator rotating at a constant angular speed $C = \omega t$, the light is continuously changing its states between linear and left- and right-circular polarisations, with intermediate elliptical polarisations in between. Placing a rotating compensator next to stationary polariser and analyzer introduces 2ω and 4ω harmonic components into a signal, α_2, α_4, β_2 and β_4:

$$I = I_0(1 + \alpha_2 \cos 2\omega t + \beta_2 \sin 2\omega t + \alpha_4 \cos 4\omega t + \beta_4 \sin 4\omega t). \tag{3.36}$$

Data analysis flow is analogous to RPE/RAE: Fourier analysis first extracts the amplitudes and those are then inverted to yield the resulting ellipsometric angles. The general expressions in RCE case are complicated. For illustrative purposes, only a special case will be considered here, in which the angles are chosen so that $P = 0°$ and $A = 45°$. The Fourier coefficients of the detected light intensity then are [72]:

$$\alpha_2 = 0, \beta_2 \propto S \sin\delta, \alpha_4 \propto N(1 - \cos\delta), \beta_4 \propto C(1 - \cos\delta). \tag{3.37}$$

For an ideal retarder, the phase retardance $\delta = 90°$, and the above equations above simplify further to simple statements of equality between the measured and calculated coefficients. Therefore, the RCE is able to directly measure N, C and S, as well as the full range of Ψ and Δ.

More advanced ellipsometer designs employ several rotating elements, such as **dual rotating compensators** placed before and after the sample, allowing to capture all the 16 components of the full Muller matrix. Their design and analysis complexity increases with the added elements and is beyond the scope of this introductory chapter. Moreover, some designs are proprietary and patent-protected.

3.1.8 Ellipsometric data analysis

The goal of an ellipsometric experiment is to determine the structural and optical properties of the sample being examined. So far we have learned how the Jones or Muller matrix coefficients, and subsequently, the main ellipsometric parameter ρ can be recovered.

In the case of a single semi-infinite, isotropic and homogeneous material serving as a substrate, and a ideal single interface between it and the semi-infinite surrounding ambient, the Fresnel coefficients for the p and s polarizartions are [73]:

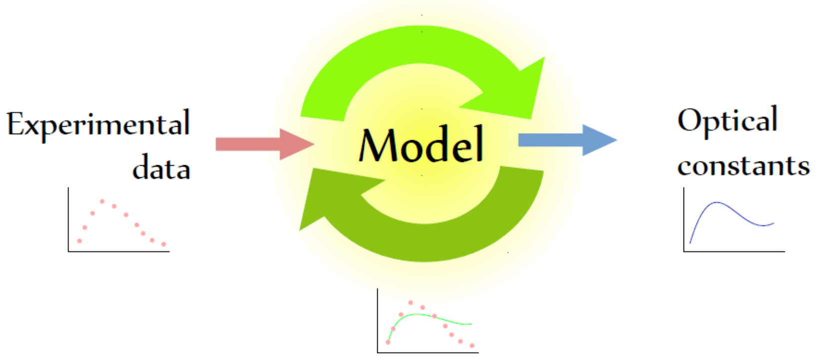

Figure 3.4: The iterative process of ellipsometry data processing.

$$r_p = \frac{\tilde{n}_s \cos\theta_i - \tilde{n}_a \cos\theta_t}{\tilde{n}_s \cos\theta_i + \tilde{n}_a \cos\theta_t}, \tag{3.38}$$

$$r_s = \frac{\tilde{n}_a \cos\theta_i - \tilde{n}_s \cos\theta_t}{\tilde{n}_a \cos\theta_i + \tilde{n}_s \cos\theta_t}, \tag{3.39}$$

with $\tilde{n}_s$ and $\tilde{n}_a$ representing the complex refractive indices $\tilde{n} = (n - ik)$ of the sample and ambient, respectively, and θ_i and θ_t representing the incident and transmitted angles. The latter are related by the well-known Snell's law.

If the angles are known, the measured ellipsometric parameters can be inverted and recalculated into the complex optical parameters of the reflecting substrate medium ϵ_s:

$$\epsilon_s = \tilde{n}_s^2 = \epsilon_a \sin^2\theta_i \left[1 + \tan^2\theta_i \left(\frac{1-\rho}{1+\rho}\right)^2\right]. \tag{3.40}$$

For real samples with layered structure, a more complex description is used. It is based on Yeh's, or transfer matrix formalism. Each layer's transfer matrix is obtained by solving the wave equation in the medium. The exact description depends on whether the layer is isotropic or birefringent, its thickness and other features. In a multi-layer case, recovery of the optical constants is not as straightforward and the simple formula 3.40 cannot be applied directly. The spectrally-dependent optical constants are then described by parametrized mathematical functions and **fit** so that the final output, the simulated ρ, would match the measured one over the entire available spectral range. It is an iterative process (fig. 3.4). In order to increase its robustness, several strategies can be employed:

- the acquisition time can be increased in order to maximize the signal-to-noise ratio. This requirement is rather easily fulfilled as modern RCE exhibit angular frequencies in the order of tens of Hz, obtaining hundreds and thousands of independent measurements in the course of minutes;

- the same sample can be measured at several angles of incidence, providing more data points for fitting as the angle of incidence can be set precisely. This is called the Variable Angle Spectroscopic Ellipsometry, or VASE.

3.2 Magneto-optical spectroscopy

The ellipsometric techniques described earlier deal with samples without any external electromagnetic fields besides the probing beam. Introducing an additional external field modifies the light and sample interaction based on its properties. In the broadest sense, this upgraded technique is called **the magneto-optical spectroscopy**. A particular subset of this technique was used in this research and will be described in the following chapters.

3.2.1 Classical cyclotron resonance

Magnetic field influences the movement of electrons. In the classical theory of electromagnetism, electrons do experience the Lorentz force just like any other charged particles, which makes them move in circular orbits in a plane perpendicular to the field direction (if the field and velocity vectors are perpendicular, see fig. 3.5). This periodic rotating movement of charged particles in a uniform magnetic field is called the **cyclotron resonance**. The parameters of this motion are easily calculated by equating the magnitudes of the centrifugal and Lorentz forces:

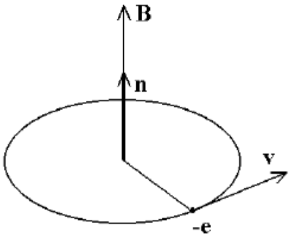

Figure 3.5: The classical Larmor rotation of an electron in a homogeneous external magnetic field [74].

$$evB = \frac{mv^2}{r}, \tag{3.41}$$

from which the radius of the orbit (also called the **cyclotron radius** or **Larmor radius**), r, and its cyclotron frequency ω_c can be extracted:

$$r = \frac{mv}{eB}, \tag{3.42}$$

$$\omega_c = \frac{eB}{m}. \tag{3.43}$$

3.2.2 Classical Hall effect

If an external magnetic field is applied perpendicular to a steadily flowing current, charge carriers experience the Lorentz force. It causes a buildup of charges at the sides of the sample slab, which in turn induces the electric field. This is the essence of the classical **Hall effect**. Its quantitative properties can be seen by analyzing the equations of motion:

$$m_{eff}\frac{\mathrm{d}v}{\mathrm{d}t} = -e(\vec{E} + [\vec{v} \times \vec{B}]) - \frac{m_{eff}}{\tau}\vec{v}, \tag{3.44}$$

the last term being the phenomenological scattering term. These equations eventually lead to the magneto-conductivity tensor, which in case of a thin two-dimensional sample is:

$$\hat{\sigma} = \frac{\sigma_0}{1 + (\omega_c \tau)^2} \begin{pmatrix} 1 & +\omega_c \tau \\ -\omega_c \tau & 1 \end{pmatrix}, \tag{3.45}$$

where $\sigma_0 = ne^2\tau/m_{eff}$ is the Drude conductivity. It can be alternatively expressed in terms of resistivity:

$$\hat{\rho} = \hat{\sigma}^{-1} = \frac{1}{\sigma_0} \begin{pmatrix} 1 & -\omega_c \tau \\ +\omega_c \tau & 1 \end{pmatrix}. \tag{3.46}$$

The off-diagonal term ρ_{xy} is related to the **Hall resistivity** R_H:

$$\rho_{xy} = \frac{-\omega_c \tau}{\sigma_0} = B \underbrace{\frac{-1}{ne}}_{R_H} = BR_H. \tag{3.47}$$

The Hall effect thus allows to experimentally determine the concentration and the sign of the charge carriers. Nowadays, it is used in applications such as magnetic field sensors etc.

3.2.3 Landau quantization

The picture becomes more complex in the framework of the quantum mechanics. The electron orbits become quantized, which in turn gives rise to the quantization of other properties. An additional set of quantized electron energy levels appear, giving rise to a rich variety of transitions between them in the IR part of the spectrum. This in turn offers yet another tool to explore the electronic properties of materials.

The effect of a static external magnetic field on the quantum system consisting of a single charged particle is introduced via the **Peierls substitution** of the canonical momentum operator:

$$\vec{p} \to (\vec{p} - e\vec{A}), \tag{3.48}$$

with the actual magnetic field $\vec{B}$ and the magnetic vector potential $\vec{A}$ related by $\vec{B} = \nabla \times \vec{A}$.

Many options exist for the choice of the gauge. Although the sample is both rotationally and translationally invariant, there isn't a gauge satisfying both conditions:

- the gauge of the form $\vec{A} = B(-y, 0, 0)$ preserves the translational invariance along the x axis, and $\vec{A} = B(0, x, 0)$ preserves it along the y axis. It is the simplest and allows adding a potential $V(\vec{r})$ with little modification.

- the rotationally symmetrical gauge is $\vec{A} = B/2(-y, x, 0)$ is used in writing the wavefunctions in fractional quantum Hall effect. Its ground state is localised, giving an example of a coherent wavepacket.

The chosen gauge is then put into the appropriate equations of motion. From here on, both the semiclassical and fully quantum models can be used. Both give the same quantitative results in terms of the energy spectra and the radiuses of the ground state:

- in the semiclassical approach, the Bohr-Sommerfeld quantization rule is used, stating that the motion of a particle is constrained to discrete values:

$$\oint (m\vec{v} - e\vec{A})\,\mathrm{d}\vec{r} = (n + \gamma)h, \tag{3.49}$$

  where the quantum correction because of the so-called Berry's phase $\gamma = 1/2$;

- in the fully quantum model, proper quantum operators are introduced into the standard Schrödinger equation which is then solved either directly or by use of the usual creation and annihilation operators.

We will briefly overview the results of the fully quantum theory here using the Landau gauge $\vec{A} = (-By, 0, 0)$ for simplicity. The momentum operator can be split into its Cartesian components:

$$(\vec{p} - e\vec{A})^2 = (p_x + eBy)^2 + p_y^2 + p_z^2. \tag{3.50}$$

Substituting it into the Hamiltonian without the potential, it can be separated into two parts, one describing the electron motion in the z direction and another in the xy plane:

- in z direction, electron behaves as a free particle and its movement is unaffected:

$$E_z(k_z) = \frac{\hbar^2 k_z^2}{2m_{\mathrm{eff}}} \tag{3.51}$$

  and the wavefunction is

$$\Psi(z) = \exp(\pm i k_z z). \tag{3.52}$$

- the xy plane is where the change happens. The wavefunction can be expressed as

$$\Psi(x, y) = f(x)\exp(\pm i k_y y), \tag{3.53}$$

  where $f(x)$ is the wavefunction of a harmonic oscillator (a Gaussian) shifted from its equilibrium position by

$$x_0 = \frac{\hbar k_y}{m_{\mathrm{eff}}\omega_c}. \tag{3.54}$$

  The frequency of this oscillator is ω_c (the same as given by the classical limit) and the eigenvalues are those of the usual quantum harmonic oscillator, an infinite ladder of equidistantly-spaced **Landau levels** (fig. 3.7 (a)):

$$E_{x,y}(B, N) = \hbar\omega_c\left(N + \frac{1}{2}\right), \tag{3.55}$$

  with the level index $N = 0, 1, 2, ...$ The splitting of electron energy in the presence of external magnetic field is called **Landau quantization**.

Therefore, the total energy spectrum of electrons in a constant external magnetic field in a three-dimensional space is

$$E(B, N, k_z) = E_{x,y}(B, N) + E_z(k_z) = \hbar\omega_c \left(N + \frac{1}{2}\right) + \frac{\hbar^2 k_z^2}{2m_{\text{eff}}}, \tag{3.56}$$

being unconstrained in one coordinate and constrained in the others, the total energy spectra forms a set of energy bands (fig. 3.7 (b)). They can be further refined by including the Zeeman splitting, giving an additional energy contribution

$$\Delta E(B) = \pm\frac{1}{2} g_{\text{eff}} \mu_B B \tag{3.57}$$

for spin-up and spind-down electroncs, respectively. Here, μ_B is the Bohr magneton and g_{eff} is the effective Landé g-factor.

The radius of an electron orbit of the N-th level is

$$r(N) = \sqrt{N+1}\underbrace{\sqrt{\frac{\hbar}{eB}}}_{l_b}, \tag{3.58}$$

where the quantity l_b is called the **magnetic length**. It is the radius of the Landau ground state, and more importantly, the lowest radius of a circular orbit in a magnetic field allowed by the uncertainty principle.

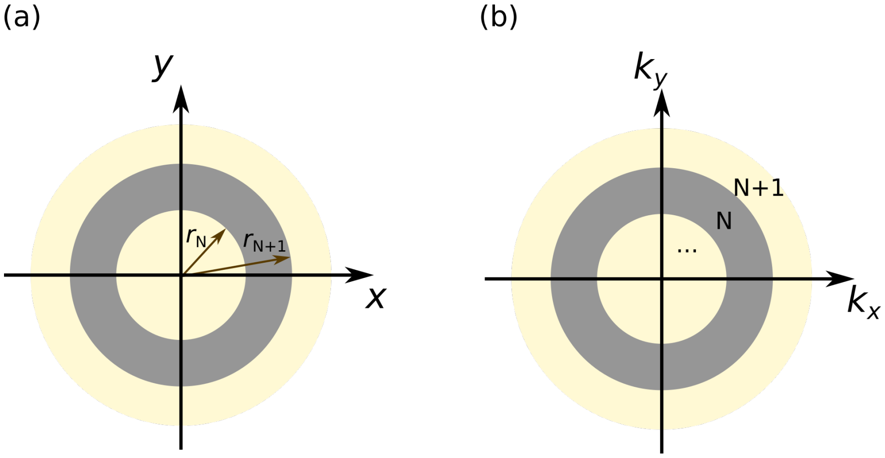

Figure 3.6: Quantization of electron orbits in real and k spaces ((a) and (b)). The orbital radiuses are described by eq. 3.58 in real space.

The number of available states (degeneracy) for a given Landau level can be estimated in either the real or k spaces since quantization exhibits itself in both (fig. 3.6). $r(N)$ can be used in a purely geometrical calculation by comparing its corresponding orbital area to the overall area of the sample S:

$$g_{2D} = \frac{S}{S_{N+1} - S_N} = \frac{S}{\pi(r_{N+1}^2 - r_N^2)} = \frac{S}{2\pi l_b^2} = \underbrace{SB}_{\Phi}\underbrace{\frac{e}{h}}_{\Phi_0} = \frac{\Phi}{\Phi_0}, \tag{3.59}$$

where Φ denotes the magnetic flux. The quantity Φ_0, defined purely by the fundamental physical constants, is the **magnetic flux quantum** and determines the lowest portion by which the magnetic flux through a current-carrying loop can be changed. Thus, the degeneracy is the same for all Landau levels. For N Landau levels present in the system, the degeneracy is then $N(\Phi/\Phi_0)$.

The quantity describing the amount of available energy levels at a particular energy is the density of states (DOS). To obtain the 3D DOS, we note that the electron is free to move in the z direction while constrained in xy. Therefore, we scan over all affected two-dimensional cases for each unconstrained 1D case:

$$g_{3D}(E) = 2\int_0^E g_{xy}(E_{xy}) g_z(E - E_{xy}) \mathrm{d}E_{xy}. \tag{3.60}$$

In the z direction, the DOS is that of a one-dimensional free particle (fig. 3.8, (b)):

$$g_z(E) = \frac{1}{2\pi}\sqrt{\frac{2m_{\mathrm{eff}}}{\hbar^2 E}}. \tag{3.61}$$

If the movement was unconstrained (i.e. the magnetic field is off), the DOS in the xy plane would be that of a free two-dimensional particle:

$$g_{xy}(E) = \frac{m_{\mathrm{eff}}}{2\pi\hbar^2}, \tag{3.62}$$

which would bring us to the well-known DOS of a free particle:

$$g_{3D}(E) = \frac{1}{2\pi^2}\left(\frac{2m_{\mathrm{eff}}}{\hbar^2}\right)^{3/2}\sqrt{E}. \tag{3.63}$$

However, in the presence of magnetic field, the DOS in the xy plane is equal to a series of Landau levels described by eq. 3.59. Since the levels are distributed equidistantly, their energy-dependent degeneracy consists of a series of δ functions separated by $\hbar\omega_c$ (fig. 3.8, (a)), and the resulting three-dimensional DOS is (fig. 3.8, (c))

$$g_{3D}(E, B) = \frac{1}{4\pi^2}\left(\frac{2m_{\mathrm{eff}}}{\hbar^2}\right)^{(3/2)} \hbar\omega_c \sum_{N=0}^{N_{max}} \frac{1}{\sqrt{E - E_N}}. \tag{3.64}$$

One can estimate the conditions required for the Landau quantization to be observable:

- regarding the **temperature**, the energy quantization is required to be greater than the thermal excitations of the environment: $\hbar\omega_c \gg k_B T$. In other words, this requires *strong magnetic fields* and/or *very low temperatures* (in the order of a few Kelvins);

- in terms of **scattering** of electrons, real samples are imperfect and include impurities. If the duration of the scattering event is τ, then, according to the uncertainty principle, the associated energy broadening is $\Delta E = \hbar\tau$. For the Landau quantization to be greater, this translates to $\omega_c\tau = \mu B \gg 1$. Therefore, *exceptionally pure samples* or *high enough fields* are needed.

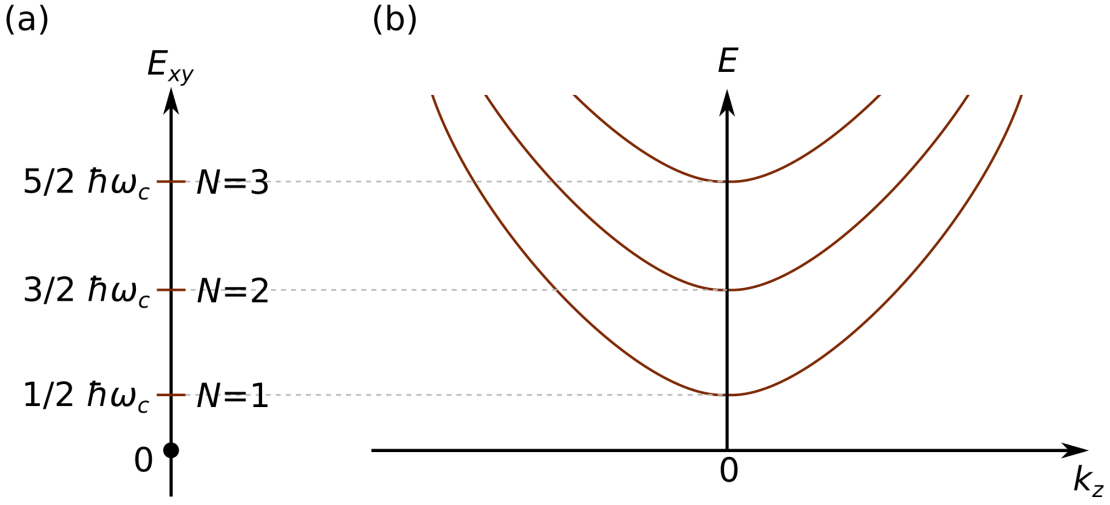

Figure 3.7: Energy spectrum of electron in an external magnetic field pointing along z direction: appearance of quantized Landau levels in two-dimensional case (a) and the resulting full three-dimensional dispersion (b).

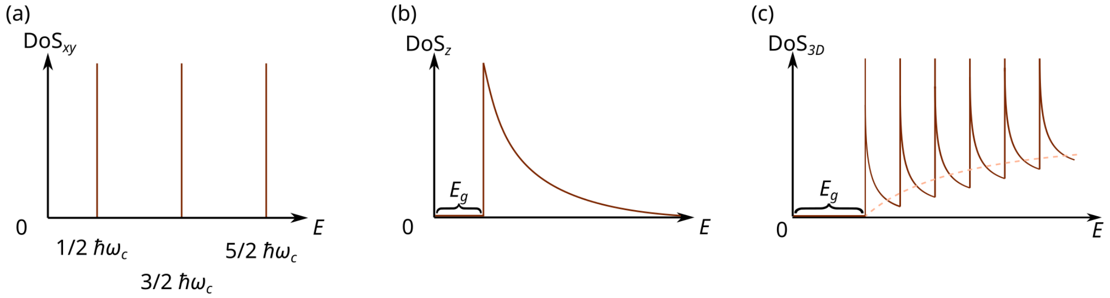

Figure 3.8: Qualitative decomposition of DoS along all directions in a sample. DoS in the xy plane consisting of equidistantly distributed δ functions separated by $\hbar\omega_c$ (a). One-dimensional free particle DoS in the z direction (b). The resultant three-dimensional DoS with the magnetic field on (c). Dashed line marks the DoS of a free particle (magnetic field off).

3.2.4 Quantum Hall effect

At very high magnetic fields, when the Landau quantization becomes substantial, the Hall conductivity σ_{xy} (or resistivity ρ_{xy}, see fig. 3.9) becomes quantized as the magnetic field is swept. This is the **quantum Hall effect**:

$$\sigma_{xy} = \nu \frac{e^2}{h}. \tag{3.65}$$

ν is called the filling factor and is defined as $\nu = N_e/N_\Phi$, where $N_e = N(\Phi/\Phi_0)$ is the number of electrons in Landau levels (the same as degeneracy) and $N_\Phi = \Phi/\Phi_0$ is the number of enclosed magnetic flux quanta. When ν is an integer number, this is the *integer quantum Hall effect.* Also possible is the *fractional quantum Hall effect*, in which $\nu < 1$.

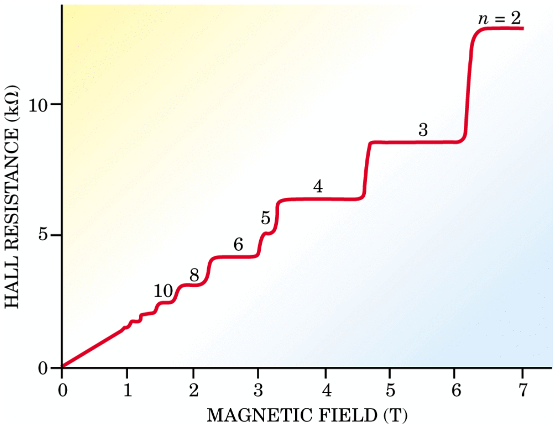

Figure 3.9: Resistivity plateaus observed in the integer quantum Hall effect of the two-dimensional electron gas [4].

To understand the mechanism of the quantum Hall effect, it is necessary to include a more realistic density of states of the 2D electron gas under the magnetic field. They are always broadened by impurities and temperature. When the highest Landau level is completely filled the Fermi energy and the chemical potential must be in the gap between this and the higher level (fig. 3.10, a). There are no more allowed states for the electrons to move in the vicinity, and the sample longitudinal conductivity σ_{xx} is zero. This happens when

$$n_e = \nu \frac{2eB}{h}, \tag{3.66}$$

where n_e is the electron concentration and ν is an integer number. On the other hand, if the level is half-filled, there are enough states just above the chemical potential, and the sample exhibits high longitudinal conductivity ρ_{xx} (fig. 3.10, b). This happens when

$$n_e = \left(\nu + \frac{1}{2}\right) \frac{2eB}{h}. \tag{3.67}$$

When the magnetic field is low and the Landau levels are densely packed, the overall DOS overlaps and forms an oscillatory pattern (fig. 3.11, a). As the field is swept, the oscillations shift, and the DOS around the Fermi energy E_F oscillates together, causing the electrical properties of the sample to oscillate as well. This

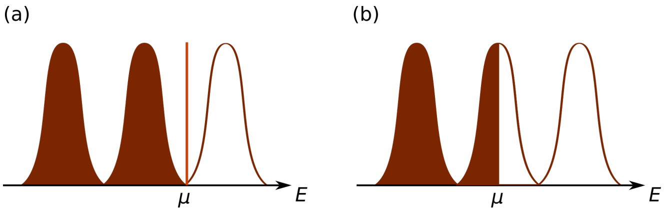

Figure 3.10: The effect of realistic Landau level density of states on the electronic properties when the highest level is completely (a) and partially (b) filled.

gives rise to **Shubnikov–de Haas oscillations** of the conductivity. They are periodic in B, with the periodicity

$$\Delta\left(\frac{1}{B}\right) = \frac{2e}{nh}. \tag{3.68}$$

At high magnetic fields, level separation becomes unambiguous. In order to understand the appearance of the *Hall plateaus* in either Hall conductivity or resistivity, inclusion of the *localised* and *delocalised* Landau level states is necessary. Close to the DOS peaks, the electrons are delocalised. At the tails, there exist the localised tail states, which do not contribute to the conduction. The boundary between these two states is called the mobility edge. Due to impurities and the irregularity of the dopant concentration in a real sample, the regions of filled Landau levels exist as separate 'puddles'. As the field is changed, their size changes because the position of the Fermi energy/chemical potential with respect to the closest Landau levels changes. Once in the localised states, those islands interconnect so that the current can flow, contributing to conductivity. As the Fermi energy starts approaching the next Landau level over the localised states, the puddles of occupied Landau levels change once again, becoming disconnected and thus making the conductivity stay constant.

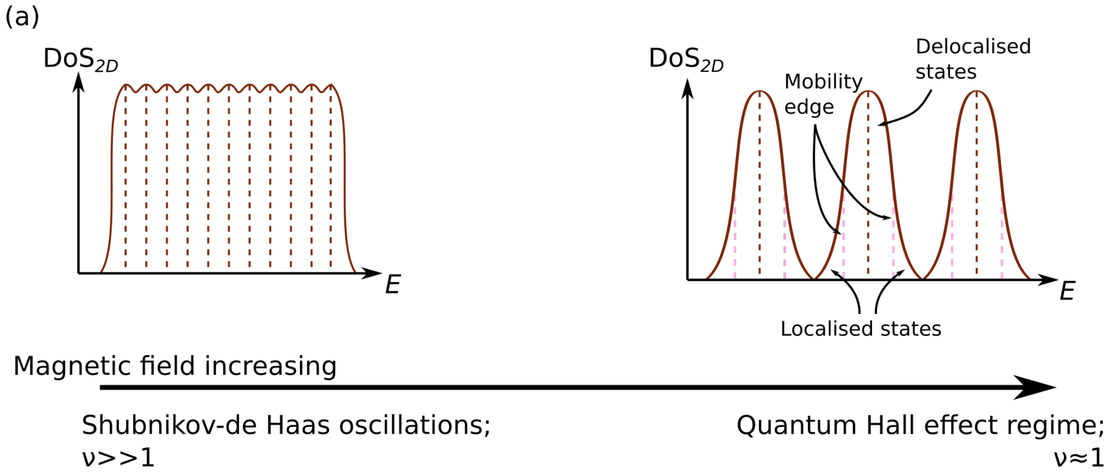

Figure 3.11: Densely packed Landau level density of states, giving rise to Shubnikov-de Haas oscillations (a). At high magnetic fields, the levels are well-separated. This is the quantum Hall effect regime (b).

3.2.5 FTIR Landau level spectroscopy

The middle and deep IR wavelengths are where vibratory molecular transitions take place. It is said that this region contains the vibratory 'fingerprints' of chemical elements. This allows examining the composition of chemical compounds from gases to organics [75, 76]. In the context of solid state physics, it allows to probe spectral properties in the vicinity of the bandgap of narrow-gapped materials. Combined with an external magnetic field, it enforces Landau quantization of the charge carriers, making possible to directly probe the properties of the band structure. This is the essence of the **Landau level spectroscopy**.

In straightforward implementation, spectroscopic measurements would be performed by selecting a narrow spectral window with a monochromator and registering the signal with a single detector. This made the process rather slow if a wide spectral region was to be measured. The advent of CCD detectors and use of diffractive elements made an instantaneous acquisition of an entire spectra possible. This is especially applicable for VIS spectral region which is nowadays readily measured using pocket-sized consumer level spectrometers [77, 78].

For IR wavelengths, however, another measurement concept proved the most efficient. It employs modulating the beam in spatial domain and registering the resulting signal with a single detector. The beam is guided using reflective optical elements that introduce minimum loss and no dispersion. All these factors mean that the entire beam and all of its spectral components are detected at all times, greatly improving the Signal-to-Noise Ratio (SNR) and acquisition speed (the latter determined purely by modulation period). For physicists, these are known as Fellgett's and Jacquinot's advantages.

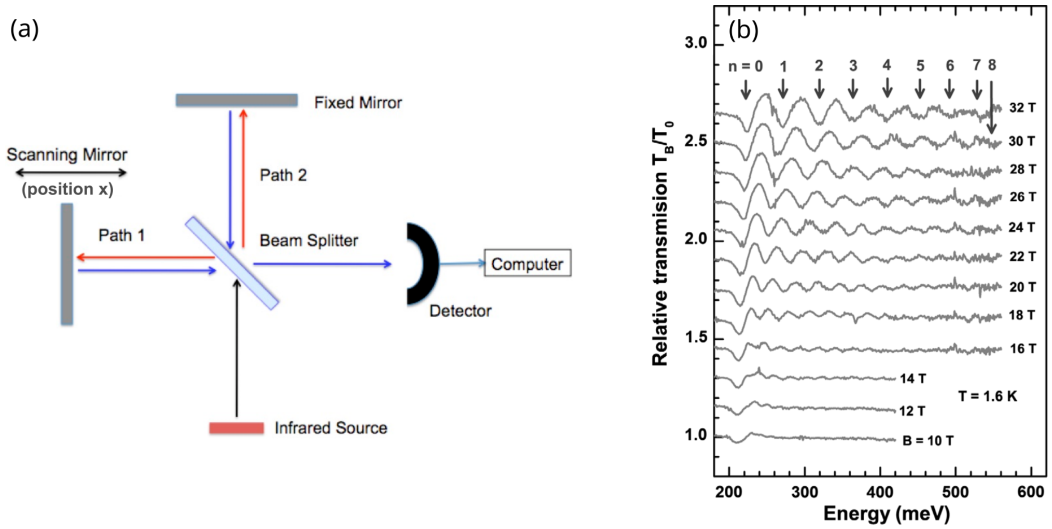

Figure 3.12: Essential parts of a FTIR spectrometer based on Michelson interferometer (a, based on [79]). The length of one of the arms is modulated harmonically (denoted by the x). An example of real data obtainable using this technique: stacked magneto-transmission graph of Bi_2Se_3 topological insulator plotted for selectad values of magnetic field with Landau level indices (based on [80]).

The most popular experimental setup is based on the Michelson interferometer. The modulation is applied by changing the length of one of its arms in a harmonic fashion (fig. 3.12). This enforces interference between the spectral components of the beam, and the registered intensity I at the position of the moving arm x is

$$I(x) = S(\nu)\cos(2\pi\nu x), \tag{3.69}$$

where the quantity called the wavenumber $\nu = 1/\lambda$ is introduced and λ is the wavelength. $S(\nu)$ is the intensity of the monochromatic line located at a particular ν. Consequently, the acquired signal is called **the interferogram**. It requires Fourier-transforming it to recover the spectrum. A complete process flow requires some other intermediate operations such as apodisation (to suppress spectral leakage), phase correction (to convert a complex-valued spectrum to real-valued) etc. [81]. This functionality is provided by default by the software of modern devices.

IV PbSnSe material

4.1 Topological Hamiltonian

A general introduction to Landau quantization was given in previous sections. In this part, both a thorough theoretical framework will be developed as well as real experiments will be discussed and interpreted for a particular material investigated in this thesis, the lead tin salts.

In order to estimate the precise transition energies and thus be ready to interpret the experimental data, the theory needs to be adapted to a particular material, taking their physical properties of interest such as their atomic structure into account. Only then can we obtain the exact density of states, energies of the conduction and the valence bands etc. In other words, what is eventually needed is a suitable model Hamiltonian.

Here we are going to review the Hamiltonians derived explicitly for lead salts as well as other closely related materials, each having their own advantages but dealing with different subsets of the phenomena. Afterwards, we are going to propose our own model Hamiltonian bridging the strong parts of those examples so that it would contain both the essential physics and topological information.

4.1.1 Hamiltonian for lead salts

The first quantum mechanical models to properly describe the properties of the lead salts were developed as early as 1960s [82], taking the symmetries around L point into account. Understandably, the notion of the non-trivial topological states of matter did not exist back then nor in the early 90s [83], and the Hamiltonians to be presented here only deal with the ordinary energy bands. These models were developed on the basis of the $\vec{k}\cdot\vec{p}$ theory. It expands the Hamiltonian in the powers of k round the chosen Brillouin zone point (the L point). It then includes the lowest conduction and the highest valence bands exactly, but the other remaining bands are taken into account in approximation to higher order k terms.

4.1.1.1 Symmetries of the lead salts

When the spin-orbit interaction is excluded, the Bloch functions at the L point of the NaCl lattice are single-group nondegenerate representations of the group D_{3d} if the spin is neglected, and which transform like $L_1^{\pm}$, $L_2^{\pm}$. The double degenerate representations transform like $L_3^{\pm}$. Because of inversion symmetry, there will be an even (+) and odd (-) representation for each class.

When the spin-orbit interaction is included, the states around the L point have $L_6^{\pm}$ or $L_{4,5}^{\pm}$ symmetry. The L_6 states are doubly-degenerate while L_4 and $L-5$ are singly degenerate, yet have twofold Kramers degeneracy at each L point, which is preserved at all points in the Brillouin zone of the NaCl type of crystal lattice. The spin-orbit coupling also mixes $L_6^{\pm}$-symmetrical states originating from different single-group states (representations of the group D_{3d} describing the transformation properties of the Bloch functions in a crystal). This mixing allows coupling of the longitudinal and transverse components of the momentum matrix elements, thus resulting in spherical or nearly spherical bands from $\vec{k}\cdot\vec{p}$ interaction of a single pair of levels at the L point [82].

According to the Mitchell and Wallis notation, the band-edge periodic functions for the valence bands $V^{\pm}$ at the L point exhibit the $\mathrm{L}_{61}^{\pm}$ symmetry [83]:

$$V^{+} = i\cos\theta^{+} R\uparrow + \sin\theta^{+} S_{+}\downarrow, \tag{4.1}$$

$$V^{-} = i\cos\theta^{+} R\downarrow + \sin\theta^{+} S_{-}\uparrow. \tag{4.2}$$

The conduction states $C^{\pm}$, however, have different symmetry. In case of PbSe, it is L_{62}^{-} in Bernick and Kleimann notation and L_{61}^{-} in Mitchell-Wallis notation:

$$C^{+} = i\cos\theta^{-} Z\uparrow + \sin\theta^{-} X_{+}\downarrow, \tag{4.3}$$

$$C^{-} = i\cos\theta^{-} Z\downarrow + \sin\theta^{-} X_{-}\uparrow. \tag{4.4}$$

The parameters $\cos\theta^{\pm}$ and $\sin\theta^{\pm}$ are given by different combinations of energy gaps and spin-orbit energies. The positive and negative subscripts ± denote the partners of a Kramers pair and do not correspond to pure spin states. The spin functions $\uparrow$ and $\downarrow$ correspond to the eigenstates of σ_z in the atomic coordinate system. It is oriented so that z lies along the [111] axis of the valley, x along $[\bar{1}\bar{1}2]$ and y along $[1\bar{1}0]$. Furthermore, R is isotropic (it is an atomic s state), $X_{\pm}$ and Z transform like the atomic p functions with $m_z = \pm 1$ and $m_z = 0$, and $S_{\pm}$ transform like the atomic d functions with $m_z = \pm 1$ [82].

4.1.1.2 Topologically trivial lead salts in magnetic field

The standard eigenvalue problem is solving the Schrödinger equation with the external magnetic field present:

$$\left(\frac{1}{2m_0}\vec{p}^{2} + V_0(\vec{r}) + H_{SO}\right)\Psi = E\Psi, \tag{4.5}$$

where $V_0(\vec{r})$ is the periodic potential of the lattice, H_{SO} is the spin-orbit interaction term, $\vec{p}$ is the momentum which in the presence of external magnetic field is augmented with the vector potential $\vec{A}$, $\vec{p} \rightarrow \vec{P} = \vec{p} + e\vec{A}$.

In a simplified treatment by Bauer [83], the solutions are sought in the form

$$\Psi = \sum_{l} f_l(\vec{r}) u_l(\vec{r}), \tag{4.6}$$

where f_l are slowly varying envelope functions and $u_l(\vec{r})$ are periodic Luttinger-Kohn (L-K) functions at the band extrema, which for the lead salts in the L point. The summation runs over the energy bands. At the band edges, the L-K functions satisfy the eigenvalue problem

$$\sum_{l} H_{l'l} f_l = E f_l', l' = 1, 2, ..., \tag{4.7}$$

where l' runs over the energy bands. The explicit expression of the $H_{l'l}$ up to the second order in $\vec{P}$ is

$$H_{l'l} = \left(\epsilon_{l0} + \frac{1}{2m_0}P^2\right)\sigma_{l'l} + \frac{1}{m_0^2}\sum_{\alpha\beta=1}^{3} A_{l'l}^{\alpha\beta} P_\alpha P_\beta + \frac{1}{m_0}\vec{\pi}_{l'l}\cdot\vec{P} + \mu_B \vec{B}\cdot\vec{\sigma}_{l'l}, \tag{4.8}$$

where l' and l are band indices, α and β are the Cartesian coordinates, ϵ_{l0} are the band-edge energies and $\vec{\pi}_{l'l} = \langle u_{l'} | \, \vec{\pi} \, | u_l \rangle$ are the matrix elements of

$$\vec{\pi} = \vec{p} + \frac{\hbar}{4m_0c^2}(\vec{\sigma} \times \nabla V_0), \tag{4.9}$$

and $\sigma_{l'l} = \langle u_{l'} | \, \vec{\sigma} \, | u_l \rangle$ with $\vec{\sigma}$ being the Pauli spin operators, $\vec{B}$ the magnetic field and μ_B the Bohr magneton.

Owing to the symmetries, for two conduction and two valence bands, the corresponding Hamiltonian is

$$H_{l'l} = \begin{pmatrix} \hat{V}^+ & \frac{1}{2}g_t^+\mu_B B_x & v_l P_z & \sqrt{2}v_t P_- \\ \frac{1}{2}g_t^+\mu_B B_x & \hat{V}^- & \sqrt{2}v_t P_+ & -v_l P_z \\ v_l P_z & \sqrt{2}v_t P_- & \hat{C}^+ & \frac{1}{2}g_t^-\mu_B B_x \\ \sqrt{2}v_t P_+ & -v_l P_z & \frac{1}{2}g_t^-\mu_B B_x & \hat{C}^- \end{pmatrix}, \tag{4.10}$$

with

$$\hat{V}^{\pm} = \frac{-E_g}{2} - \frac{P_x^2 + P_y^2}{2m_t^+} - \frac{P_z^2}{2m_l^+} \pm \frac{1}{2}g_l^+\mu_B B_z^+, \tag{4.11}$$

$$\hat{C}^{\pm} = \frac{+E_g}{2} + \frac{P_x^2 + P_y^2}{2m_t^-} + \frac{P_z^2}{2m_l^-} \pm \frac{1}{2}g_l^+\mu_B B_z^+, \tag{4.12}$$

where μ_B is the Bohr magneton and $m_l^{\pm}$, $m_t^{\pm}$, $g_l^{\pm}$, $g_t^{\pm}$ denote the far-band contributions to the effective masses and the spin g-values, v_l, v_t are combinations of the $\vec{P} \cdot \vec{\pi}$ matrix elements with $\sin\theta^{\pm}$ and $\cos\theta^{\pm}$, and $P_{\pm} = (P_x \pm P_y)/\sqrt{2}$. The subscripts ± refer to the valence and conduction bands while t/l refer to the transverse and longitudinal projections [83]. The Hamiltonian derived by Mitchell and Wallis share similar expressions [82].

4.1.2 Hamiltonian for $\mathbf{Bi_2Se_3}$ topological insulators

Zhang and Liu succeeded in developing an early Hamiltonian applicable to topological insulators [84, 85]. Originally, it was developed for Bi_2Se_3 family of two-compound materials which are stoichiometric crystals with well-defined electronic structures and simple surface states, making them describable by modest theoretical models. Even though Bi_2Se_3 exhibits Dirac cones at the Γ point (unlike the L point in the case of the lead salts), this Hamiltonian deserves attention as an historical example of the first successful Hamiltonian for topological insulators. Moreover, we will show that under certain assumptions, this Hamiltonian is highly adaptive and can be connected to the lead salts as well.

4.1.2.1 The main interacting orbitals

As the band structure is determined by the outmost orbitals, only they can be considered. The electronic configuration of Bi is $6s^2 6p^3$ and that of Se is $4s^2 4p^4$, therefore, only p orbitals are sufficient to be examined. The same applies to lead tin salts as the outmost orbitals of both Pb, Sn and Se are of p type.

In the case of bismuth selenide, there are 5 atoms per quintuple layer, each atom having 3 p orbitals (p_x, p_y, p_z), there are 15 orbitals in total. This is how they

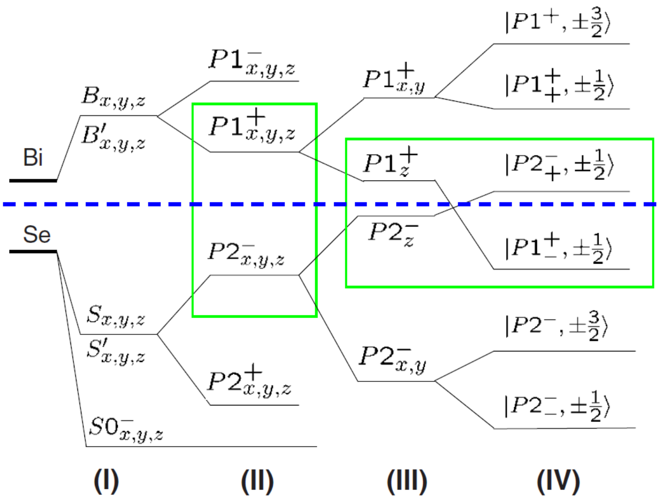

Figure 4.1: Evolution of p orbitals in Bi_2Se_3 topological insulator: hybridization of Bi and Se orbitals (I), formation of bonding and anti-bonding states (II), crystal field splitting (III), addition of the spin-orbit interaction which finally gives rise to band inversion, a signature feature of topological insulators (IV). From [85].

interact and give rise to the observed energy band structure (each step pictured in fig. 4.1):

- the strongest coupling is between Bi and Se layers, causing level repulsion (I);
- because of the inversion symmetry, they then form the bonding and anti-bonding orbitals (II);
- as a result of the layered crystal structure (unequivalence between z and x or y directions), there is an energy splitting between p_z and p_{xy} orbitals, referred to as the 'crystal field splitting';
- the spin-orbit interaction (SOC) couples the orbital angular momentum to spin and causes additional level repulsion of the two pairs of $P1^+_-$ and $P2^+_-$ orbitals with the opposite parity, finally inverting the bands and generating the signature feature of topological insulators.

Therefore, at the end, in order to capture the essential physics of topological insulators, it is sufficient to only analyze the two pairs of inverted band orbitals. They are twice degenerate because of spin and form the basis of this four-band model Hamiltonian. Subsequently, they are labeled $|P1^+_-, +1/2\rangle = |\text{Se}\downarrow\rangle$, $|P2^-_+, +1/2\rangle = |\text{Bi}\uparrow\rangle$, $|P1^+_-, -1/2\rangle = |\text{Se}\uparrow\rangle$ and $|P2^-_+, -1/2\rangle = |\text{Bi}\downarrow\rangle$.

Of course, one can include additional basis vectors which describe couplings with other orbitals as well. In Liu's article, the eight-band Hamiltonian is derived for quantitative analysis [85]. Understandably, the model becomes more complex, with over 26 parameters which have to be meticulously tuned in order to achieve a good correspondence to reality. On the other hand, the general four-band model is sufficient to describe the main physics of topological insulators, namely the band inversion, in the low energy and long-wavelength regime.

4.1.2.2 Four-band Hamiltonian

Having resolved the basis (two bands corresponding to the valence and conduction band twice degenerate because of spin), the exact form of the Hamiltonian can be derived in several ways, both leading to the same result:

- from symmetry principles, or theory of invariants. It takes into account two-fold, three-fold and other rotational symmetries R_2, R_3, ... along different directions, inversion P, and time-reversal symmetry T present in the lattice.

  Any 4×4 Hamiltonian can be expanded by Dirac Γ matrices:

  $$\hat{H}_{eff} = \epsilon(\vec{k}) I_{4x4} + \sum_i d_i(\vec{k})\Gamma_i + \sum_{ij} d_{ij}(\vec{k})\Gamma_{ij}, \tag{4.13}$$

  where I_{4x4} is the 4x4 identity matrix and $\Gamma_i (i = 1, ..., 5)$ are the five Dirac Γ matrices. They satisfy $\Gamma_i, \Gamma_j = 2\delta_{ij}$ and their ten commutators are $\Gamma_{ij} = [\Gamma_i, \Gamma_j]/2i$. Taking the symmetries of the system into account, the effective Hamiltonian up to $O(k^3)$ is

  $$H_{eff} = H_0 + H_3, \tag{4.14}$$

  where H_0 preserves the in-plane rotation symmetry along the z direction and H_3 breaks it down to the threefold rotation symmetry:

  $$H_0 = \epsilon(\vec{k}) + M(\vec{k})\Gamma_5 + B(k_z)\Gamma_4 k_z + A(k_x^2 + k_y^2)(\Gamma_1 k_y - \Gamma_2 k_x), \tag{4.15}$$

  and

  $$H_3 = R_1 \Gamma_3 (k_x^3 - 3k_x k_y^2) + R_2 \Gamma_4 (3k_x^2 k_y - k_y^3), \tag{4.16}$$

  where $\epsilon(\vec{k}) = C_0 + C_1 k_z^2 + C_2(k_x^2 + k_y^2)$, $M(\vec{k}) = M_0 + m_1 k_z^2 + M_2(k_x^2 + k_y^2)$, $A(k_x^2 + k_y^2) = A_0 + A_2(k_x^2 + k_y^2)$ and $B(k_z) = B_0 + B_2 k_z^2$.

- from $\vec{k} \cdot \vec{p}$ theory, which expands the Hamiltonian in the powers of k in the vicinity of a chosen Brillouin zone point (Γ in case of Bi_2Se_3 and L in case of lead tin salts as these are the points exhibiting the Dirac cones). It uses the wave function around those points as the zeroth-order wave function and treats $\hat{H}' = \hbar/m_0 \vec{k} \cdot \vec{p}$ as perturbation. p is the momentum operator and k is regarded as a small parameter for the perturbation procedure.

The two descriptions are equivalent and the corresponding Hamiltonians H_{symm} and $H_{\vec{k}\cdot\vec{p}}$ can be exchanged with the aid of this transformation [85]:

$$H_{\vec{k}\cdot\vec{p}} = U_1 H_{symm} U_1^\dagger, \tag{4.17}$$

where U is

$$U = \begin{pmatrix} 1 & 0 & 0 & 0 \\ 0 & -i & 0 & 0 \\ 0 & 0 & 1 & 0 \\ 0 & 0 & 0 & i \end{pmatrix}. \tag{4.18}$$

The immediate result is the explicit expression of the Hamiltonian which can be straightforwardly applied for the bulk states:

$$H = H_{bulk} = \epsilon(\vec{k}) I_{4\times4} + \begin{pmatrix} M(\vec{k}) & A(k)k_+ & 0 & -B(k_z)k_z \\ A(k)k_- & -M(\vec{k}) & b(k_z)k_z & 0 \\ 0 & B(k_z)k_z & M(\vec{k}) & A(k)k_- \\ -B(k_z)k_z & 0 & A(k)k_+ & -M(\vec{k}) \end{pmatrix}, \tag{4.19}$$

where $\epsilon(\vec{k}) = C_0 + C_1 k_z^2 + C_2 k^2$, $I_{4\times4}$ is the 4 × 4 identity matrix, $M(\vec{k}) = M_0 + M_1 k_z^2 + M_2 k^2$, $B(k_z) = B_0 + B_2 k_z^2$, $A(k) = A_0 + A_2 k^2$, $k_\pm = k_x \pm i k_y$ and $k^2 = k_x^2 + k_y^2$.

To describe the surface states, we note that k_x and k_y are still good quantum numbers but k_z is not [84]. The Hamiltonian (4.14) in the subspace $z > 0$ is divided into two parts, one with all k_z-dependent terms and the rest:

$$\hat{H} = \widetilde{H}_0 + \widetilde{H}_1, \tag{4.20}$$

where

$$\widetilde{H}_0 = \widetilde{\epsilon}(k_z) + \widetilde{M}(k_z)\Gamma_5 + B_0\Gamma_4 k_z, \tag{4.21}$$

$$\widetilde{H}_1 = C_2(k_x^2 + k_y^2) + M_2(k_x^2 + k_y^2)\Gamma_5 + A_0(\Gamma_1 k_y - \Gamma_2 k_x) + H_3. \tag{4.22}$$

In these equations, $\widetilde{\epsilon}(k_z) = C_0 + C_1 k_z^2$ and $\widetilde{M}(k_z) = M_0 + M_1 k_z^2$. The eigenvalue equation is obtained by replacing k_z with $-i\partial_z$:

$$\widetilde{H}_0(k_z \to -i\partial_z)\Psi(z) = E\Psi(z), \tag{4.23}$$

which allows to find the one-dimensional eigenfunctions $\Psi_{k_x,k_y}(z)$ [84]. The Hamiltonian $\hat{H}_0$ is then block diagonal with the eigenstates

$$\Psi_\uparrow(z) = \begin{pmatrix} \psi_0 \\ \vec{0}_2 \end{pmatrix}, \Psi_\downarrow(z) = \begin{pmatrix} \vec{0}_2 \\ \psi_0 \end{pmatrix}, \tag{4.24}$$

$\vec{0}_2$ being the two-component zero vector. $\Psi_\uparrow(z)$ and $\Psi_\downarrow(z)$ are related by the time-reversal operation. For surface states, $\psi_0(z)$ should be localized at the surface and satisfy the eigen equation

$$(\widetilde{\epsilon}(-i\partial_z) + \widetilde{M}(-i\partial_z)\tau_3 - iB_0\tau_2\partial_z)\psi_0(z) = E\psi_0(z), \tag{4.25}$$

where τ are the Pauli matrices. The wavefunction at the Γ point is then $\psi_0 = \phi e^{\lambda z}$, where

$$\psi_0 = \begin{cases} a(e^{\lambda_1 z} - e^{\lambda_2 z})\phi_+, & B_0/M_1 > 0, \\ a(e^{-\lambda_1 z} - e^{-\lambda_2 z})\phi_-, & B_0/M_1 < 0. \end{cases} \tag{4.26}$$

In the above expressions, a definition $\tau\phi_\pm = \pm\phi_\pm$ was introduced. The surface states Hamiltonian gives rise to helical spin textures, similarly to how helicity was an outcome of the Dirac Hamiltonian (fig. 4.2).

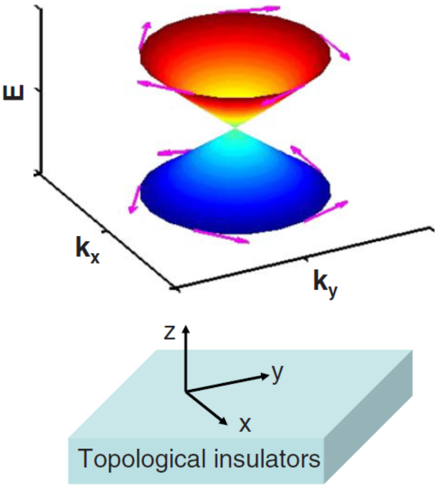

Figure 4.2: Three-dimensional plot of the spin texture of the surface states at the Γ point in momentum space. Left-handed helicity of the conduction band and right-handed helicity of the valence band is apparent [85].

4.2 Dirac Hamiltonian for topological insulators

Although derived from different principles and driven by different goals, all previously mentioned Hamiltonians share the same structure. In fact, they are all *Dirac-like*. Let's see how we could translate the original Dirac Hamiltonian describing a free particle to describe the topological semiconductor physics. The Dirac Hamiltonian already exhibits most of the features needed for this purpose:

- a forbidden gap;
- a universal dispersion model capable of describing both the usual parabolic energy bands in the case of ordinary materials as well as the linear Dirac cones of ultra-relativistic particles.

It should therefore be possible to apply it to ordinary semiconductors by:

- replacing the gap of $2m_0c^2$ (originating from the existence of the rest energy mass) with the standard semiconductor gap E_g. For convenience, we will adopt the notion of the **half gap** $\Delta = E_g/2$ to replace m_0c^2;
- similarly to how the free electron mass m_0 is replaced by the effective mass m_{eff} to reflect the effect of the periodic crystal and keep the potential term V out of the Schrödinger equation, the speed of light c can be replaced by its effective value in the material, the Fermi velocity v_F;
- the momentum p can be replaced by the wave-vector owing to the quantum-mechanical relation $p = \hbar k$.

The Dirac Hamiltonian then takes the following form:

$$\hat{H}_{Dirac} = \begin{pmatrix} \Delta & 0 & \hbar v_F k_z & \hbar v_F k_- \\ 0 & \Delta & \hbar v_F k_+ & -\hbar v_F k_z \\ \hbar v_F k_z & \hbar v_F k_- & -\Delta & 0 \\ \hbar v_F k_+ & -\hbar v_F k_z & 0 & -\Delta \end{pmatrix}, \tag{4.27}$$

where we also adopted the notion $k_{\pm} = k_x \pm i k_y$. The basis functions ψ obviously describe the valence and conduction bands V and C, each doubly degenerate because of spin:

$$\psi = \begin{pmatrix} |C_{\uparrow}\rangle \\ |C_{\downarrow}\rangle \\ |V_{\uparrow}\rangle \\ |V_{\downarrow}\rangle \end{pmatrix}. \tag{4.28}$$

The eigen energies are then

$$E_{eig}(\vec{k}) = E_{C,V}(\vec{k}) = \pm\sqrt{\Delta^2 + \hbar^2 v_F^2 k^2}. \tag{4.29}$$

This general Dirac Hamiltonian, however, so far does not include any information related to the topology. Comparing this Dirac Hamiltonian to Liu's (eq. 4.19), we can deduce the meaning of its coefficients:

- $M_{0,1,2}$ is related to the curvature of the bands. In particular, for small values of $M_{1,2}$, the band gap approaches $2M_0$; we can therefore conclude that $\Delta := M_0$. Strictly speaking this is valid only for strong coupling between bands with only one extreme (at $k = 0$).
- $A_{0,1,2}$ and $B_{0,1,2}$ are related to the in-plane and out-of-plane effective speeds of electrons $v_{x,y}$ and v_z, allowing to include the effects of anisotropy;
- $C_{0,1,2}$ is related to the effective masses in xy and z directions. It causes asymmetry between the electron and hole bands. C_0 acts as the general calibration of the zero energy. For convenience, we want to keep it at the middle of the gap, therefore setting $C_0 := 0$.

We notice that the two Hamiltonians could be consolidated if we further simplied 4.19 by neglecting k^3 terms. This essentially means that we are neglecting the shape of the bands further away from the chosen point of interest in the Brillouin zone. The meaning of the remaining coefficients then is:

- M_2 describes the band inversion and topology. We will define it as $M := M_2$. It is called the **diagonal dispersive term**. As long as the material is in the ordinary insulator state, the conduction band lies below and the valence band lies above the band gap. When the gap closes and reopens in the topological insulator regime, the conduction and valence bands flip, but a model without M is unable to describe this correctly. The only available approach is to empirically change the bandgap into negative (fig. 4.3, (a)). The M parameter allows to leave the fundamental parameter of a semiconductor - its bandgap - unchanged (fig. 4.3, (b)). In order to keep the band gap positive (only real values of energy are detectable experimentally), M should be negative for topologically nontrivial phases by convention.

  Therefore, the sign of M serves as a measure of the topological regime of the system:

  - the material is an ordinary insulator when $M > 0$;
  - in topological regime with inverted energy bands, $M < 0$ (fig. 4.3, (b)).

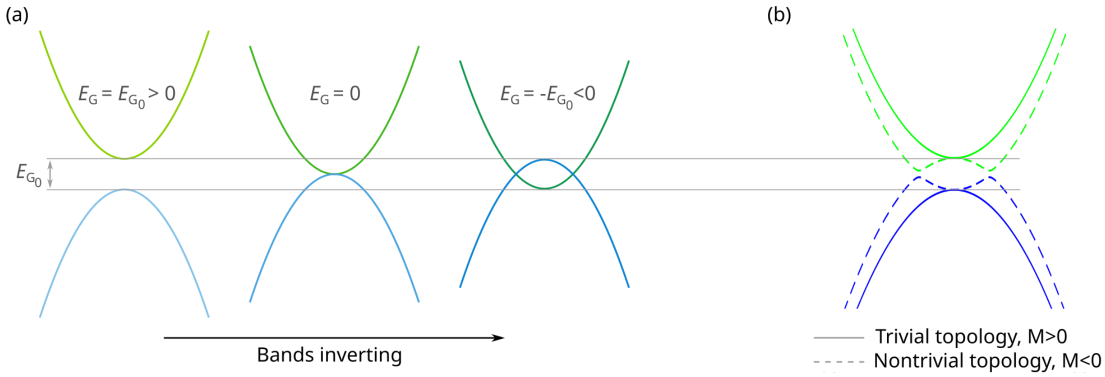

Figure 4.3: Meaning of the diagonal dipersive term M: in ordinary insulator, the valence band lies above the conduction band. In the topological phase, these bands flip, but a general Dirac Hamiltonian is unable to describe band inversion. The only way to introduce it is by meddling with the value of the bandgap (a). The band topology is captured by the sign of M (b), preserving the bandgap.

- the only remaining asymmetry term is C_2. If there was a difference between the electron and hole masses, the transitions $|N\rangle \to |N+1\rangle$ and $|N+1\rangle \to |N\rangle$ would exhibit different energies. We therefore name it the **electron-hole asymmetry term** and set $C := C_2$;

- with only linear off-diagonal terms remaining, $v_{x,y} := A_0/\hbar$ and $v_z := B_0/\hbar$. In the absence of anisotropy, $v_F := A_0/\hbar$.

We therefore adopt the following general isotropic (rotationally symmetric) 4×4 Hamiltonian to describe bulk topological insulators. It can be thought of as the Dirac Hamiltonian with the added band inversion and asymmetry terms:

$$\begin{pmatrix} \Delta + Mk^2 + Ck^2 & \hbar v_F k_+ & 0 & -\hbar v_F k_z \\ \hbar v_F k_- & -\Delta - Mk^2 + Ck^2 & \hbar v_F k_z & 0 \\ 0 & \hbar v_F k_z & \Delta + Mk^2 + Ck^2 & \hbar v_F k_- \\ -\hbar v_F k_z & 0 & \hbar v_F k_+ & -\Delta - Mk^2 + Ck^2 \end{pmatrix}. \tag{4.30}$$

This Hamiltonian could in principle be derived using the $\vec{k} \cdot \vec{p}$ theory around L point. In fact, it could be derived around any other point $\vec{k_0}$ of the Brillouin zone, but keeping the terms up to quadratic in the diagonal and linear in the off-diagonal elements would eventually lead to the same expressions as eqs. 4.27 and 4.30.

It is easy to determine its eigen energy dispersion by adding M to the Δ term and C term in front:

$$E_{C,V}(\vec{k}) = Ck^2 \pm \sqrt{(\Delta + Mk^2)^2 + \hbar^2 v_F^2 k^2}. \tag{4.31}$$

4.2.1 Topological Dirac Hamiltonian in magnetic field

We introduce the magnetic field via the usual Peierls substitution $\vec{k} \to \vec{q} := \vec{k} + \frac{e\vec{A}}{\hbar}$, where $\vec{A}$ is the vector potential. $B = \nabla \times \vec{A}$ and $B = (0, 0, B_z)$. We introduce the standard creation and annihilation operators a and $a^\dagger$ to study the formation of Landau levels:

$$a = \frac{l_B}{\sqrt{2}}\vec{q}_-, a^\dagger = \frac{l_B}{\sqrt{2}}\vec{q}_+, \tag{4.32}$$

obeying the well-known commutation relation:

$$[a, a^\dagger] = 1. \tag{4.33}$$

Their eigenvalues are

$$a\left|n\right\rangle = \sqrt{n}\left|n-1\right\rangle, \tag{4.34}$$

$$a^\dagger\left|n\right\rangle = \sqrt{n+1}\left|n+1\right\rangle \tag{4.35}$$

with the number state eigenvalue

$$a^\dagger a = n. \tag{4.36}$$

l_B in eq. 4.32 stands for the magnetic length:

$$l_B = \sqrt{\frac{\hbar}{eB}}. \tag{4.37}$$

The magnetic field only affects particle motion in the xy plane but leaves it unaffected in the z direction. Therefore, we can decompose $\vec{q}$ into its Cartesian components. We first invert eqs. 4.32 in order to recover $q_{x,y}$:

$$q_x = \frac{1}{\sqrt{2l_B^2}}(a^\dagger + a), q_y = \frac{-i}{\sqrt{2l_B^2}}(a^\dagger - a) \tag{4.38}$$

and then use them and the commutation relation 4.33 to decompose

$$q^2 = q_x^2 + q_y^2 + q_z^2 = \frac{2}{l_B^2}\left(\frac{1}{2} + a^\dagger a\right) + q_z^2. \tag{4.39}$$

The topological Hamiltonian thus changes into

$$\hat{H}_B(\vec{q}) = \begin{pmatrix} \Delta + M_q + C_q & \frac{\sqrt{2}\hbar v_F}{l_B}a^\dagger & 0 & -\hbar v_F q_z \\ \frac{\sqrt{2}\hbar v_F}{l_B}a & -\Delta - M_q + C_q & \hbar v_F q_z & 0 \\ 0 & \hbar v_F q_z & \Delta + M_q + C_q & \frac{\sqrt{2}\hbar v_F}{l_B}a \\ -\hbar v_F q_z & 0 & \frac{\sqrt{2}\hbar v_F}{l_B}a^\dagger & -\Delta - M_q + C_q \end{pmatrix} \tag{4.40}$$

where we marked the decomposed diagonal elements as

$$M_q = \frac{2M}{l_B^2}\left(\frac{1}{2} + a^\dagger a\right) + Mq_z^2 \tag{4.41}$$

and

$$C_q = \frac{2C}{l_B^2}\left(\frac{1}{2} + a^\dagger a\right) + Cq_z^2. \tag{4.42}$$

4.2.2 Hamiltonian with $k_z = 0$

Special consideration has to be paid for the case when the electron motion along the applied magnetic field can be neglected ($k_z = 0$). In such case, the full Hamiltonian 4.40 reduces to the block-diagonal form, two 2D Dirac-like Hamiltonians h and h^*:

$$H(k_z = 0) = \begin{pmatrix} h(a^\dagger, a) & 0 \\ 0 & h^*(a^\dagger, a) \end{pmatrix} \tag{4.43}$$

where h Hamiltonian, for instance, is

$$h(a^\dagger, a) = \begin{pmatrix} \Delta + \frac{2}{l_b^2}(C+M)(a^\dagger a + \frac{1}{2}) & \frac{\sqrt{2} v_F \hbar}{l_b} A_0 a^\dagger \\ \frac{\sqrt{2} v_F \hbar}{l_b} a^\dagger & -\Delta + \frac{2}{l_b^2}(C-M)(a^\dagger a + \frac{1}{2}) \end{pmatrix} \tag{4.44}$$

To find the solution, these wavefunctions are chosen:

$$\Psi_{N \neq 0} = \begin{pmatrix} c_1 \left| N \right\rangle \\ c_2 \left| N-1 \right\rangle \end{pmatrix}, \Psi_{N=0} = \begin{pmatrix} \left| 0 \right\rangle \\ 0 \end{pmatrix}, \tag{4.45}$$

providing the following solution:

$$E_{N,\alpha} = +\frac{M}{l_b^2} + 2\frac{C}{l_b^2}N + \beta\sqrt{\left(\frac{C}{l_b^2} + \Delta + 2\frac{M}{l_b^2}N\right)^2 + 2\frac{A_0^2}{l_b^2}N} \tag{4.46}$$

and

$$E_{0,e\downarrow} = \Delta + \frac{C+M}{l_b^2}. \tag{4.47}$$

The wavefunctions for h^* Hamiltonian are

$$\Psi_{N \neq 0} = \begin{pmatrix} c_1 \left| N-1 \right\rangle \\ c_2 \left| N \right\rangle \end{pmatrix}, \Psi_{N=0} = \begin{pmatrix} 0 \\ \left| 0 \right\rangle \end{pmatrix}, \tag{4.48}$$

and the solutions are

$$E_{N,\alpha} = -\frac{M}{l_b^2} + 2\frac{C}{l_b^2}N + \beta\sqrt{\left(\frac{C}{l_b^2} - \Delta - 2\frac{M}{l_b^2}N\right)^2 + 2\frac{A_0^2}{l_b^2}N} \tag{4.49}$$

and

$$E_{0,h\downarrow} = -\Delta + \frac{C+M}{l_b^2}. \tag{4.50}$$

$\beta = +1$ stands for electrons and $\beta = -1$ for holes. Note that these solutions imply a **full polarisation of the ground states**. Also worth noting is that the two diagonal sub-blocks h and h^* can be exchanged by the time reversal operation [86].

4.2.3 General Hamiltonian ($k \neq 0$)

The general solutions are sought in the form

$$\Psi_N = \begin{pmatrix} c_1 & \left| N \right\rangle \\ c_2 & \left| N-1 \right\rangle \\ c_3 & \left| N-1 \right\rangle \\ c_4 & \left| N \right\rangle \end{pmatrix}, \tag{4.51}$$

which transforms the Hamiltonian into

$$\hat{H}_B(\vec{q}) = \begin{pmatrix} D_1 & a & 0 & -\hbar v_F k_z \\ a & D_2 & \hbar v_F k_z & 0 \\ 0 & \hbar v_F k_z & D_3 & a \\ -\hbar v_F k_z & 0 & a & D_4 \end{pmatrix}, \tag{4.52}$$

where

$$a = \frac{\sqrt{2}\hbar v_F}{l_b}\sqrt{N}, \tag{4.53}$$

and the diagonal components $D_{1,2,3,4}$ are:

$$D_1 = +A + B + C + E_0, \tag{4.54}$$

$$D_2 = -A + B - C + E_0, \tag{4.55}$$

$$D_3 = +A - B - C + E_0, \tag{4.56}$$

$$D_4 = -A - B + C + E_0. \tag{4.57}$$

In the above equations, we have grouped the variables as follows:

$$A = \left(\Delta + Mk_z^2 + \frac{2M}{l_B^2}N\right), \tag{4.58}$$

$$B = \frac{M}{l_B^2}, \tag{4.59}$$

$$C = \frac{C}{l_B^2}, \tag{4.60}$$

$$E_0 = \left(Ck_z^2 + \frac{2C}{l_B^2}N\right). \tag{4.61}$$

The energy spectrum of quasiparticles described by the above Hamiltonian is $E_n = E_0 + \epsilon_n$, where ϵ_n is the spectrum of the following matrix:

$$\mathcal{H} = \begin{pmatrix} A+B+C & a & 0 & -\hbar v_F k_z \\ a & -A+B-C & \hbar v_F k_z & 0 \\ 0 & \hbar v_F k_z & A-B-C & a \\ -\hbar v_F k_z & 0 & a & -A-B+C \end{pmatrix}. \tag{4.62}$$

Getting the eigenvalues of the above equation, or $\mathcal{H}\Psi = \lambda\Psi$, is equivalent to solving $det(\mathcal{H} - \lambda I) = 0$ with I being the identity matrix. This implies the characteristic equation

$$\begin{aligned} &\lambda^4 - 2\lambda^2\left[B^2 + A^2 + C^2 + a^2 + (\hbar v_F k_z)^2\right] - \lambda \cdot 4ABC + \\ &+ \left[A^2 + B^2 - C^2 + a^2 + (\hbar v_F k_z)^2\right]^2 + 4(a^2C^2 - A^2B^2 - a^2B^2) = 0. \end{aligned} \tag{4.63}$$

It can only be reduced to biquadratic form and provide simple solutions for special cases $A = 0$, or $B = 0$, or $C = 0$. For general case with all nonvanishing terms, one should solve the equation of the 4th order. This can be done with Wolfram Mathematica software package, for instance.

Here we will use the liberty and mention in advance that we did not detect any secondary transition bands with different bending in our experiments. This implies that $C = 0$. In this case, a solution can be found, and it reads

$$E_B(N) = \alpha\frac{M}{l_B^2} + \beta\sqrt{\left(\Delta + \frac{2M}{l_B^2}N + Mk_z^2\right)^2 + \frac{2\hbar^2v_F^2}{l_B^2}N + \hbar^2v_F^2k_z^2}, \tag{4.64}$$

where $\beta = +1$ corresponds to the conduction and $\beta = -1$ to the valence band, and $\alpha = \pm1$ corresponds to the spin splitting.

The solutions for the ground states, on the other hand, are possible to find in the most general form described by eq. 4.40. For these states $N = 0$, because by definition $|N \leq 0\rangle = 0$, the ansatz solution has to be modified:

$$\Psi_{N=0} = \begin{pmatrix} c_1\,|N\rangle \\ 0 \\ 0 \\ c_4\,|N\rangle \end{pmatrix}. \tag{4.65}$$

Note that this again implies a full spin-polarisation of the ground states. For electrons, E_0 is fully polarised as $|\downarrow\rangle$ level while for holes it is fully $|\uparrow\rangle$ state. The corresponding Hamiltonian is simplified to a 2x2 matrix:

$$\hat{H}_{B|N=0}(\vec{q}) = \begin{pmatrix} \Delta + \frac{M}{l_B^2} + Mk_z^2 + \frac{C}{l_B^2} + Ck_z^2 & -\hbar v_F k_z \\ -\hbar v_F k_z & -\Delta - \frac{M}{l_B^2} - Mk_z^2 + \frac{C}{l_B^2} + Ck_z^2 \end{pmatrix}. \tag{4.66}$$

Its eigenenergies are

$$E_{N=0}(k_z) = \frac{C}{l_B^2} + Ck_z^2 \pm \sqrt{\left(\Delta + \frac{M}{l_B^2} + Mk_z^2\right)^2 + \hbar^2v_F^2k_z^2}. \tag{4.67}$$

4.2.4 Topological dispersion summary

To summarize, we have got the following dispersion formulas in the case of electron-hole asymmetry absence ($C = 0$):

$$E_B(N) = \alpha\frac{M}{l_B^2} + \beta\sqrt{\left(\Delta + \frac{2M}{l_B^2}N + Mk_z^2\right)^2 + \frac{2\hbar^2v_F^2}{l_B^2}N + \hbar^2v_F^2k_z^2}, \tag{4.68}$$

where $\beta = +1$ stands for valence and $\beta = -1$ for conduction bands, and $\alpha = \pm1$ for the spin projections. For holes in the fully polarised ground state

$$E^h_{N=0}(B) = +\sqrt{\left(\Delta + \frac{M}{l_b^2} + Mk_z^2\right)^2 + \hbar^2v_F^2k_z^2}, \tag{4.69}$$

while for the electrons

$$E^e_{N=0}(B) = -\sqrt{\left(\Delta + \frac{M}{l_b^2} + Mk_z^2\right)^2 + \hbar^2v_F^2k_z^2}. \tag{4.70}$$

4.2.5 Selection rules

The selection rules for the transitions between the LLs within the topological Hamiltonian can be analyzed using the perturbation and linear response theories [86], where the power absorbed by the system is analyzed via the Fermi golden rule:

$$P(\omega) = 2\pi\omega \sum_{\alpha,\beta} |F_{\alpha\beta}|^2 (f_\beta - f_\alpha)\delta(E_\alpha - E_\beta - \hbar\omega), \tag{4.71}$$

describing the rate of single-electron transitions $\beta \to \alpha$, applied to a single-particle Hamiltonian H_0 with eigenstates $E_{\alpha,\beta}$, occupational factors $f_{\alpha,\beta}$, and matrix element of perturbation between these states $F_{\alpha\beta}$, with a monochromatic perturbation. The vector potential is

$$A_x = -B_z y + \frac{cE_x}{i\omega} e^{-i\omega t} + c.c., A_y = A_z = 0, \tag{4.72}$$

with E_x being the electric field amplitude and 'c.c.' the complex conjungate. The perturbation corresponding to this potential is

$$F_e = \frac{ieE_x}{\omega} v_x, \vec{v} = \frac{1}{\hbar} \frac{\partial H_k}{\partial \vec{k}}\bigg|_{\vec{k} \to \vec{\pi}}, \tag{4.73}$$

with $\vec{\pi}$ denoting the Peierls substitution $\vec{k} \to \vec{\pi} = -i\nabla + (e/\hbar c)\vec{A}$ [86]. At $k_z = 0$, the nonvanishing matrix elements of F_e impose these selection rules:

$$n, s \to n \pm 1, s, \tag{4.74}$$

where s denotes the spin degree of freedom [86]. Moreover, if similar matrix element analysis is also carried within with the Kubo-Greenwood formalism (which will be used for theoretical spectral modeling further in the thesis) for the circularly polarised light in the view of h, h^* nomenclature [80, 86],

- in h Hamiltonian, $N \to N - 1$ transitions are dominant and active in left circular polarisation σ^+,
- in h^* Hamiltonian, $M \to N + 1$ transitions are dominant, active in right circular polarisation σ^-.

4.3 PbSnSe sample preparation

The recent advances and goals of any solid state material production process aims to prepare the purest monocrystalline layers with controlled composition and geometric structure. There are a few widely used techniques for that.

4.3.1 Molecular beam epitaxy

Molecular beam epitaxy uses evaporated focused molecular beams of the source materials directed to the substrate where they are deposited. It enables the growth of high-purity thin films, especially for III-V compound heterostructures. It achieves a perfect control of stoichiometry and doping profile, as well as structure changes on the scale of atomic layers [87]. The source materials are heated to sublimation point in Knudsen effusion cells (K-cells). They contain ultra-high purity elements in solid form such as elemental 99.999% bismuth, selenium etc. The ultra high vacuum ensures the transport of high purity materials to the surface. The growth process it precisely monitored. The latter is provided *in-situ* during growth by reflection high-energy electron diffraction (RHEED) using low angle of incidence. Film properties are deduced from the registered diffraction pattern. A simplified scheme of the growth reactor is shown in fig. 4.4. For more uniform growth, substrate can be continuously rotated. The source materials and substrate must have the same crystal structure and similar symmetry, as well as similar lattice parameters differing no more than 10% [88]. All these factors make the molecular beam epitaxy the most technically challenging and demanding [89].

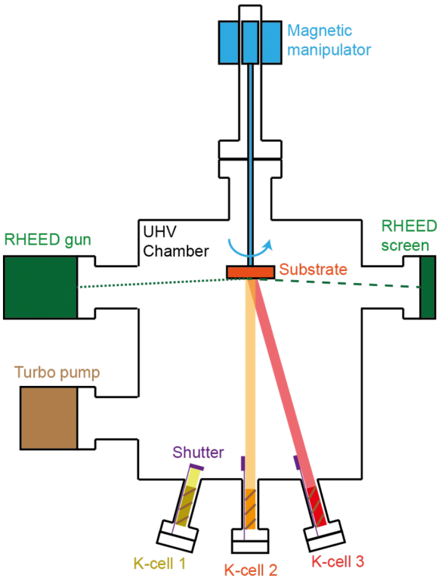

Figure 4.4: A simplified molecular beam epitaxy reactor system [89].

4.3.2 How wall epitaxy

In hot wall epitaxy, layers are grown as close as possible to thermodynamical equilibrium. This makes it very applicable for materials with Van der Waals binding character, for instance, organic epilayers [90]. The difference in epitaxial growth for inorganic and organic materials manifests in different bonding. The inorganic materials are first physisorbed and then chemisorbed on the growing surface. Organic materials are only physisorbed as no chemical bonds are formed between the molecules [90]. This method was used for preparation of high quality IV-VI films with carrier concentrations much lower than in the bulk since the 1980s [91]. The hot wall epitaxy belongs to the thermal evaporation class of material growth techniques. It is a vacuum layer deposition technique where the source material is first evaporated, then transported and deposited onto the substrate [91]. The hot wall is the region of the growth reactor between source and substrate. It guarantees a nearly uniform and isotropic flux of the molecules onto the substrate surface, as well as high vapor pressures. The advantage of such closed system is the minimization of source material losses, which might be crucial for materials not available commercially [90].

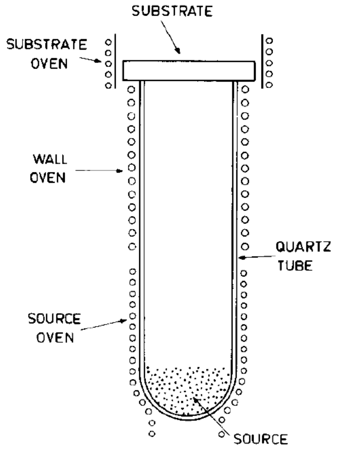

Figure 4.5: A simplified hot wall epitaxy reactor scheme [91].

4.3.3 Chemical vapor deposition

In this technique, the source materials are deposited owing to a chemical reaction between the precursors in a gas phase and a solid substrate that is typically heated. The solid films are formed by a heterogeneous reaction occurring at the substrate surface. It is synonymously said that the deposition is surface-mediated [92]. The reacting compounds can be either the original reagent chemicals fed to the system or short-lived intermediate species created in the high temperature gas phase [92]. The vapor, once transported to the substrate via fluid flow or diffusion, must remain there long enough so that it can react. The deposited atoms or molecules are migrating across the surface and can be trapped (and thus fixed in place) by impurities, atomic vacancies, lattice edges etc. Volatile byproducts must desorb from the surface to make space and are removed by a gas flow. Most CVD setups are oriented horizontally to control the gas flow. The system requires an inlfux of energy as the most important aspects are thermally driven. This is achieved by heating the substrate or plasma energy transfer to the reactants [92]. CVD is widely used to deposit materials in various forms from metals, semiconductor crystals, to coatings and polymers [93]. It is widely used in semiconductor industry to produce thin films.

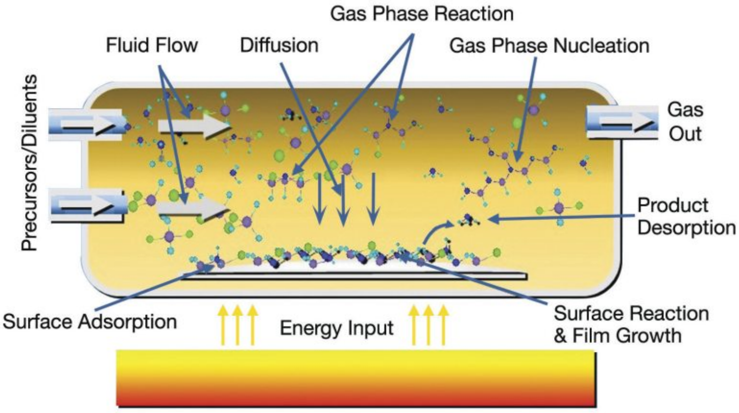

Figure 4.6: A simplified scheme of a chemical vapor deposition system [92].

4.3.4 $\mathbf{Pb_{1-x}Sn_xSe}$ sample production

The samples were produced by prof. Akihiro Ishida from Shizuoka university in Japan. They were grown using the hot wall epitaxy on a (111)-oriented BaF_2 substrate, weakly doped by bismuth to ensure n-type conductivity. The temperature of the substrate was 350°C, and the temperature of the PbSnSe source 550°C. Six samples were prepared, which we labelled A, B, C, D, E and F. The thickness of the epilayers ranged from 1 to 2.55 μm (table 4.1) while their lateral size measured about 1 cm (fig. 4.7). The X-ray diffraction analysis confirmed the (111) orientation of all PbSnSe layers (fig. 4.8). The nominal concentration of tin was chosen $x = 0.20$, 0.25 and 0.33. With this tin content, the samples are expected to have an inverted band structure at liquid helium temperatures. At chosen tin concentrations, the samples are still away from the crossover from the rocksalt to orthorhombic phase happening at $x \approx 0.4$ [94]. The carrier concentration was checked by Hall resistivity measurements at room temperature, and deduced from $R_H = 1/en$ relation.

Table 4.1: $Pb_{1-x}Sn_xSe$ sample nominal and measured parameters.

Sample	x	d (μm)	ρ (Ωcm)	μ (cm^2/V.s)	n (10^{18}cm^{-3})
A	0.20	0.8	no data	720	10
B	0.20	0.7	no data	580	9
C	0.25	2.5	0.0037	1200	1.4
D	0.25	2.55	0.0013	970	5
E	0.33	2.5	0.0021	1200	2.5
F	0.33	1	no data	350	11

The stoichiometric composition of samples D and F was checked by Energy Dispersive X-ray Analysis (EDX). This technique allows to determine the elemental composition of a specimen owing to the fingerprint response of the constituent atoms during the X-ray induced transitions in the inner atomic shells [96–98]. Two random spots were chosen on each sample and their elemental composition analyzed with Tescan Mira FEG SEM. A sample image of one spot is shown in fig. 4.9. EDX provided a detailed information about the concentration of each constituent of the samples. In order to calculate the Sn content x, its overall rela-

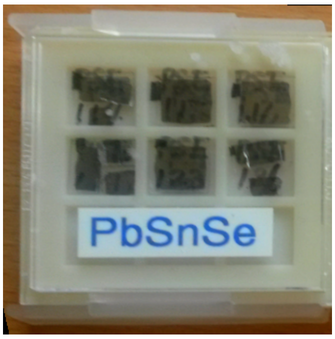

Figure 4.7: Photography of a few manufactured PbSnSe samples in a containment box.

tive stoichiometric part had to be normalized to the combined amount of Pb+Sn. Both samples show a slight deviation form the nominal composition in the order of a few percent (table 4.2).

Table 4.2: Raw relative elemental composition of samples D and F obtained using XRD analysis

Sample	Pb (%)	Sn (%)	Se (%)	x_{Sn}(%)	overall x_{Sn}(%)	$x_{nominal}$(%)
D	41.0	11.2	47.9	21.4±2	21.9	25
	40.8	11.8	47.4	22.4±2		
F	34.1	17.5	48.4	33.9±2	33.7	33
	34.3	17.3	48.4	33.5±2		

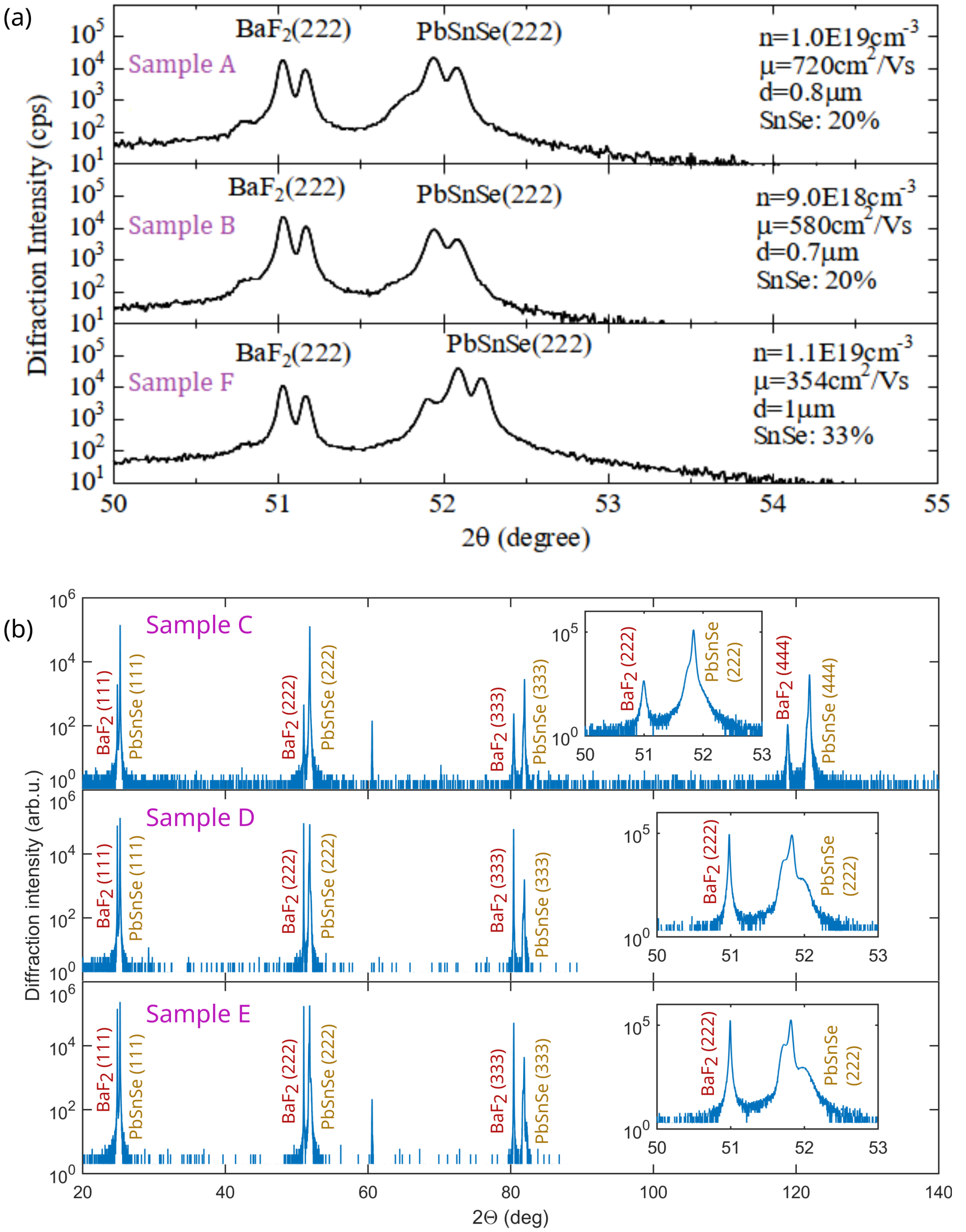

Figure 4.8: X-ray 2-Θ diffraction analysis of our PbSnSe samples. It confirms both the substrate and PbSnSe layers to be grown in (111) orientation. Almost all patterns exhibit several peaks instead of one, which might be due to presence of interference from the interface layers. Also, a different phase might have formed at the interface between $BaF_2(111)$ substrate and PbSnSe film. Samples A, B and F (a) were analyzed by Akihiro Ishida from Shizuoka university in Japan, samples C, D and E (b) by Petr Cejpek from he Department of Condensed Matter Physics, Charles University.

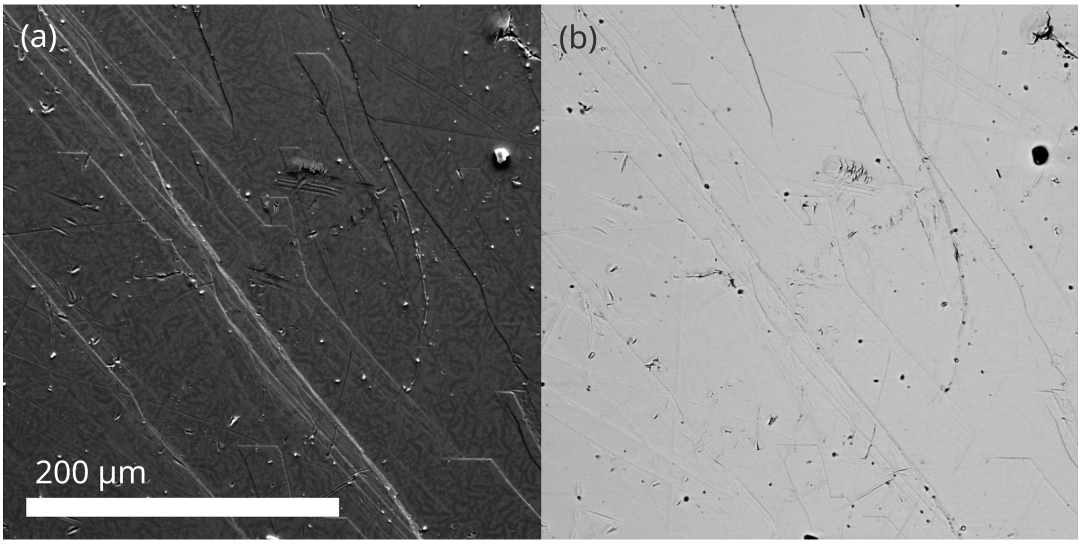

Figure 4.9: SEM picture acquired when performing EDX analysis of one spot of sample D. Secondary electrons originating from surface regions (a), backscattered electrons from deeper regions of the sample (b) [95].

4.3.5 Optical constants characterisation

To characterize the optical properties of the investigated samples, their response was probed using the spectroscopic ellipsometry at room temperature in the photon range between 0.7 to 6.4 eV. Spectral dependency of the complete Mueller matrix of samples C, D, F was evaluated at several angles of incidence ranging from 55 deg to 75 deg with 5 degree step. This allowed to obtain a confident evaluation of the complex dielectric function $\epsilon = \epsilon_1 + i\epsilon_2$ that was parametrized by a sum of several K-K consistent Lorentz oscillators. To obtain the best fit, 5 oscillators were considered, resulting in excellent correspondence between the measured and modeled ellipsometric quantities (fig. 4.10). Each oscillator is defined by its amplitude A, broadening γ and central energy E_0:

$$\epsilon_{Lor}(\hbar\omega) = \frac{A}{E_0^2 - (\hbar\omega)^2 - i\hbar\omega\gamma}, \tag{4.75}$$

and the explicit parameters for each oscillator are laid out in table 4.3. The additional term centered at 0 eV with zero broadening was used to account for the IR transitions unobservable directly. Because of the spectral limitations of the spectrometer, the absorption edge (the so-called E_0 transition) cannot registered directly.

The choice of oscillators that produced the best fit is not arbitrary but related to the well-known critical energies of the PbSe material family. They arise because of Van Hove singularities of the critical points (CPs) in the joint density of states. There are several spectral structures, historically mostly detected in reflectivity or second derivative of ϵ_2 measurements [34, 99–101]. Employing the band structure models, these were assigned to specific atomic transitions [18, 24, 30, 33, 35–37, 99, 102] (fig. 4.11):

- the very first $E_0 \approx 0.2 - 0.3$ eV transition corresponds to the **direct gap** of the material between L_6^+ in the valence and L_6^- in the conduction band [33].

This transition $L(5 \to 6)$ is related to M_0 symmetry of the CP [30, 102]. This peak is known to shift down in energy with decreasing temperature because of the closing gap [34]. Unfortunately, this particular energy was unattainable with our spectrometer, and is therefore not estimated;

- the **shoulder** at $E_1 \approx 1.6$ eV arises because of several transitions smeared together: M_1 symmetry $L(5 \to 7)$, M_0 symmetry $\sum(5 \to 6)$ and $L(4 \to 6)$ [30, 33, 102], formed by transitions between s-Pb valence states and p-Pb and a few of p-anion conduction states [18]. Notably, it has been interpreted as a transition between $L^+_{6\ upper}$ and $L^-_{6\ upper}$ [101]. Our model comprises 2 oscillators in this region, #1 and #2;
- the **main peak** $E_2 \approx 2.7{-}3$ eV is related to M_1 symmetry transition $\sum(5 \to 7)$ and M_2 symmetry transition $\Delta(5 \to 6)$ [30, 33, 101, 102], corresponding to interband transitions between p-anion (some form s-Pb) valence states and p-Pb and p-anion conduction states [18]. It is represented by oscillator #3;
- $E_3 \approx 3.8 - 4.2$ eV peak is related to M_2 symmetry transition $\Delta(4 \to 6)$ and M_1 symmetry transition $\sum(4 \to 7)$ [30, 33, 101, 102] between p-anion valence states and p-anion conduction states [18]. It is modeled by oscillator #4;
- the oscillator #5 just above 7 eV is most likely related to higher energy transitions around Γ, X [102].

Although the analysis of how the critical energies depend on the substitute material concentration x is mostly performed only for E_0, or the gap, our results allow to see the evolution of other critical energies $E_1 - E_5$, shown in fig. 4.12. A positive as well as negative peaking is present at $x = 0.25$ in all critical energies. Nonetheless, to understand their origin, explicit theoretical modeling of the band structure should be performed.

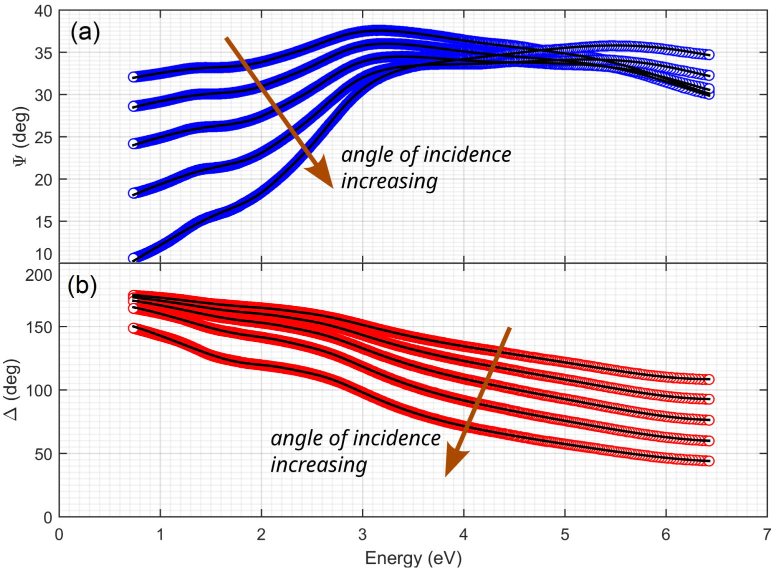

Figure 4.10: Raw experimental ellipsometric angles and the best-matching model for sample C.

Table 4.3: Parameters of Lorentz oscillators producing the best-matching dielectric function ϵ.

Sample	x	Parameters	MSE
C	0.25	$A_{pole} = 0.8055, \gamma_{pole} = 0, E_{pole} = 0;$ $A_1 = 14.0928, \gamma_1 = 1.7312, E_1 = 1.681;$ $A_2 = 7.1031, \gamma_2 = 0.8874, E_2 = 2.251;$ $A_3 = 12.1319, \gamma_3 = 0.9718, E_3 = 2.665;$ $A_4 = 1.8372, \gamma_4 = 3.6849, E_4 = 4.323;$ $A_5 = 1.4789, \gamma_5 = 2.3355, E_5 = 7.364;$	1.726
D	0.22 (nominal 0.25)	$A_{pole} = 0.7067, \gamma_{pole} = 0, E_{pole} = 0;$ $A_1 = 14.1130, \gamma_1 = 1.7367, E_1 = 1.693;$ $A_2 = 7.4672, \gamma_2 = 0.8915, E_2 = 2.273;$ $A_3 = 11.6116, \gamma_3 = 0.9487, E_3 = 2.671;$ $A_4 = 1.6557, \gamma_4 = 3.4775, E_4 = 4.379;$ $A_5 = 1.4150, \gamma_5 = 2.2201, E_5 = 7.308;$	1.927
E	0.33	$A_{pole} = 0.7800, \gamma_{pole} = 0, E_{pole} = 0;$ $A_1 = 13.7238, \gamma_1 = 1.6918, E_1 = 1.699;$ $A_2 = 7.7200, \gamma_2 = 0.8618, E_2 = 2.281;$ $A_3 = 13.4748, \gamma_3 = 0.9416, E_3 = 2.680;$ $A_4 = 1.9357, \gamma_4 = 3.5233, E_4 = 4.328;$ $A_5 = 1.4884, \gamma_5 = 2.4854, E_5 = 7.357;$	1.951

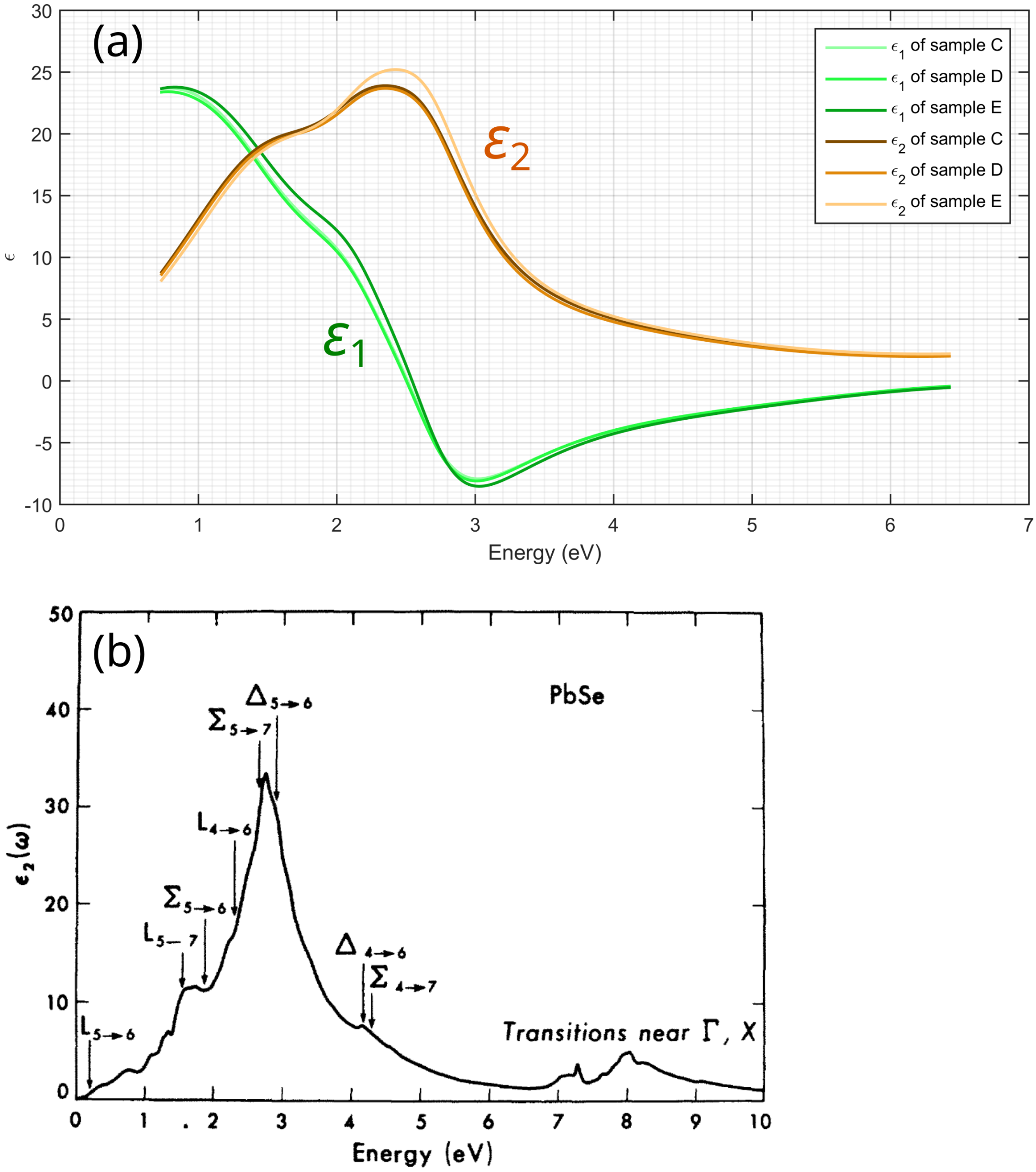

Figure 4.11: (a) Real and imaginary part of the dielectric function ϵ_1 and ϵ_2 of sample C, D and E providing the best match of ellipsometric data and model. (b) Critical points observable in ϵ_2 and the associated transitions in the energy band gap (from [102]).

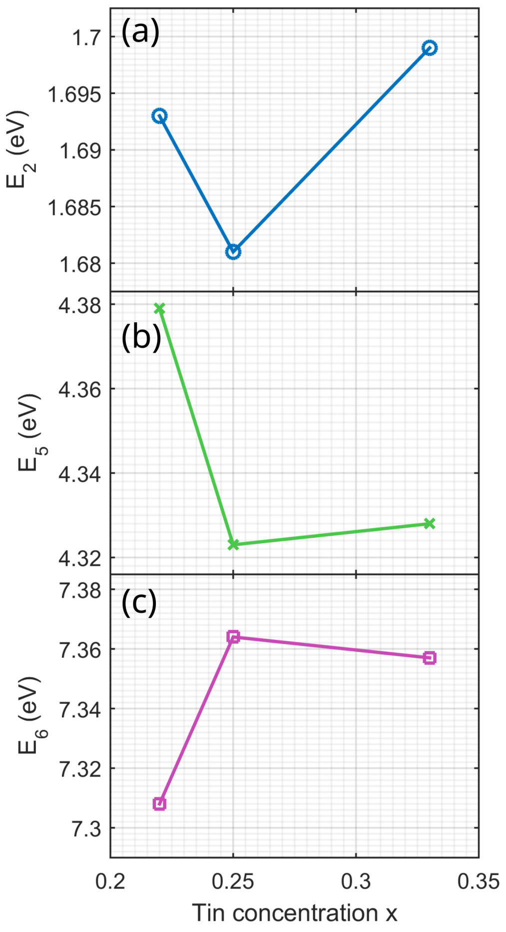

Figure 4.12: Oscillator energy (corresponding to the critical energies) dependency on tin concentration. E_2, E_3 and E_4 all exhibit the same trend and only E_2 is shown in (a) for brevity.

4.4 Landau level spectroscopy of PbSnSe samples

4.4.1 Measuring magneto-optical response of PbSnSe samples

The optical response of PbSnSe samples was probed in the middle infrared spectral region using magneto-transmission technique. These measurements were performed in the National High Magnetic Field Laboratory in CNRS Grenoble, France. The unpolarised radiation from a globar source was directed to the sample using a waveguide (fig. 4.13). The sample was placed in a dewar with liquid helium, where it was kept in the helium exchange gas below the λ point at 2 K. For fields below 13 T, a superconductive coil was used, while for fields above 13 T - a resistive coil. We used the Faraday configuration, in which the surface of the sample was perpendicular to the wave vector of incident light. Several mm^2 of the sample surface were illuminated. The FTIR spectrometer contained the globar source. The composite bolometer detector was placed just below the sample in the same dewar. The sample holder housed both the sample and the reference BaF$_2$ which could be rotated and each placed in the light path. They were both measured at each magnetic field, allowing us to remove the response of the substrate material from the signal as well as to correct for the bolometer response.

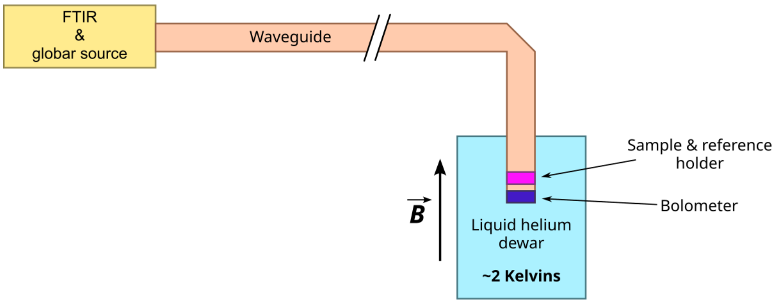

Figure 4.13: A general setup for the middle infrared magnetotransmission measurements.

The detected raw signal was normalized to the reference signal. It was acquired at $B = 0$ at 1) the beginning and 2) the end of measurements. The intermediate values were linearly interpolated in-between. This was required to account for the changing conditions (such as the changing helium level) over the entire measurement time which took up to 5 hours with the resistive coil measurements above 13 T. The resulting signal T_B/T_0 corresponds to a magnetic field-induced transmission and is thus called the **magneto-transmission**.

The resulting signal exhibits modulation starting from fields as low as 2 T (depending on the sample), indicating excellent quality of the samples. The raw data of all samples is presented in figs. 4.14 and 4.15. The stacked plots on the left side facilitate noticing the smallest changes in the signal. The 2D false color maps on the right side help to easily notice the overall grouping of peaks and valleys. These are related to magnetic field induced excitations. they follow a sub-linear dependence on B and can be straightforwardly interpreted as bulk transitions of interband Landau levels. Sample C exhibited the most pronounced modulation with the onset at merely 2 T. Up to 10 individual transitions can be distinguished in the magneto-optical response of this particular sample. In most other samples, any modulation did not become noticeable before reaching higher fields such as 5 T (sample D) or even 10 T (samples A or B).

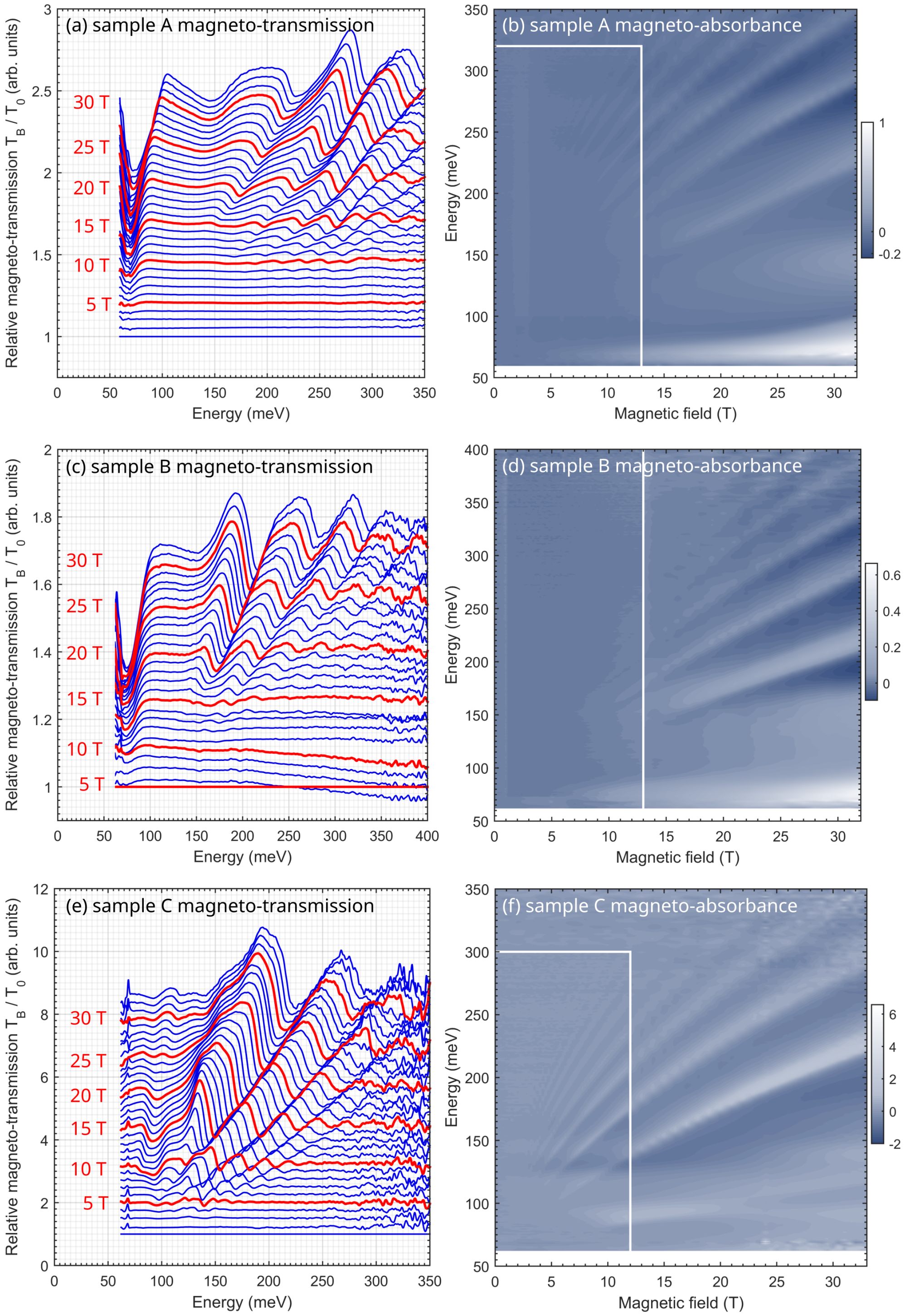

Figure 4.14: Magneto-transmission spectra of samples A-C acquired up to 33 T. Stacked spectra showing data every 1 T step (a, c, e). False color maps of magneto-absorbance $A_B = -\ln T_B/T_0$ (b, d, f). The white lines separate the areas of the data collected using a superconducting and resistive coil. The downwards bending of the low-field curves of sample B is a measurement artifact. Importantly, it does not affect the locations of the Landau level excitations energies, and thus does not influence further analysis. Sample C exhibited the most pronounced modulation starting at 2 T.

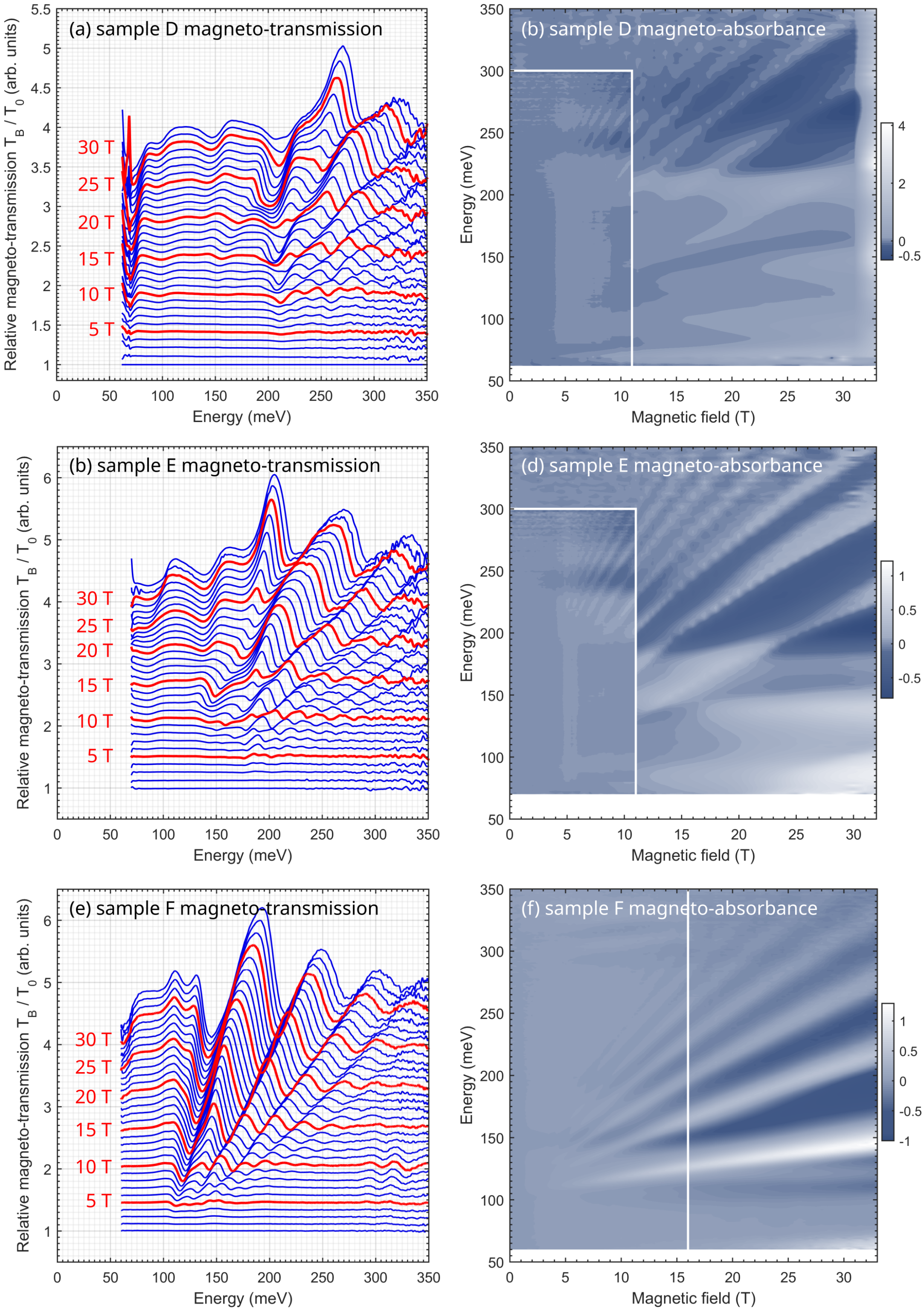

Figure 4.15: Magneto-transmission spectra of samples D-F acquired up to 33 T. Stacked spectra showing data every 1 T step (a, c, e). False color maps of magneto-absorbance $A_B = -\ln T_B/T_0$ (b, d, f). The white lines separate the areas of the data collected using a superconducting and resistive coil.

4.4.2 Magnetotransmission analysis

For further analysis, one needs to read out the precise excitation energies. The raw magnetotransmission spectra feature pronounced Fabry-Pérot interference patterns appearing in the transmission spectra of epilayers and related to their thicknesses (fig. 4.16). To get rid of those and to bring out the smallest changes in the spectra, one could calculate the differential spectra equivalent to a backward derivative $T_B/T_{B-\delta B}$. However, in reality, neither maxima nor minima in these signals correspond to real excitation energies. Each transition probability depends on the joint density of states which depends on the resonance energy E_0: $j_{DOS} \propto 1/\sqrt{E-E_0}$ (fig. 4.17, a). The j_{DOS} is additionally washed out by broadening (fig. 4.17, b). The absorption A_B depends on the optical conductivity σ_B, which in turn depends on j_{DOS}. The transmission, in the simplest form, can be related solely to absorption: $T_B \approx 1 - A_B$; it is accordingly dependent on the joint density of states: $T_B \propto 1 - j_{DOS}$. Thus, the transmission minima do not correspond to the exact excitation energies, neither the maxima of the differential signal (fig. 4.17, c). The real excitation energies lie in between. We better associated them with the inflection points in regions with negative slope. To locate them, we looked for peaks in the following modified spectra:

$$T_{\text{inflection}} = -\frac{\mathrm{d}\left(T_B/T_{B-\delta B}\right)}{\mathrm{d}E}, \tag{4.76}$$

where we first applied a gentle Savitzky-Golay filter on raw signals to minimize noise and later occurrence of false peaks. An example experimental inflection point array is shown in fig. 4.18. We then manually picked the energy- and magnetic field-dependent peak positions and discarded those not following any pattern (remaining noise and artifacts). The remaining peaks were associated with the excitation energies of interband Landau transitions. All points following the (presumably) same field-dependent curve were grouped. This way, we acquired a set of independent vectors holding the resonant energies of separate transitions. The exact Landau levels from which these transitions originate are so far unknown. With an appropriate model, these could be assigned to particular indices and material properties can be recovered.

Therefore, a typical magneto-transmission data processing workflow is as follows:

- recalculate raw experiment data to inflection point map;
- associate peaks in this map with real transition energies;
- group points belonging to the same yet unknown transition bands;
- use an appropriate physical model to determine the exact Landau level indices and sample parameters.

When the electron motion along the applied magnetic field is neglected ($k_z = 0$), the topological Hamiltonian provides the following LL spectra:

$$E_{N,\alpha,\beta} = \alpha\frac{M}{l_b^2} + \beta\sqrt{\left(\Delta + 2\frac{M}{l_b^2}N\right)^2 + 2\frac{v_F^2\hbar^2}{l_b^2}N}, \tag{4.77}$$

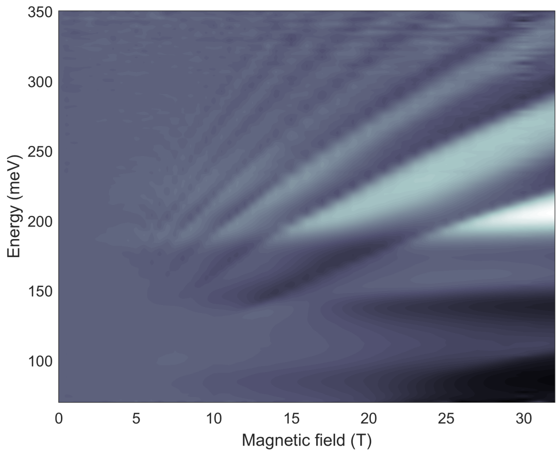

Figure 4.16: Fabry-Pérot interference observed in raw magnetotransmission spectra T_B/T_0, especially below 100 meV, 150 meV and 200 meV. This map is plotted in grayscale for easier visual inspection.

and for the ground states, owing to their full spin-polarisation:

$$E_{conduction\uparrow} = \Delta + \frac{M}{l_b^2}, \tag{4.78}$$

$$E_{valence\downarrow} = -\Delta - \frac{M}{l_b^2}, \tag{4.79}$$

where the level index $N = 1, 2, 3, ..$, $\alpha = \pm 1$ corresponds to the spin up and down, and $\beta = 1$ corresponds to the conduction while $\beta = -1$ to the valence bands. Because of the spin-polarisation and selection rules, the dominant transitions are $N \to N-1$ for h and $N \to N+1$ for h^* Hamiltonians (table 4.4). To get the transition energies, we take the energy difference between the electron and hole bands. This removes the first 'ballast' term $\alpha M/l_b^2$. The remaining part under the square root is the same for both Hamiltonians, as well as electrons and holes, only the level indices N differ. If we denote this square root term by $r(N)$, then transition energies for h Hamiltonian are

$$\Delta E_N = E_{N,+1,+1} - E_{N,+1,-1} = r(N) + r(N+1), \tag{4.80}$$

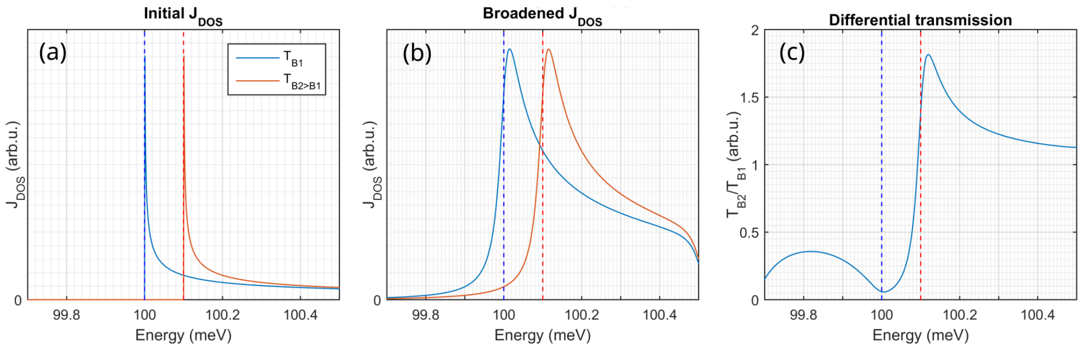

Figure 4.17: Idealized model of the joint density of states (a) and broadening (b) influence on the transmission signal (c). Because of these real-world effects, one cannot straightforwardly associate neither the minima nor maxima with the real excitation energies (dashed lines).

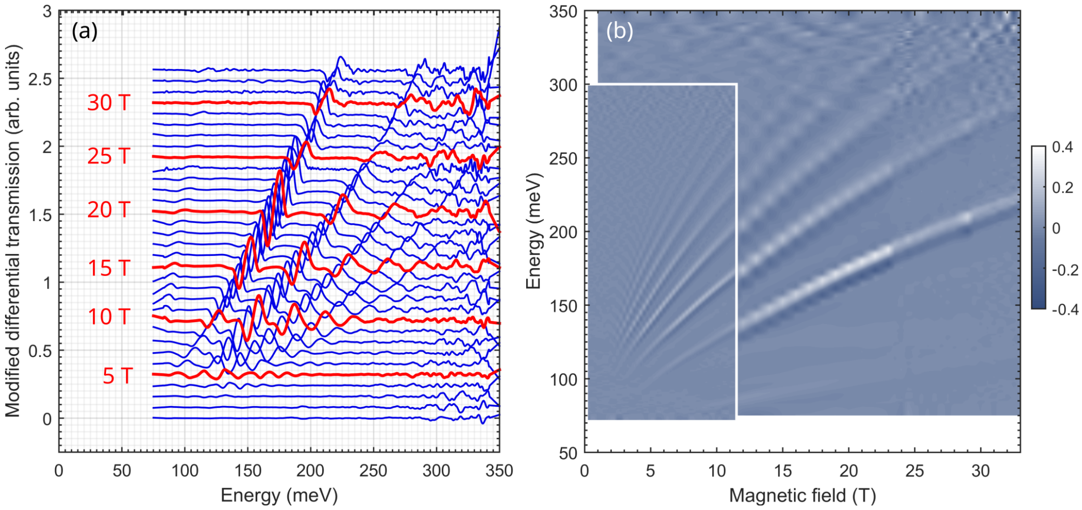

Figure 4.18: Inflection point spectra of sample C used to read out the exact Landau level excitation energies. Spectra stacked every 1 T (a) and 2D map (b). The white lines separate the areas of the data collected using a superconducting and resistive coil.

while for h^* Hamiltonian

$$\Delta E^*_{N'} = E_{N',-1,+1} - E_{N',-1,-1} = r(N') + r(N'-1). \tag{4.81}$$

But since $N' = N+1$, this transforms to

$$\Delta E^*_{N'} = r(N+1) + r(N) = \Delta E_N. \tag{4.82}$$

The transitions for both Hamiltonians are thus symmetrical, and **their energies are the same** for $0 \leftrightarrow 1$, $1 \leftrightarrow 2$, $2 \leftrightarrow 3$, ... transitions:

$$\hbar\omega_N = \sqrt{\left(\Delta + 2\frac{M}{l_b^2}N\right)^2 + 2\frac{v_F^2\hbar^2}{l_b^2}N} + \sqrt{\left(\Delta + 2\frac{M}{l_b^2}(N+1)\right)^2 + 2\frac{v_F^2\hbar^2}{l_b^2}(N+1)}, \tag{4.83}$$

where $N = 0, 1, 2, \ldots$. This greatly simplifies Landau level analysis as a single formula can be applied to all grouped transition bands. There is no need to additionally distinguishing their origin.

Table 4.4: Dominant transitions allowed by the topological Hamiltonians.

h	h^*
$h \to e$	$h \to e$
$1 \to 0$	$0 \to 1$
$2 \to 1$	$1 \to 2$
$3 \to 2$	$2 \to 3$
$\ldots \to \ldots$	$\ldots \to \ldots$

Now, the grouped transition bands can be fit to formula 4.83, interacting Landau levels and material parameters Δ (or $E_g = 2\Delta$), v_F and M determined. We want to emphasize that no secondary, weaker transitions or line splittings could be identified in either sample spectra. Other research groups reported observing those and assigned them to electrons originating from the longitudinal and oblique valleys of the lead tin salts [40, 41, 103]. Both exhibit the same Δ (since the material is the same) but different v_F. Their values are recovered by fitting the two data sets independently to equation 4.83. On the other hand, no Fermi velocity anisotropy could be observed in our samples. This conclusion agrees with a relatively low anisotropy of the electronic bands at the L point in PbSe (that can be expressed in terms of the anisotropic effective masses [104, 105]), which further decreases upon incorporation of Sn [40]. This is in contrast to some other lead-salt compounds, such as PbSnTe, in which the anisotropy is profound [106, 107], thus giving rise to well-resolved splitting of interband inter-LL resonances due to oblique and longitudinal valleys.

Dealing with each curve separately underconstrains the fit. Even though the exact level indices are unknown, one can with certainty assume that the neighboring transition bands originate from Landau levels differing by one. This is especially easy for higher transition bands which are densely packed close to each other. Therefore, handling a group of neighboring transition bands stabilizes the fit. Various N combinations are put to formula 4.83 and parameters Δ, v_F, M are varied. The N combination achieving the best fit to the transition curves (the lowest RMSE, or Root Mean Squared Error) is chosen.

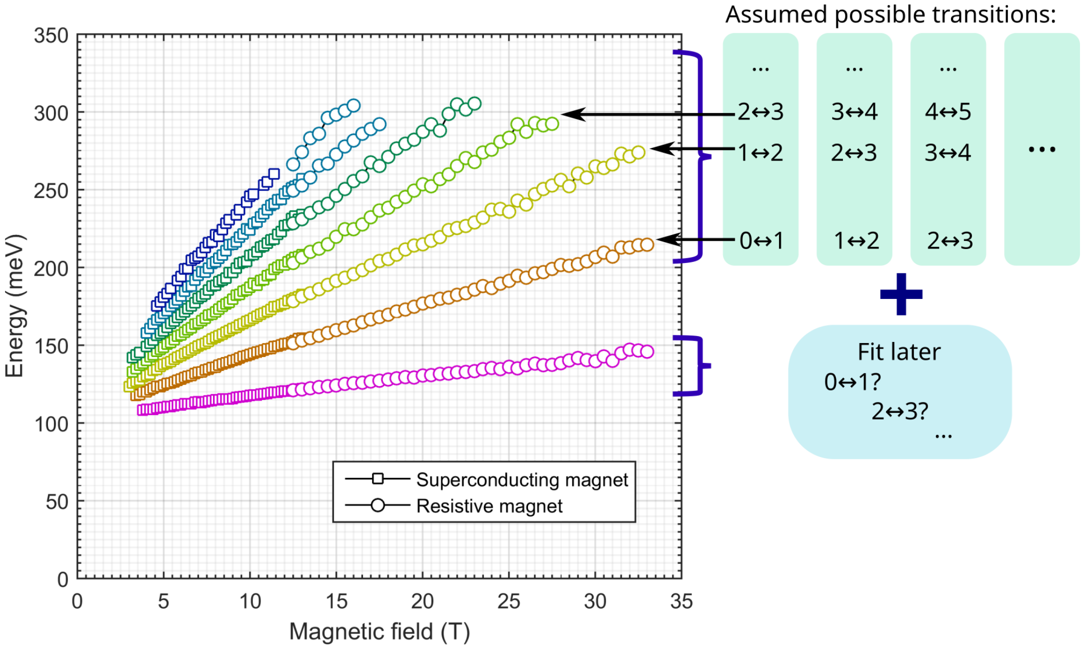

Figure 4.19: Assumed interband Landau transition level combinations of grouped sample F excitation points.

Including the ground transition might be ambiguous as both the surface states and cyclotron resonances typically emerge at similar low energies. They might have been ascribed to interband transition bands in previous steps. In such cases, it proved appropriate to first fit all higher transitions and acquire a set of material parameters; then include the potential ground transition and check if it does not drastically change neither these parameters nor the quality of fit. A sketch of grouped inflection points of sample F is shown in fig 4.19).

Very good agreement was reached between this simple theory and experimen-

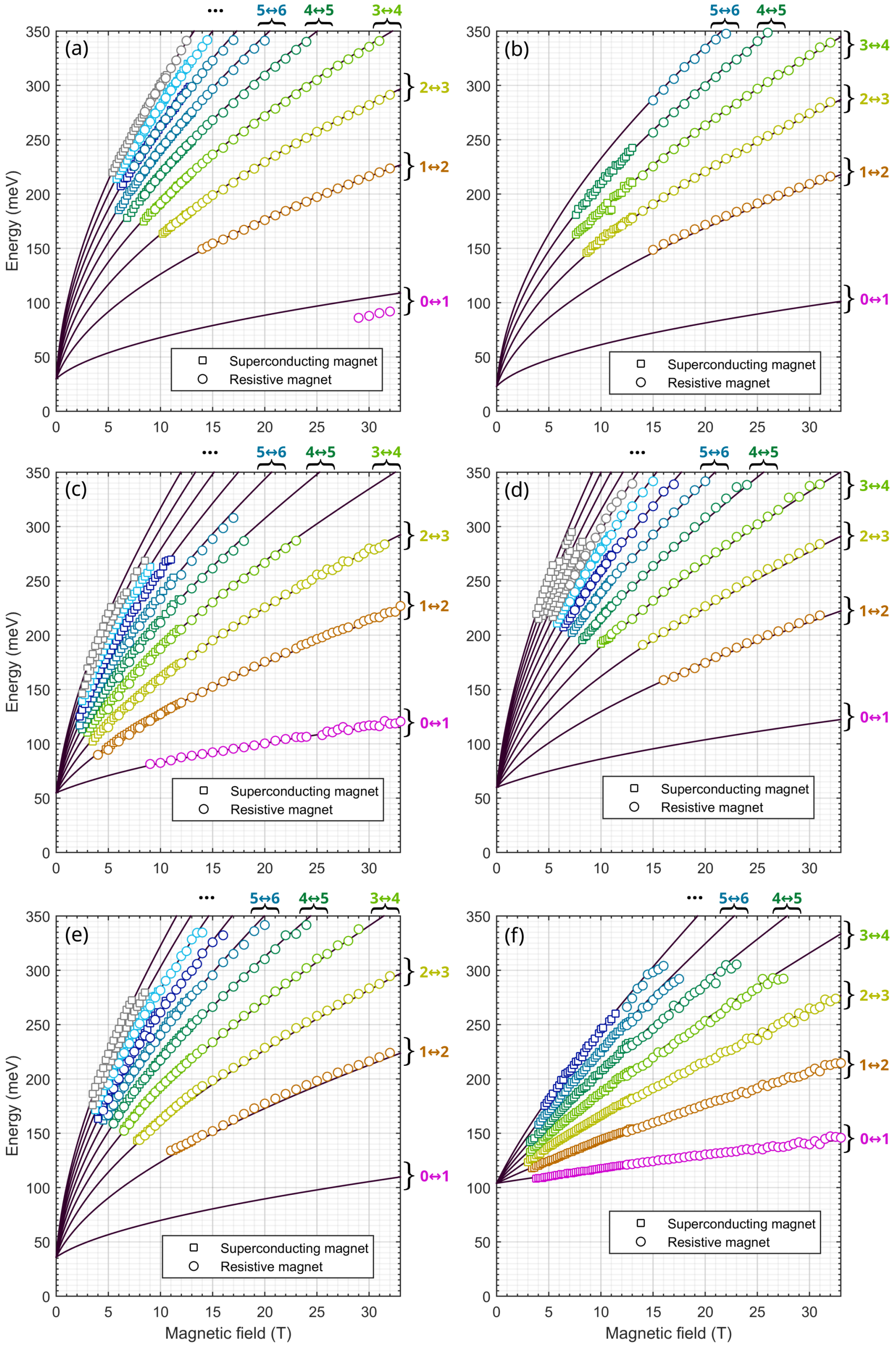

Figure 4.20: Grouped fan diagrams containing experimentally detected interband Landau level excitations (symbols) and best-fit dispersion curves (solid lines) with origin level indices of all samples A to F. For samples A, C and F, both the lowest and highest interband transitions were observed experimentally. For others, the ground transition could only be deduced from the best-fit parameters Δ, v_F and M using eq. 4.83. The fit of sample A ground transition is imperfect due to a very low number of points, which did not provide enough weight for this particular transition. The color coding was chosen only to facilitate the identification of the corresponding transitions and is consistent across all subfigures.

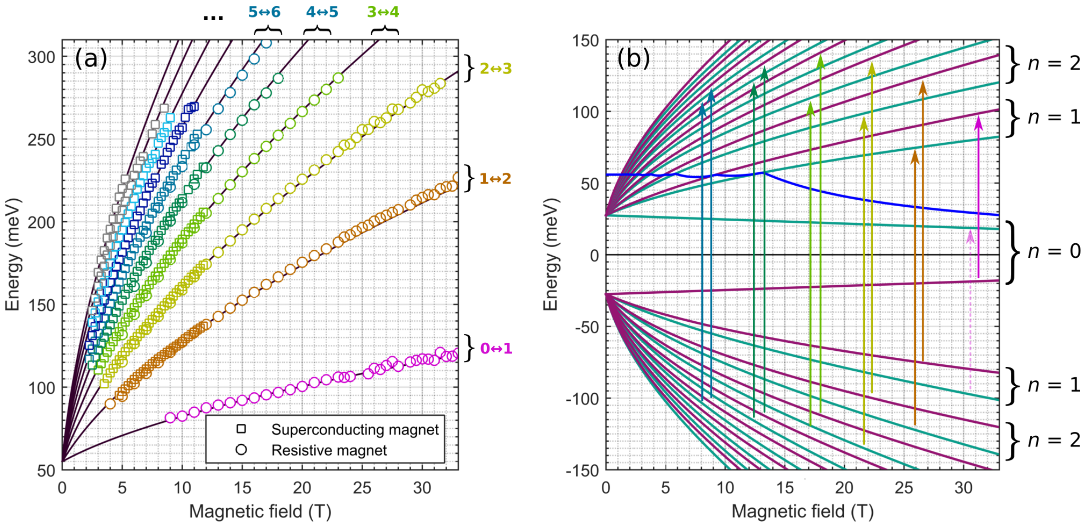

Figure 4.21: Fan diagram of inter-LL transition bands for sample C (a). Some data points were obtained using the superconductive (squares), others - resistive (circles) coils. Solid lines correspond to the best-matching theoretical lines with these parameters: $2\Delta = 55$ meV, $v_F = 4.4 \times 10^5$ m/s and $M = -20$eVÅ. This subfigure was copied from fig. 4.20 (c). Interacting Landau levels were determined and their spectra plotted in (b) for $k_z = 0$. Cyan and violet bands correspond to $\alpha = +1$ and $\alpha = -1$ LL series. Blue line marks the field-dependent Fermi energy assuming that the number of electrons is independent of field. The vertical arrows indicate the interband inter-LL excitations active in dipole-dipole approximation. The dashed line marks the transition forbidden due to band filling in turn enforced by E_F dependency on field. The color coding was chosen only to facilitate the identification of the corresponding transitions.

tal data, as illustrated in fig. 4.20 for all samples. For samples A, C and F, both the lowest and highest interband transitions were observed experimentally. For others, the ground transition could only be deduced from the best-fit parameters Δ, v_F and M using eq. 4.83. The fit of sample A ground transition is imperfect due to a very low number of points, which did not provide enough weight for this particular transition. Figure 4.21 additionally shows a detailed Landau energy band diagram for sample C. It explains the origin of each transition and how they are affected by another fundamental material parameter, the Fermi energy. The same analysis was carried out for all samples but is omitted here.

An excellent match with the experimental data corroborated the validity of our model. Both the positions and field dependency was reproduced well using only three parameters Δ, v_F and M that are summarized in table 4.5 and figure 4.22. The gap, or 2Δ, increases roughly linearly or weakly parabolically with tin content. The same behavior is observed for the absolute value of the parameter $|M|$. This parameter was fit freely without constraints, and its negative value indicates the topological regime of the material at measured temperatures. The difference in the extracted band gap for samples with presumably the same tin concentration points towards a variation of x as compared to the declared nominal values. This is in line with the EDX results mentioned before. The deduced Fermi velocity parameters show a weak tendency to decrease with x. Such behavior is perfectly in line with previous studies [103, 105, 108, 109].

Table 4.5: Fitted parameters of the bulk

Sample	Sn content	2Δ (meV)	v_F (m/s)	M (eVÅ^2)
A	0.20	34 ± 6	$(4.5 \pm 0.1) \times 10^5$	-12 ± 5
B	0.20	42 ± 8	$(4.3 \pm 0.1) \times 10^5$	-15 ± 1
C	0.25	55 ± 2	$(4.4 \pm 0.1) \times 10^5$	-20 ± 2
D	0.25	60 ± 10	$(4.4 \pm 0.1) \times 10^5$	-19 ± 5
E	0.33	42 ± 7	$(4.5 \pm 0.1) \times 10^5$	-19 ± 4
F	0.33	104 ± 5	$(4.2 \pm 0.1) \times 10^5$	-24 ± 1

The characteristic shape of the dispersion bands can be described by a dimensionless parameter η. It compares the influence of the relativistic part in the Hamiltonian:

$$\eta = \frac{4|M|\Delta}{\hbar v_F^2}. \tag{4.84}$$

For $\eta = 1$, the bands would be strictly parabolic, that is $E_\pm(\vec{k}) = \pm(\Delta + |M|k^2)$. In such case, the entire LL spectrum as well as the magneto-optical response would scale linearly with B. As an example, this occurs at the Γ point of the well known Bi_2Se_3 topological insulator. For all our investigated samples, we obtained $\eta < 1$. This implies subparabolic profiles of bands, and consistently with our experiments, magneto-optical excitations following a sublinear dependence in B. An extrapolation of bandstructure parameters as a function of the tin content (fig. 4.22) suggests that the condition $\eta = 1$ might be achieved at concentrations between $x = (0.35, 0.45)$ (fig. 4.23).

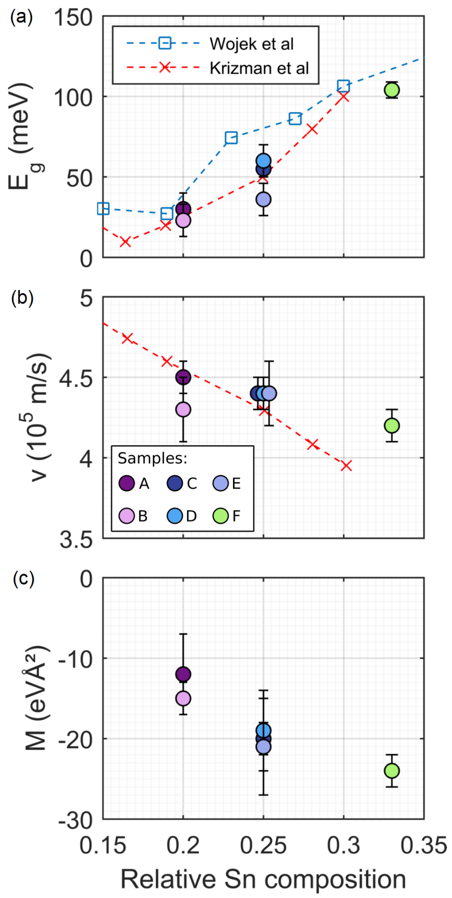

Figure 4.22: Band-structure parameters extracted from the magneto-optical data as a function of the nominal tin concentration: (a) energy band gap $E_g = 2\Delta$, (b) velocity parameter v_F, and (c) inversion parameter M. The symbols connected by dashed lines indicate the band gap and velocity parameter values extracted from [40, 109].

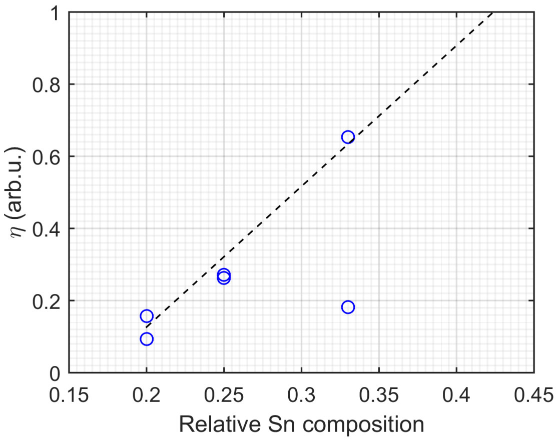

Figure 4.23: Measured values of η parameter describing the shape of the dispersion bands and its extrapolation to $\eta = 1$ condition.

4.5 Carrier density calculations

The analysis and subsequent simulations of the observed LL spectra involves the precise knowledge of the carrier concentration in the samples, and how it behaves under magnetic field.

4.5.1 Carrier concentration at B=0

Let's start with the simpler case of absent magnetic field. All electrons fill up the k-space from the bottom to the highest allowed level, which, at zero temperature, is the Fermi level. The total number of electrons in 3D space, with spin included, is then

$$n = \frac{2}{(2\pi)^3} \int_0^{k_F} \mathrm{d}^3 k. \tag{4.85}$$

Since in the absence of magnetic field, all directions are equivalent, we can assume the Fermi surface to be spherical. The volume of that sphere is

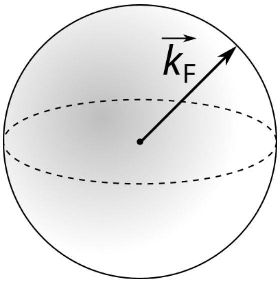

Figure 4.24: Fermi sphere in the k-space marking the highest level up to which the electrons are filled.

$$V_k = \frac{4}{3}\pi k^3, \tag{4.86}$$

and the volume element is

$$dV_k = 4\pi k^2 \mathrm{d}k. \tag{4.87}$$

We can then express the carrier density in terms of the Fermi radius k_F:

$$n = \frac{1}{4\pi^3} \int_0^{k_F} 4\pi k^2 \mathrm{d}k = \frac{1}{\pi^2} \int_0^{k_F} k^2 \mathrm{d}k = \frac{1}{\pi^2} \frac{k_F^3}{3} N, \tag{4.88}$$

where N is added phenomenologically to reflect the number of equivalent valleys. **This is the most general formula** where various dispersion models only come in via the Fermi radius k_F.

4.5.1.1 Parabolic dispersion

For parabolic dispersion, the Fermi level energy is described by the well-known textbook formula

$$E_F = \frac{\hbar^2 k^2}{2m}, \tag{4.89}$$

and inverting it yields

$$k = \sqrt{\frac{2E_F m}{\hbar^2}}. \tag{4.90}$$

Substituting it into equation 4.88, we get

$$n = \frac{N}{3\pi^2\hbar^3}(2mE_F)^{\frac{3}{2}}. \tag{4.91}$$

Now, if the concentration of carriers is known, we can invert the above equation to extract the Fermi energy dependency:

$$E_F = \frac{1}{2m}\left(\frac{3\pi^2\hbar^3 n}{N}\right)^{\frac{2}{3}}. \tag{4.92}$$

4.5.1.2 Relativistic dispersion

In such systems, there is an additional relativistic dispersion term:

$$E = \sqrt{\left(\frac{E_g}{2}\right)^2 + \hbar^2 k^2 v_F^2}. \tag{4.93}$$

For small k, this additional term is negligible and the dispersion is similar to parabolic. The main difference arises at high values of k, where this term dominates and turns the dispersion linear:

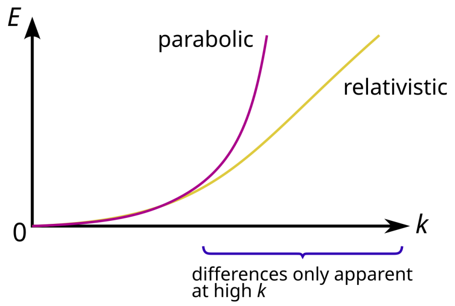

Figure 4.25: Differences between classical (parabolic) and relativistic solid state matter energy dispersion models.

$$E(k \gg 0) = \hbar k v_F. \tag{4.94}$$

Returning to the full model, we can extract k by squaring the full equation:

$$k_F = \frac{\sqrt{E_F^2 - \Delta^2}}{\hbar v_F}. \tag{4.95}$$

Inserting it back to eq. 4.88, the carrier concentration is then

$$n = \frac{N}{3\pi^2}\frac{(E_F^2 - \Delta^2)^{\frac{3}{2}}}{\hbar^3 v_F^3}. \tag{4.96}$$

If this quantity is known, then we can deduce the dependency of the Fermi energy:

$$E_F = \sqrt{\left(\frac{3\pi^2\hbar^3 v_F^3 n}{N}\right)^{\frac{2}{3}} + \Delta^2}. \tag{4.97}$$

4.5.1.3 Relativistic dispersion with weak M parameter

Including the M term, the full dispersion in the topological regime is

$$E = \sqrt{(\Delta + Mk_F^2)^2 + \hbar^2 v_F^2 k_F^2}. \tag{4.98}$$

This is a quadratic equation in terms of k^2:

$$\underbrace{\left(M^2\right)}_{a} k^4 + \underbrace{\left(2\Delta M + \hbar^2 v_F^2\right)}_{b} k^2 + \underbrace{\left(\Delta^2 - E_F^2\right)}_{c} = 0, \tag{4.99}$$

having a textbook solution

$$k_F^2 = \frac{-b + \sqrt{b^2 - 4ac}}{2a}. \tag{4.100}$$

which can be further numerically processed by taking its root to get k_F. It can then be put back to the main dispersion formula 4.88 to get the carrier concentration. This process can be repeated with several initial guess values of E_F using the simple arithmetic formulas above until a target n is reached. This way, one can numerically estimate E_F.

Table 4.6: Initial carrier concentrations and E_F values at $B = 0$.

Sample	n_0 (10^{18} cm^{-3})	E_F (meV)
A	9	120
B	10	119
C	14	66
D	5	146
E	2.5	79
F	11	120

Because of convention, M is negative in the topological regime. This puts a limitation on the analytical formula. It can be solved as long as M is small so that b term remains positive. This also explains the limitation to the + solution only in the quadratic solution formula 4.100. It is because $-b$ alone is negative while k_F^2 must be positive.

4.5.2 Carrier concentration at $B \neq 0$

At non-zero magnetic field, the most general rule to count the total number of carriers would be to sum over all possible states, taking the orbital filling factors into account:

$$n = \int g(E) f(E) \mathrm{d}E, \tag{4.101}$$

where $f(E)$ is the Fermi distribution function and $g(E)$ is the density of states. At absolute zero, the Fermi function becomes a step function (fig. 4.26), changing the integration limits and simplifying the expression:

$$n \approx \int_0^{\mu} g(E) \mathrm{d}E. \tag{4.102}$$

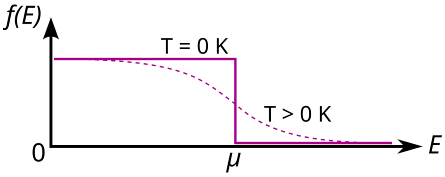

Figure 4.26: Fermi distribution at ideal zero and finite temperatures.

The temperature during the experiments was kept barely above zero, so it is a reasonable approximation to adopt such a step-like Fermi distribution for subsequent analysis. In the context of Landau levels, it can be simplified further. In our model, only $k_z = 0$ states are active. At some given magnetic field B, there is a set of possible $k_z = 0$ values, each dispersing according to whatever the dispersion model is valid. Electrons fill all those possible states up to the limiting Fermi level (fig. 4.27). Therefore, each Landau level is taking up some Δk_z interval in the k_z space. We can then relate the carrier concentration to this filling factor:

$$n \sim \sum \Delta k_z \underbrace{\frac{eB}{h}}_{\text{degeneracy}}, \tag{4.103}$$

the full expression being

$$n = N \sum_{\uparrow,\downarrow} \Delta k_z \frac{eB}{\hbar} \frac{1}{(2\pi)^2} = N \frac{eB}{\hbar} \frac{1}{(2\pi)^2} \sum_{\uparrow,\downarrow} \Delta k_z. \tag{4.104}$$

This is a universal formula and $\uparrow, \downarrow$ represents summing over spin up and down. And just like eq. 4.88, it is able to include any dispersion via Δk_z term(s). It will be used to determine the Fermi energy at varying magnetic fields for the same sample. Since the sample remains the same and the carriers cannot escape from it, we assume that their concentration does not change. What can be reasonably expected?

- Landau levels disperse with magnetic field while their degeneracy remains constant. Thus, the E_F will change to adapt to varying availability of energy levels;
- At the highest magnetic fields, all carriers tend to be pressed to the lowest Landau level. In order to accomodate them, E_F converges to this lowest level;
- Solutions with and without B should converge to each other at the lowest fields.

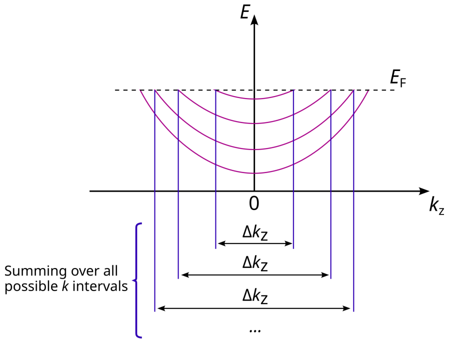

Figure 4.27: Set of dispersing Landau levels up to the limiting Fermi energy.

4.5.2.1 Parabolic dispersion

At $k_z = 0$, each level has certain (for the moment arbitrary) energy E_N. The dispersion is then

$$E_z = E_N + \frac{\hbar^2 k_z^2}{2m^*}, \tag{4.105}$$

and inversion is straightforward:

$$k_z = \pm\sqrt{\frac{2m^*}{\hbar}\left(E_z - E_N\right)}. \tag{4.106}$$

Because of a common prefactor and symmetry, $\Delta k_z = 2k_z$, and the full expression becomes

$$\sum_{\uparrow,\downarrow} \Delta k_z = \sqrt{\frac{8m^*}{\hbar}} \sum_{\uparrow,\downarrow} \sqrt{E_F - E_N}. \tag{4.107}$$

This expression suggests an efficient algorithm for calculating $\sum \Delta k_z$ numerically. For instance, one can first calculate energy differences $(E_F - E_N)$ for multiple levels and only continue with the positive terms.

It is a good sanity check to use the fitted parameters of the samples with this simplest model. We do not expect it to be valid inside the investigated material, but it has to provide reasonable results converging with those at $B = 0$. The introduced magnetic field would manifest by an additional splitting via the Zeeman effect for the two spin orientations:

$$E_{\uparrow,\downarrow}(B,N) = \frac{\hbar e B}{m^*}\left(N + \frac{1}{2}\right) \underbrace{\pm g \mu_B B}_{\text{Zeeman term}}, \tag{4.108}$$

where $gapprox2$ is the Landé g factor and $\mu_B = e\hbar/2m_e \approx 9.274 \cdot 10^{-24}\mathrm{JT}^{-1}$ is the Bohr magneton. We took sample C as a reference ($m^* \approx 0.05 m_e$), resulting in $E_F|_{B=0} = 36$ meV. In the dispersion model, we also included the polarisation of the ground levels. The result is a perfect match between all calculated E_F values, as well as the characteristic monotonously increasing E_F at high B (fig. 4.28), just as expected.

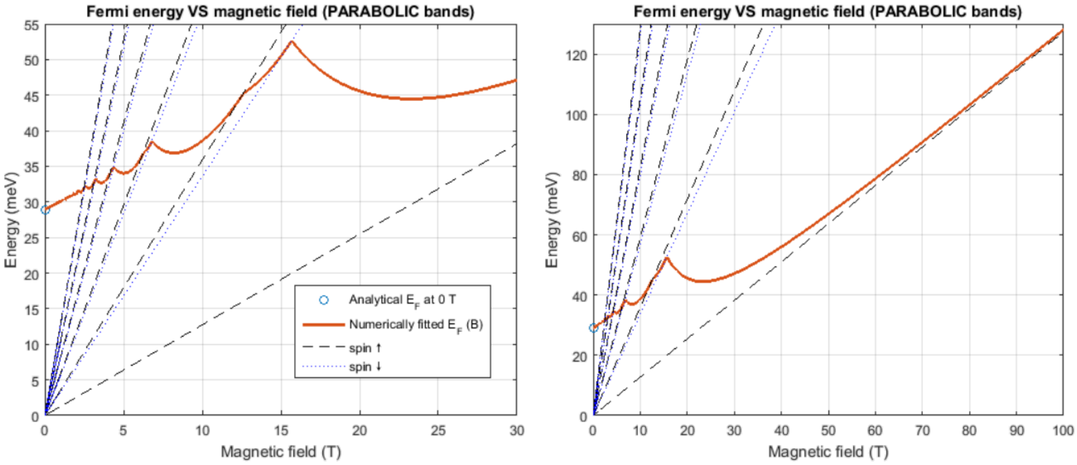

Figure 4.28: Parabolic Landau level dispersion model using sample C parameters. Left graph - zoomed in version, right graph - up to 100 T. There is an excellent agreement between the analytical and best fit E_F at the lowest fields. At high fields, E_F approaches the ground level as there is no other available level for the carriers. It becomes highly degenerate.

4.5.2.2 Relativistic dispersion

In this case, we follow the convention of the half band-gap, and will mark it Δ_N to reflect that at the moment, it can be an arbitrary bandgap of any Landau level:

$$E = \sqrt{\Delta_N^2 + \hbar^2 v_F^2 k_z^2}, \tag{4.109}$$

and inversion yields

$$\sum_{\uparrow,\downarrow} \Delta k_z = \frac{2}{\hbar v_F} \sum_{\uparrow,\downarrow} \sqrt{E_F^2 - \Delta_N^2}. \tag{4.110}$$

This formula once again suggests an efficient method for numerical calculations - first calculate an array of $(E_F^2 - \Delta_N^2)$ and then continue only with positive ones.

4.5.2.3 Relativistic dispersion in topological regime

The full formula with M term is too complicated to be tackled analytically:

$$E_{N,\alpha,\beta} = \alpha \frac{M}{l_b^2} + \beta \sqrt{\left(\Delta + M k_z^2 + 2\frac{M}{l_b^2} N\right)^2 + 2\frac{v_F^2 \hbar^2}{l_b^2} N + \hbar^2 v_F^2 k_z^2}, \tag{4.111}$$

with fully polarised ground levels

$$E_{N=0} = \pm \sqrt{\left(\Delta + \frac{M}{l_b^2} + M k_z^2\right) + \hbar^2 v_F^2 k_z^2}. \tag{4.112}$$

To get around with a numerical solution, one can define a grid fine enough for k_z and another grid of N going reasonably high. N must be no less than the highest Landau level available at a given magnetic field in order to account for all possible carriers. A trial E_F value is used and fed to the full formula. For each N, a k_z grid is used to calculate the energy. It is discarded beyond E_F. Summing up the obtained Δk_z segments from all available N, carrier concentration is calculated for this initial E_F. If it is too low or too high than the target, it is adjusted and the process repeats. One could say that we numerically fit the E_F to the value producing the best match to the target sample initial concentration n_0. To make the algorithm as simple as possible, we actually minimized the squared difference between the trial n and target n_0.

Let us now pay attention to the influence of M. In its absence, there is a symmetry between h and h^* Hamiltonians, and their energy levels are identical. The ground levels are equivalent to the nominal Δ of the material and are constant over B. In fig. 4.29, we are showing all these possible scenarios taking sample C parameters as a reference. Nonzero M values give rise to difference between the two Hamiltonians. It fundamentally changes the dispersion of the ground levels. For positive values of M, the ground levels of both Hamiltonians diverge from each other. This does not essentially change the expected behavior of E_F - it would simply asimptotically converge towards this particular ground level. For negative M, however, both bulk levels converge linearly. There exists a point where the lowest levels of h and h^* Hamiltonians cross at 0 meV (~95 T predicted for sample C, albeit currently inaccessible experimentally; see fig. 4.30), and then the only physically available Landau level for carriers is the ground level from the other h^* Hamiltonian.

This crossing brings about many unusual effects. For instance, it is responsible for the Quantum Spin Hall Effect in HgTe quantum wells [11], or negative longitudinal magnetoresistance in $Pb_{1-x}Sn_xSe$ [110]. In other cases, an **avoided crossing** is observed where the spectal lines split instead of becoming degenerate due to the breaking of bulk inversion symmetry, but also likely mediated by electron-electron interactions [111], or due to spin-orbital mixing [112]. Overall, this **(anti)crossing of the bulk zeroth-mode Landau levels is a characteristic feature for all topological (crystalline) insulators**. The field at which the crossing occurs, also called **the critical field** B_C, can be estimated from the crossing condition for the $k_z = 0$ ground states, $E_{cond\uparrow} = E_{val\downarrow}$:

$$B_C = -\frac{\hbar\Delta}{eM}. \tag{4.113}$$

The calculated critical fields for all our samples are summarized in table 4.7. It is apparent that they are all much above the magnetic fields achievable in our experiments. In this manner, the fascinating effects associated with the bulk band crossing could not be registered.

Table 4.7: Predicted B_C values for the bulk ground state Landau levels crossing.

Sample	B_C (T)
A	82.3
B	50.5
C	95.3
D	103.9
E	56.4
F	142.6

Comparing the most general analytical relativistic dispersion 4.109 and a full explicit topological dispersion 4.111, one might be tempted to check how well would 4.109 hold with our assumption that only $k_z = 0$ states are active in all

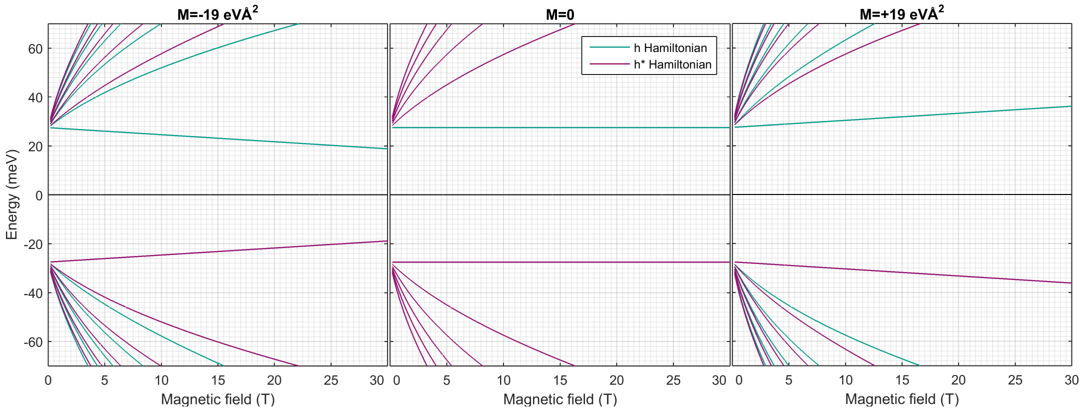

Figure 4.29: Influence of M parameter on the $k_z = 0$ Landau level spectra zoomed to experimentally achievable magnetic fields. With $M = 0$, both h and h^* Hamiltonians are identical, and ground levels do not disperse. Any other M value gives rise to the asymmetry. Although the higher levels change a little, it considerably alters the slope of the ground levels.

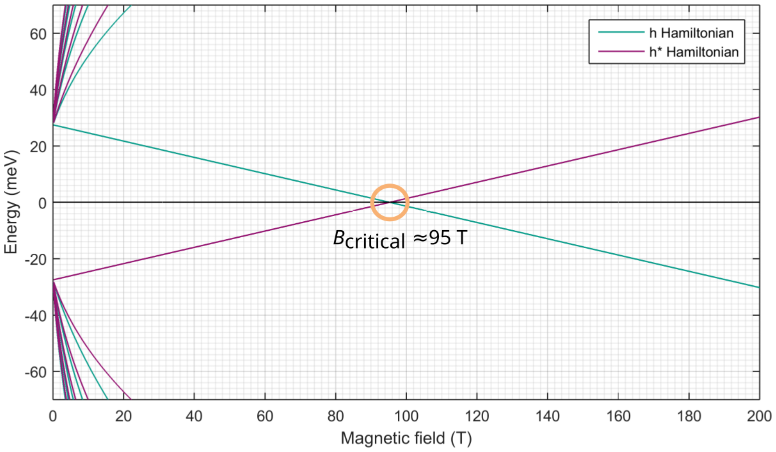

Figure 4.30: Ground **bulk** Landau levels $k_z = 0$ crossing for $M < 0$. This is a characteristic feature for all topological insulators. In this example, we took sample C parameters as a referece. The crossing is predicted to occur at a critical magnetic field of ~95 T.

these transitions. Also, it does not explicitly include M. On the other hand, we can include it via the expression of Δ_N, taking it from the topological Hamiltonian. The energy formulas read:

$$\Delta_N(k_z = 0) = \alpha\frac{M}{l_b^2} + \beta\sqrt{\left(\Delta + 2\frac{M}{l_b^2}N\right)^2 + 2\frac{v_F^2\hbar^2}{l_b^2}N}, \tag{4.114}$$

and for the ground states, owing to their full spin-polarisation:

$$E_{conduction\uparrow} = \Delta + \frac{M}{l_b^2}, \tag{4.115}$$

$$E_{valence\downarrow} = -\Delta - \frac{M}{l_b^2}, \tag{4.116}$$

where $\alpha = \pm 1$ corresponds to the spin up and down, and $\beta = 1$ corresponds to the conduction and $\beta = -1$ to the valence bands. Just a reminder, owing to the absence of the electron-hole symmetry and selection rules for both Hamiltonians, in $k_z = 0$ case, we can include the ground level polarisation by restricting the N grids for both Hamiltonians (table 4.8). For $k_z = 0$ case, there is no additional struggle to sum and fit over all k_z grid. This part of the calculations is thus removed. Accordingly, one can first numerically calculate the energies for a given field and a grid of N, then put these to the analytical expression 4.110, which is much easier and faster to fit. As formula 4.109 is basically formula 4.111 with $M = 0$, and parameter M is in the order of -20 meVÅ in our samples, the resulting E_F should not be too different. The results indeed show a small overall difference between the two calculations. The simplified relativistic model exhibits a correct anticrossing and converges towards the full correct model (fig. 4.31). The deviation from the full model is in the order of a few percent on average, as can be seen in fig. 4.32.

Table 4.8: Allowed Landau level N grids for h and h^* Hamiltonians for $k_z = 0$.

Hamiltonian	Allowed N grid
h	[0, 1, 2, ...]
h^*	[1, 2, ...]

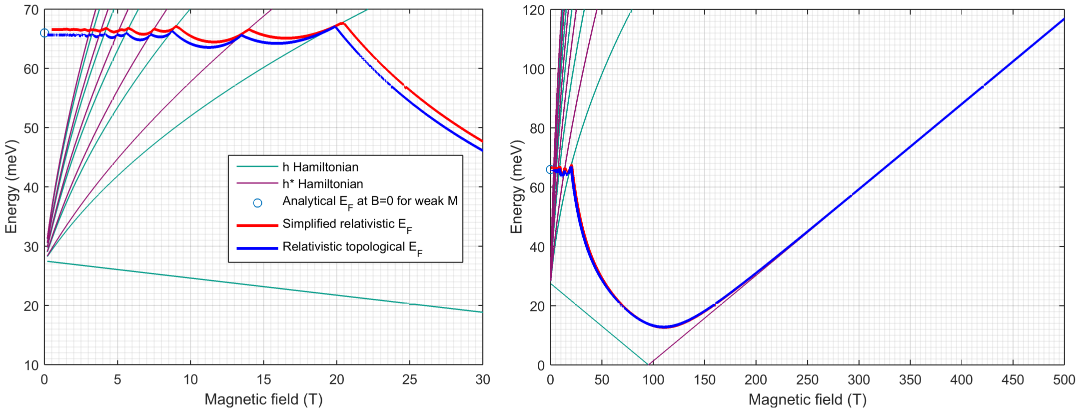

Figure 4.31: Best fit E_F values and their comparison to the full explicit topological and simplified relativistic models. Left side - zoomed in to experimentally accessible fields, right side - model up to 500 T. Although there is a slight deviation between the two E_F dispersion models at first, they converge at higher fields. Both models correctly account for the anticrossing at a critical magnetic field. At the highest fields, because of absence of any other available Landau levels, all carriers accumulate on the ground level, which asimptotically raises E_F.

The goal of calculating the magnetic field-dependent Fermi energy is to achieve the best match of our model with the experiment. To achieve that, we had to tune the electron densities. We have chosen to adjust it to the reference point, the appearance of the lowest bulk interband inter-LL excitation. To do that, we calculated an array of E_F starting from 100% nominal concentration going down every 5-10% (see fig. 4.33 for example). Those Fermi energies were then used in our model and magneto-optical repsonse spectra were calculated for each case.

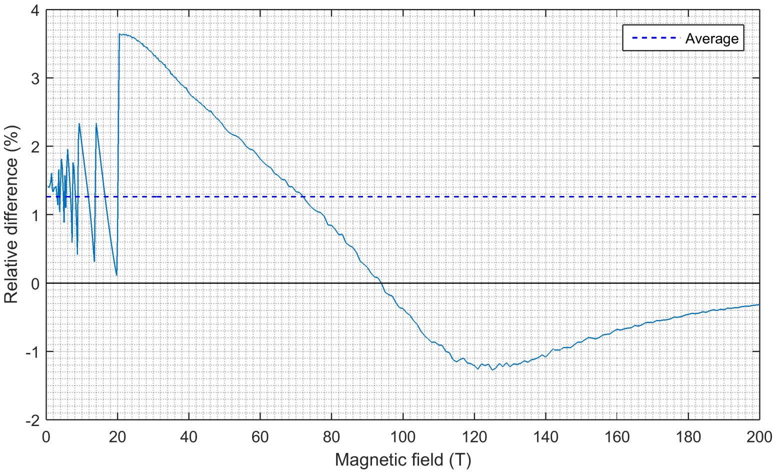

Figure 4.32: Relative difference between E_F from the full topological and simplified relativistic models. Although the deviation exhibits a few abrupt jumps up to almost 4% in experimentally achievable magnetic fields, it is around merely 1% on average, and eventually converges to 0.

The final n was chosen so that the lowest bulk transition appears like observed experimentally. A few sample inflection point maps obtained with different n are shown in figure 4.34. The resulting electron densities are in general smaller than nominal, measured by Hall conductivity at room temperature, by a factor of 2. We attribute this to sample aging (storage and handling). Only sample F was an exception and we had to consider n by an order of magnitude smaller than the initial n_0.

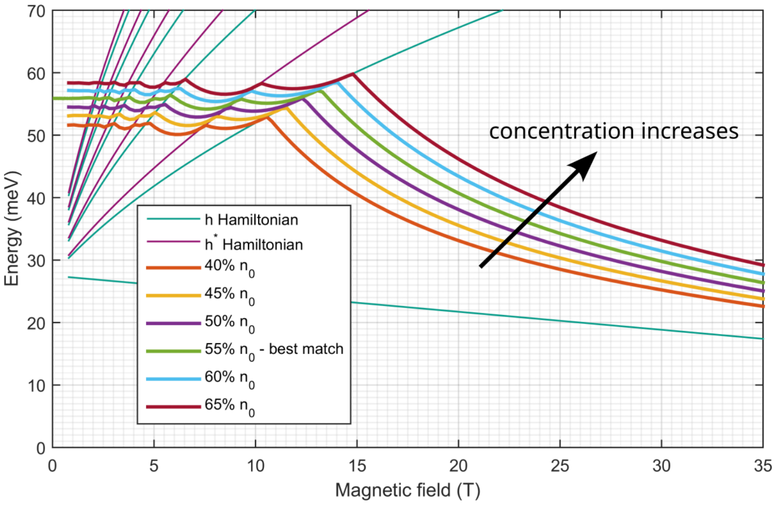

Figure 4.33: A few obtained Fermi energy dependencies on the magnetic field for sample C around the optimal value of 55%.

Table 4.9: Tuned carrier concentrations.

Sample	n_0 (10^{18} cm^{-3})	ratio n/n_0 (%)
A	10	35-40
B	9	30
C	1.4	55-60
D	5	75
E	2.5	100
F	11	2.5

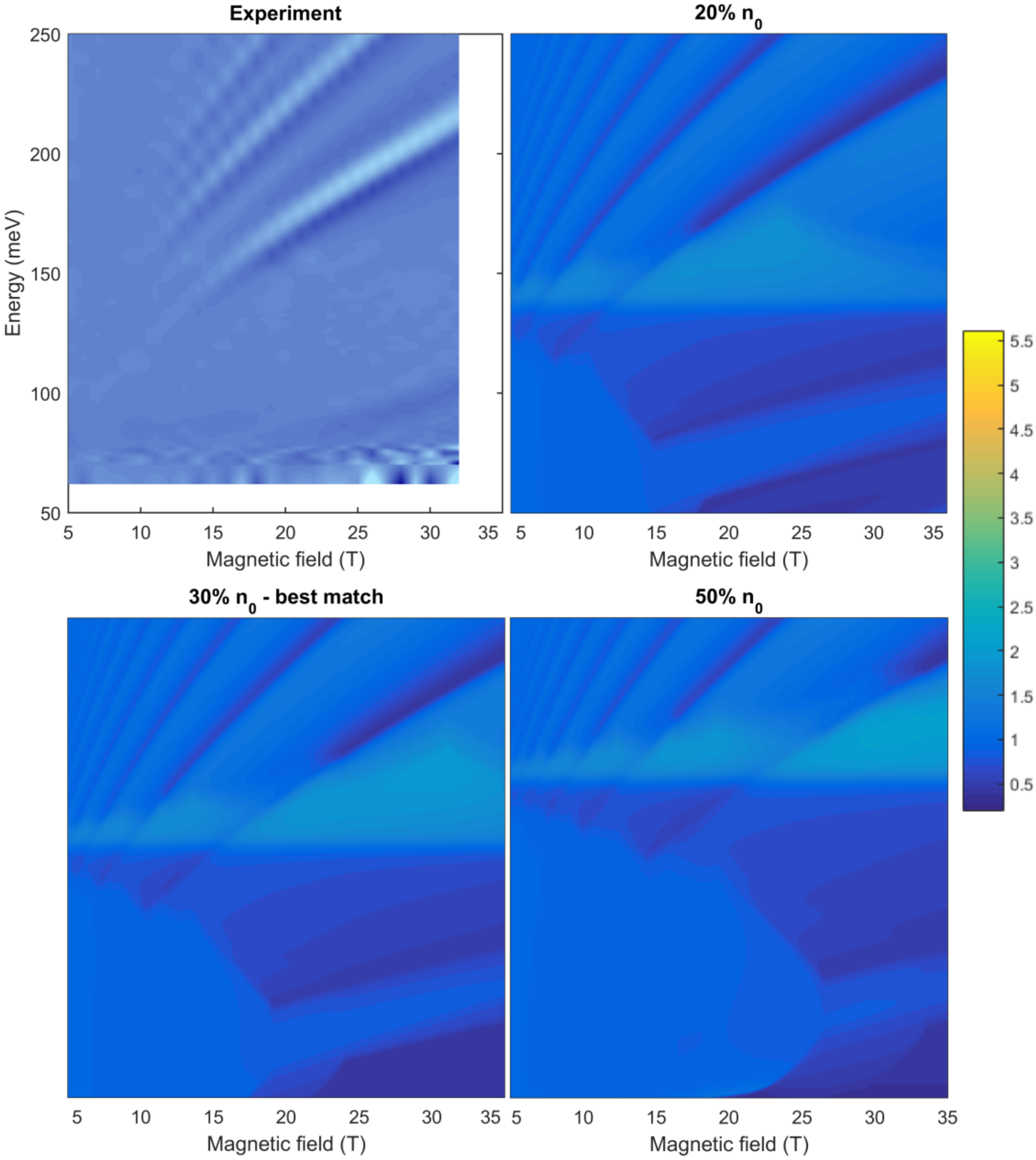

Figure 4.34: Several inflection point maps for sample B with Fermi energies calculated for several carrier concentrations. $n = 0.5 \cdot n_0$ produces the onset of the lowest interband transition below 15 T, which is too high; similarly, $n = 0.2 \cdot n_0$ produces it just a bit too low, at 7 T. $n = 0.3 \cdot n_0$ gives the best match at roughly 10 T. The colorbar is for amplitude estimation of the simulated colormaps only.

4.6 Theoretical modeling

4.6.1 Kubo-Greenwood formalism

Now that we have deduced the bulk parameters of the investigated PbSnSe samples in the topological regime (indicated by $M < 0$), it is in our interest to develop an effective model to theoretically replicate experiment data, and explore the influence of broadening, as well as check the validity of E_F calculations. This was done in the framework of the Kubo-Greenwood formalism. The adapted formula describes the interaction of light and LLs induced by an external magnetic field. It expresses the optical conductivity σ in terms of the left- and right-circularly polarised light ±:

$$\sigma^{\pm}_{\omega,B} = 2\frac{iG_0 N}{l_B^2 \omega} \sum_{n,m,k_z} \frac{(f_m - f_n)|\langle m|\, \hat{v}_{\pm}\, |n\rangle|^2}{E_n - E_m - \hbar\omega + i\gamma}, \tag{4.117}$$

where $G_0 = e^2/(2\pi\hbar)$ is the quantum of conduction, $N = 4$ is the valley degeneracy and γ is the broadening parameter. LL occupation is given by the Fermi distribution function f. Indices m, n run over all available initial and final LLs, including the states with nonzero k_z momenta. The velocity operator is given by

$$\hat{v}_{\pm} = \hat{v}_x \pm i\hat{v}_y, \tag{4.118}$$

its components in turn are defined by

$$\hbar\hat{v}_x = \frac{\partial \hat{H}}{\partial k_x}, \hbar\hat{v}_y = \frac{\partial \hat{H}}{\partial k_y}. \tag{4.119}$$

To calculate the transition energies $E_{n,m}$ and velocity operator matrix elements $\langle m|\, \hat{v}_{\pm}\, |n\rangle$ for all k_z contributions and keep all features of the full topological insulator model, we have essentially numerically diagonalized the full 4.52 Hamiltonian with $C = 0$.

The quality of simulation is influenced by the grid of k. We have chosen to limit its maximal value to 1.25 nm^{-1} and the grid step $\Delta k = 0.0025$ nm^{-1}. $\epsilon_\infty = 20$ was chosen based on reported values from literature [28, 34]. Its role is to account for the spectral tails of transitions outside of the measured spectral range and not computed explicitly. Based on the fitted band parameters, for the lowest fields, the number of transitions that had to be included in the simulation ranged roughly from 20 to 200, depending on the sample. Further optimisation is possible by adaptively adjusting the computed Landau levels. The higher the field, the fewer available levels.

For a given magnetic field B, an independent 4x4 Hamiltonian was computed for each Landau level N and k_z element. To exploit the computational parallelism, those Hamiltonians were put as diagonal sub-elements of a single matrix of zeros. Diagonalizing it returned both the eigenvectors (for calculating the matrix elements $\langle m|\, \hat{v}_{\pm}\, |n\rangle$) and the eigenvalues (transition energies). This allowed efficient computation of all possible transition permutations, including forbidden ones. To discard those, level occupancies (determined by the field-dependent E_F) were applied. Furthermore, the velocity operator matrices contain a lot of vanishing elements, which makes the resulting matrices very sparse, only containing a few hundreds of elements. Besides, these terms are frequency-independent. This

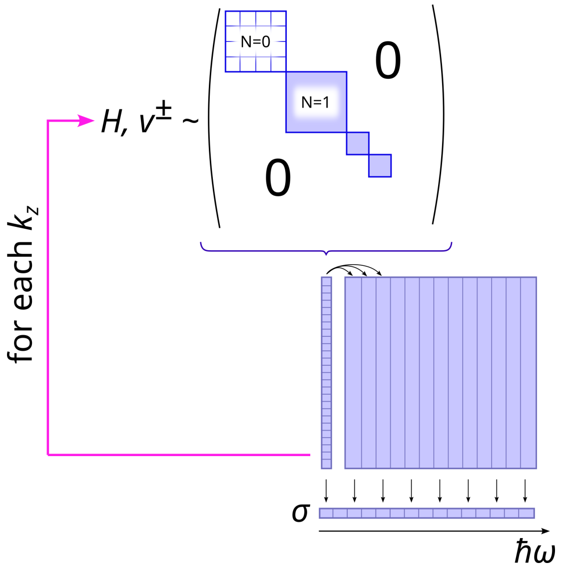

Figure 4.35: Parallelized and vectorized algorithm for fast and efficient computation of magneto-optical response $\sigma^{\pm}$. It makes possible to use the full topological insulator Hamiltonian on an average consumer computer with computational times within 15-20 minutes.

was exploited and the computation could be performed for the entire spectra in a vectorised manner in a single step. Upon next iteration, a different k_z element is used and σ iteratively updated for the entire spectra (fig. 4.35). Thus, an efficient algorithm employing the full general topological Hamiltonian was developed. It takes about 15-20 minutes to return the spectra at experimentally recorded fields and spectral range with 0.25 meV step on an average consumer computer. A few raw values of modeled σ are shown in fig. 4.36.

Optical conductivity is recalculated into the dielectric function, where we account for the uncomputed higher transition by including ϵ_∞:

$$\epsilon_{p,m}(E) = \epsilon_\infty + i\frac{\sigma_{p,m}}{\epsilon_0 E/\hbar}. \tag{4.120}$$

From ϵ, the absorption and reflectivity coefficients A and R can be calculated:

$$A_{p,m} = \Im(\sqrt{\epsilon_{p,m}})\frac{E}{\hbar c}, R_{p,m} = \left|\frac{\sqrt{\epsilon_{p,m}}-1}{\sqrt{\epsilon_{p,m}}+1}\right|^2. \tag{4.121}$$

In a volumetric piece of a bulk material, the intensity of transmitted light would be

$$I_T = (1-R)^2 e^{-Ad}, \tag{4.122}$$

but due to multiple reflections inside the thin film, there appears an additional modulation:

$$I_T = (1-R)^2 e^{-Ad} \times [1 + R^2 e^{-2Ad} + R^4 e^{-4d} + ...] = \frac{(1-R_{p,m})^2 e^{-Ad}}{1-R_{p,m}^2 e^{-2Ad}}. \tag{4.123}$$

To get the transmission in an unpolarised light, the average of the two polarisations is calculated: $T_B = (T_B^{\sigma^+} + T_B^{\sigma^-})/2$. To model the magnetotransmission, the

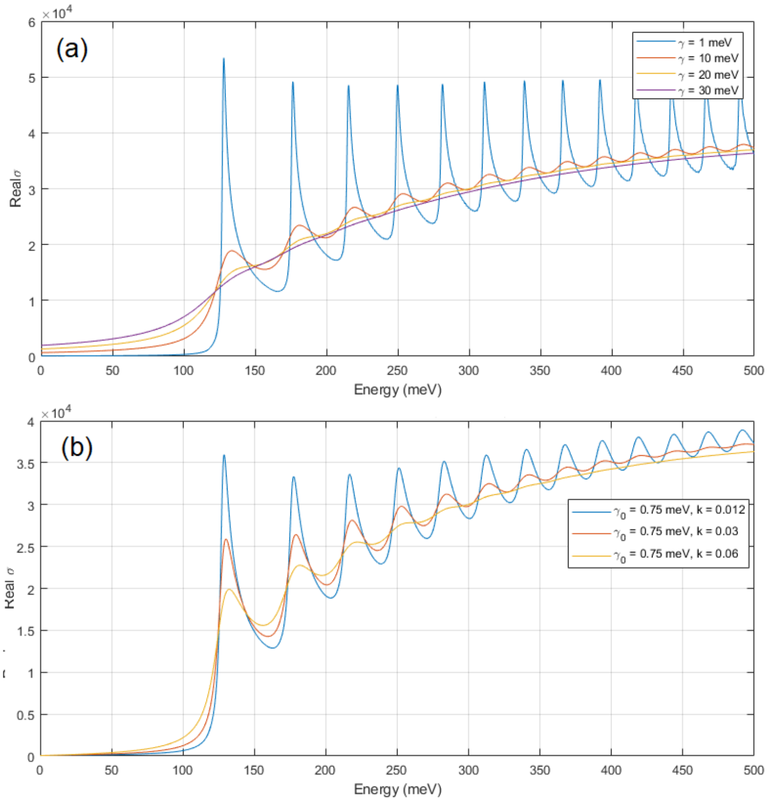

Figure 4.36: Modeled σ using the Kubo-Greenwood formula 4.117 for a few broadening scenarios: constant (a) and linear on energy (b). For small γ, σ becomes essentially a series of overlapping j_{DOS} corresponding to each LL.

reference spectra was modeled at $B = 1$ T, below the onset of any experimentally observed LL transitions.

The Kubo-Greenwood formula allows to include the effect of broadening via γ. So it is another adjustable parameter in our model. The simplest choice—a parameter independent of the energy and magnetic field—led to acceptable results (fig. 4.37). A value of $\gamma = 2$ meV was chosen, consistent with the onset of observed of LL quantisation at 2 T. The agreement could be further improved by taking an energy-dependent broadening increasing linearly: $\gamma = \gamma_0 + \kappa\hbar\omega$ with γ_0 meV and $\kappa = 0.0125$. This choice resembles the empirical rule deduced for interband inter-LL excitations in graphene [113, 114]. Notably, for relatively weak disorder, the width of excitations is not entirely determined by the γ parameter. The pronounced high energy tail of interband inter-LL excitations appears due to excitations at nonzero k_z momenta. Moreover, even though the electron-hole asymmetry was not directly evidenced in our data, it may still influence the width of transitions. This latter contribution would be roughly equal to the difference between the cyclotron energies of electrons and holes.

There is a fairly good agreement between the experiment and the model at higher photon energies, both for the shape and intensity of modulation. At lower energies, a certain deviation may be observed in the range corresponding to the excitations of electrons from the valence band to the vicinity of the Fermi energy in the conduction band. The relatively pronounced maximum in the theoretical T_B/T_0 spectra (around 120 meV in fig. 4.37) is not observed experimentally. It

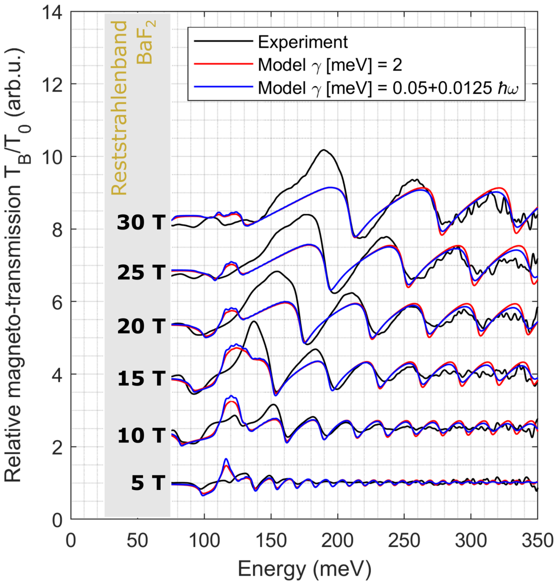

Figure 4.37: Relative magneto-transmission spectra T_B/T_0 at selected values of the applied magnetic field compared to those calculated using the linear-response theory (4.117) for sample C. To calculate T_B and T_0, the Landau levels up to the index 20 and 200 were included, respectively. The contribution of excitation at nonzero momenta were taken into account up to $k_z = 1.25$ nm^{-1}. Two cases have been considered to account for the disorder in the system: $\gamma = 2$ meV (red curve) and $\gamma = 0.05$ meV $+ 0.0125\,\hbar\omega$(blue curve).

appears in the calculated spectra as a result of B-induced splitting of the interband absorption edge for opposite circular polarisation of the incident light. In our experimental data, this feature seems to be smeared out due to the inhomogeneity of the electron density (fluctuation of the Fermi energy) across the explored sample. The overall matching of experiment and the model is shown also in figure 4.38.

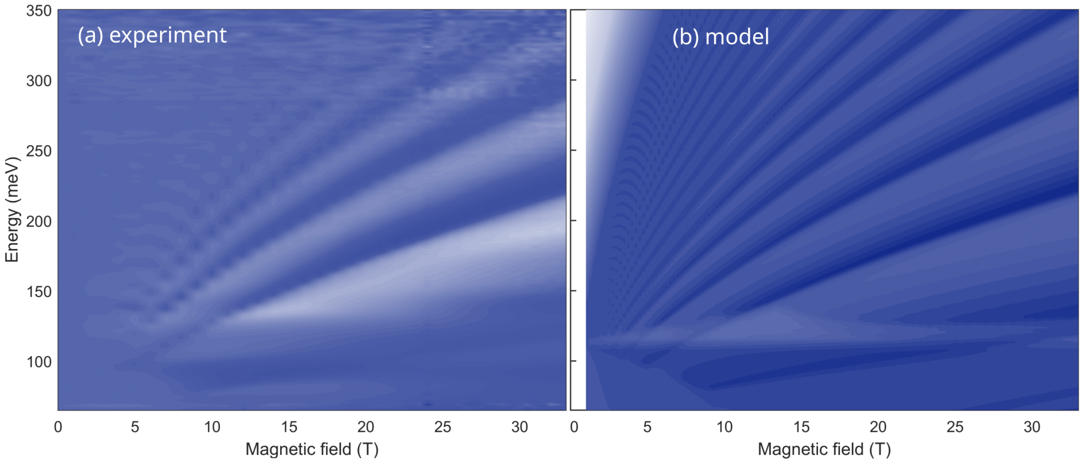

Figure 4.38: Experiment (a) and theoretical (b) map of magnetotransmission for sample C. White area in the upper left corner (at the highest fields) marks the highest Landau levels up to $N = 200$. Modeling higher order levels proved impractical in terms of computation time. There, the magneto-optical response is represented mostly by ϵ_∞.

4.6.2 ϵ modeling using WIEN2k

The aim of this section is to verify the band structure parameters Δ, v_F, M determined earlier. They should be accessible via first-principles *ab-initio* calculations. Essentially, the idea is to solve the general many-body problem of electrons in a solid. The Hamiltonian of such a system can be described by

$$H_{total} = \underbrace{T}_{\substack{\text{kinetic}\\ \text{energy}}} + \underbrace{U_{en}}_{\substack{\text{electron-nucleus}\\ \text{potential energy}}} + \underbrace{U_{ee}}_{\substack{\text{electron-electron}\\ \text{potential energy}}} + \underbrace{E_H}_{\substack{\text{Hartree}\\ \text{energy}}} + \underbrace{E_{xc}}_{\substack{\text{exchange-correlation}\\ \text{energy}}} . \tag{4.124}$$

This problem with $3N$ variables (coordinates of each interacting electron) is simplified in the **electron density functional theory** (DFT). It reformulates the many-body problem in effectively a single-particle fashion [115]. The Hohenberg-Kohn theorem asserts that the density of any system determines all ground-state properties of the system. In this case the total ground state energy of a many-electron system is a functional of the density $n(\vec{r})$. The total energy of a system can therefore be deduced using the electron density functional [116]. In DFT, it is postulated that the correct ground energies can be recovered upon the choice of a suitable functional depending on $n(\vec{r}) = (\Psi, \psi^*(\vec{r})\psi(\vec{r})\Psi)$, where Ψ is the many-body ground state wavefunction and $\psi(\vec{r})$ is an appropriate field operator. This functional is universal, applicable to an arbitrary number of particles and the potential $v(\vec{r})$ [117]. The effort is thus refocused on finding this functional. Many approximations are available, from general-purpose to specific systems. They require to choose the exchange-correlation (XC) term with its energy defined as $E_{XC} = \int \epsilon_{XC}(\vec{r}) \mathrm{d}^3 r$. One well-known XC functional is the local density approximation (LDA), where the XC energy depends only on the electron density ρ and is suitable for homogeneous materials. In another generalized gradient approximation functional GGA suited for less homogeneous materials, it also depends on its first derivative $\nabla\rho$. The interacting many-body system of electrons is mapped onto a non-interacting system of quasiparticles, characterized

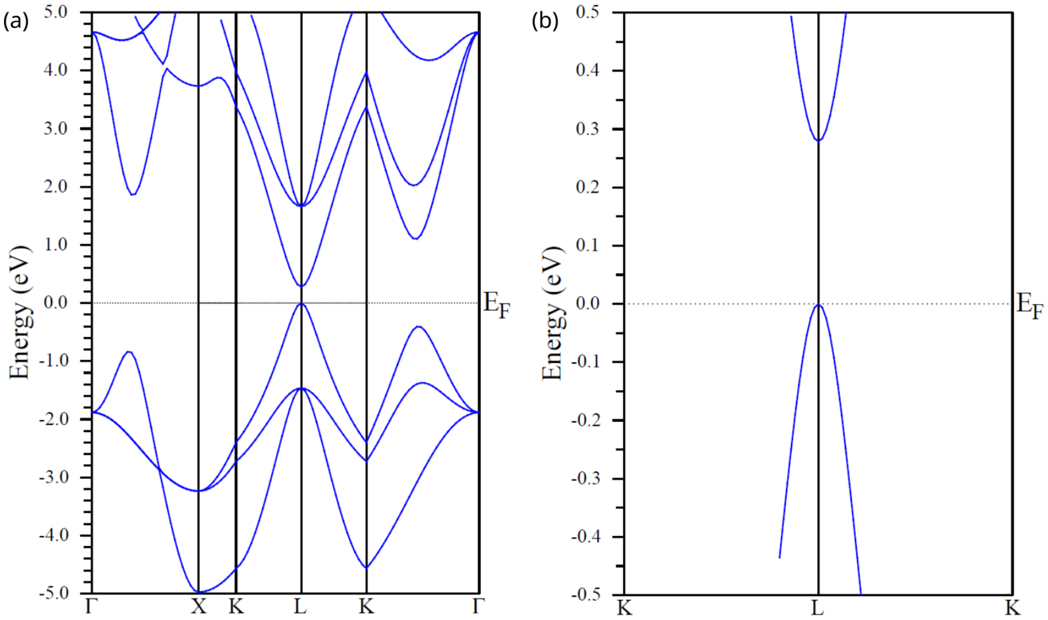

Figure 4.39: The energy band structure of PbSe alloy calculated with Wien2K along the most important k points. The Fermi energy was arbitrarily set to zero. The gap is located at Γ which is also zoomed in (b). Our simulation gives the value between 250-300 meV, which agrees reasonably well with experimental values.

by Kohn and Sham (KS) orbitals with a specific KS energy [118]. We used the WIEN2k package solving these equations using the linearized augmented plane wave (LAPW) method with localised orbitals, or LAPW+lo. It applies different optimized wavefunctions belonging to the atomic spheres and the interstitial (i.e. empty) region [119]. WIEN2k features the possibility to use an arbitrary number of local orbitals, which allows an accurate calculation of all states, from the low-lying occupied semi-core to the high-lying unoccupied states. In the Born-Oppenheimer approximation, the nuclei are considered to be at rest [118]. As a by-product, the KS orbitals/energies yield the PbSe parent compound band structure sketched in fig. 4.39, in agreement with other reports [28, 30, 31, 33].

The optical response of the material can be determined from its band structure. Direct transitions conserving $\vec{k}$ use the independent-particle approximation. The transition probabilities are given by the square of the momentum matrix elements between the occupied and empty states $M = \langle n'\vec{k}|\, A \cdot p\, |n\vec{k}\rangle$, where A is the vector potential. The matrix elements determine the probability of optical transitions using dipole selection rules as well as clearly distinguishes allowed and forbidden transitions. The Kubo formula allows expressing the optical response in terms of the joint density of states, the first approximation to spectral optical properties such as absorption. It can be done if i) the matrix elements are k-independent and ii) band index-independent. The vector potential A holds the information about light polarisation. The formula used in 4.117 deals with circularly-polarised light and its interaction with LLs. The optics module of WIEN2k, on the other hand, expresses the optical response in terms of the permittivity in linear basis at zero magnetic field. This changes the normalization factors and summation - it now runs over the energy bands instead of LLSs, and

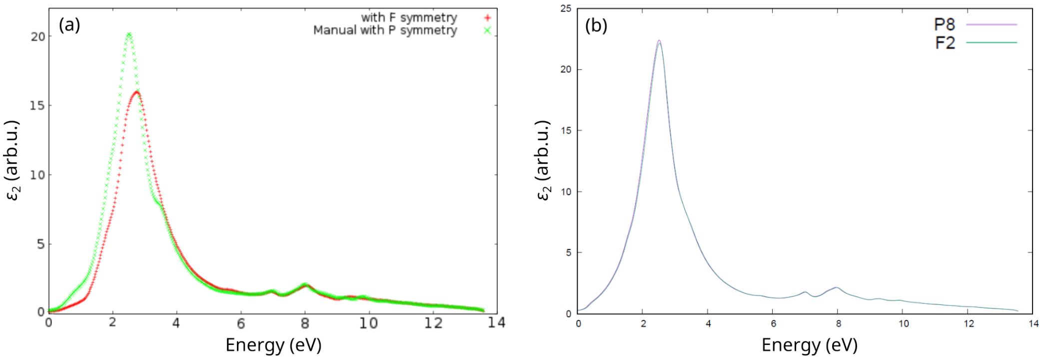

Figure 4.40: The final simulation result - the physical quantities such as the permittivity - depend on the k space sampling grid. Convergence tests between F and P symmetries for PbSe revealed 1 000 points (a) to be insufficient. Only starting from 10 000 points results become trustworthy. An example obtained using 50 000 points is shown in (b).

over all components of the momentum vector $\vec{k}$ [120]. It calculates the imaginary part of the permittivity ϵ_2 while the real part ϵ_1 is obtained via the Kramers-Kronig relationship [118].

To obtain the optical properties, the k space has to be sampled with a certain grid. Besides that, both F and P symmetries have to ultimately reproduce the same physical properties. Convergence tests show 1 000 k points to be insufficient while 10 000-50 000 generated practically identical results (fig. 4.40).

The broadening is included by smearing the entire spectra via the Lorentz or Gaussian oscillator, and is purely a post-processing step in WIEN2k. On the other hand, it could be in principle included as the broadening parameter γ in Kubo formula, as it is done in eq. 4.117. The weakest broadening produced spectral features that were not observable experimentally, with all critical energies clearly visible as shoulders, kinks or peaks in the spectra (fig. 4.41). To better reproduce the experimentally registered ϵ, the broadening had to be increased severalfold, to about 50 meV and higher (fig. 4.41).

The program employs crystal symmetries that allow reducing the computation time. For PbSe, the so-called F symmetry is readily available, in which the user only describes the 2 base atom species (lead and selenium). The full primitive cell is then mimicked via the help of symmetries in calculations. On the other hand, one can also define the entire primitive cell entirely manually. This requires populating it with 8 atoms instead of just 2, which inevitably results in longer computation times. This expense allows to simulate the quasi-random lead tin selenide alloy by replacing Pb atoms in the unit cell. The downside of WIEN2k is that once this cell is defined, the material is considered to be a perfect periodic crystal in all directions. It is thus incapable of directly simulating a random alloy. To bring the simulation closer to reality, we have replaced 1× Pb atom out of 4× with 1× Sn atom, and this was done for all 4× Pb positions. In other words, 4 semi-random crystal configurations were tested: with 1st lead atom replaced, with 2nd lead atom replaced, and so on. This effectively simulated an array of quasi-periodic $Pb_{0.75}Sn_{0.25}Se$ alloys. Different spatial configurations of tin do not change most of the critical energies such as E_1 or E_4 and E_5 and higher (fig. 4.42).

To better simulate the random nature of the alloy, a supercell concept can be

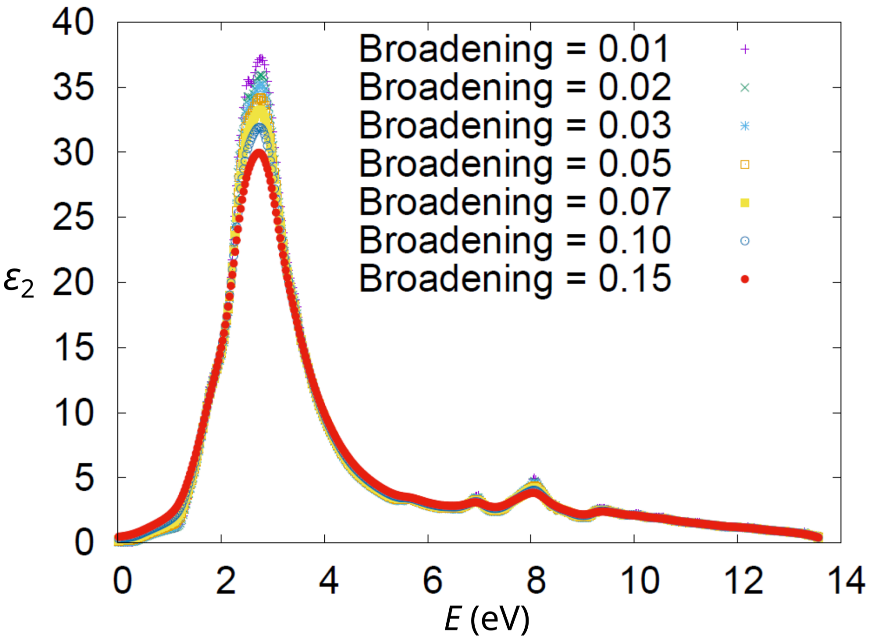

Figure 4.41: Broadening is an entirely post-processing step in WIEN2k. Lowest values produced a too sharp spectra (violet color). On the other hand, all critical energies are visible as sharp features: the absorption edge - the gap E_0, shoulder at $E_1 = 1.6$ eV, the main peak $E_2 \approx 2.7 - 3$ eV, here clearly separated into two atomic transitions etc. Only starting from 50 meV the spectra became smeared enough to better reproduce experimentally registered ϵ_2.

applied. Instead of a single unit cell, a bigger cell is defined, in which several lead atoms could be replaced. The bigger the cell, the better the quasi-randomness, with the expense of significantly higher computation load (fig. 4.43). Therefore, the recipe would be the following: first, calculate an array of ϵ for all possible Sn atom positions (in the case of a single cell, 4 independent permutations are available; in the case of 2× supercell elongated in one direction $8*7 = 56$ permutations etc.). A real random alloy should exhibit a mix of these optical responses, and to reflect this, the final permittivity should be averaged. This, however, becomes computationally too demanding for a general-purpose consumer computer. Such a calculation was performed on a supercomputer in Ostrava, the IT4i cluster, but only the DOS were calculated (fig. 4.44). As with many DFT calculations, it under-estimates the band gap, which is a known (and commonly fixed with the so-called scissor operator) issue of ab-initio calculations [118]. In the calculated DOS spectra, it is roughly 100-150 meV. Overall, all calculated DOS spectra reproduce the same spectral structures. The DOS of the quasi-random supercells exhibit little to no change among each other (different Se atoms replaced) neither at the gap nor other spectral regions. In comparison, the gap of a pure PbSe alloy seems to be wider (yellow curve). All other spectral features of the supercells are shifted to lower energies. Because of the convention used in WIEN2k, the zero energy represents the Fermi level. Therefore, negative energies represent occupied and positive energies represent empty states.

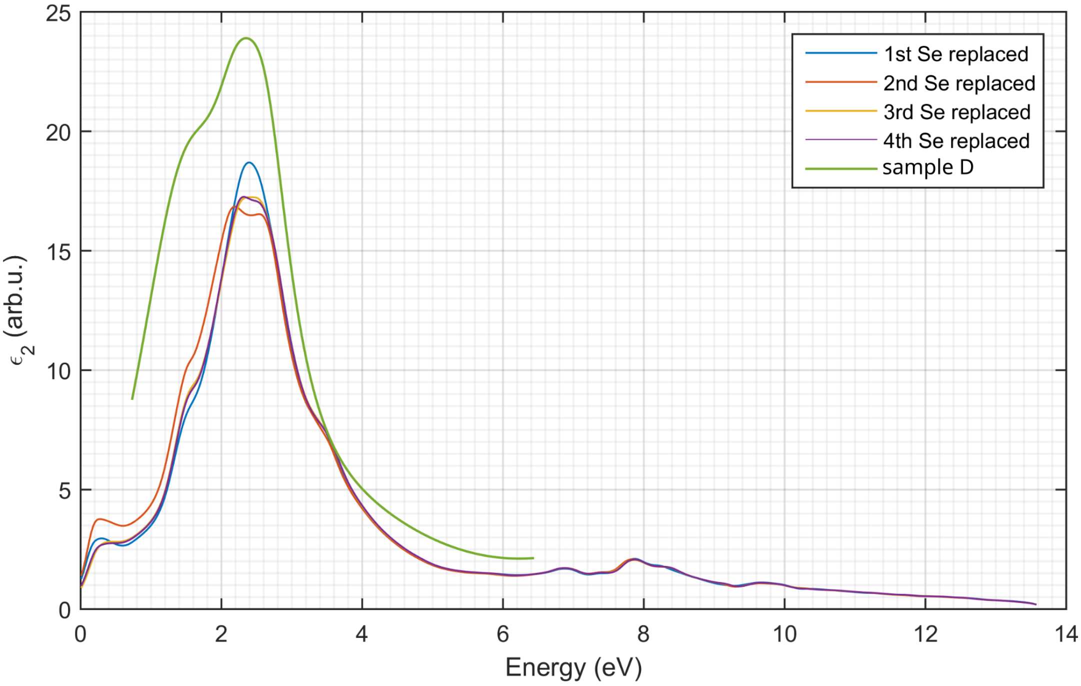

Figure 4.42: ϵ_2 for a quasi-periodic $Pb_{0.75}Sn_{0.25}Se$ compound compared to an experiment (green line). Different spatial tin configurations do not change critical energies E_1, E_4, E_5 and higher.

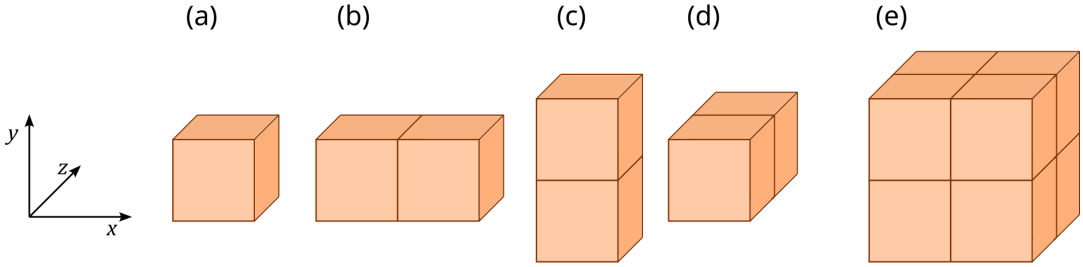

Figure 4.43: The supercell concept. Original PbSe unit cell (a) and its expansions in x (b), y (c) and z (d) directions. Supercell made out of 2 × 2 × 2 unit cells to imitate a quasi-random alloy such as $Pb_{1-x}Sn_xSe$ (d).

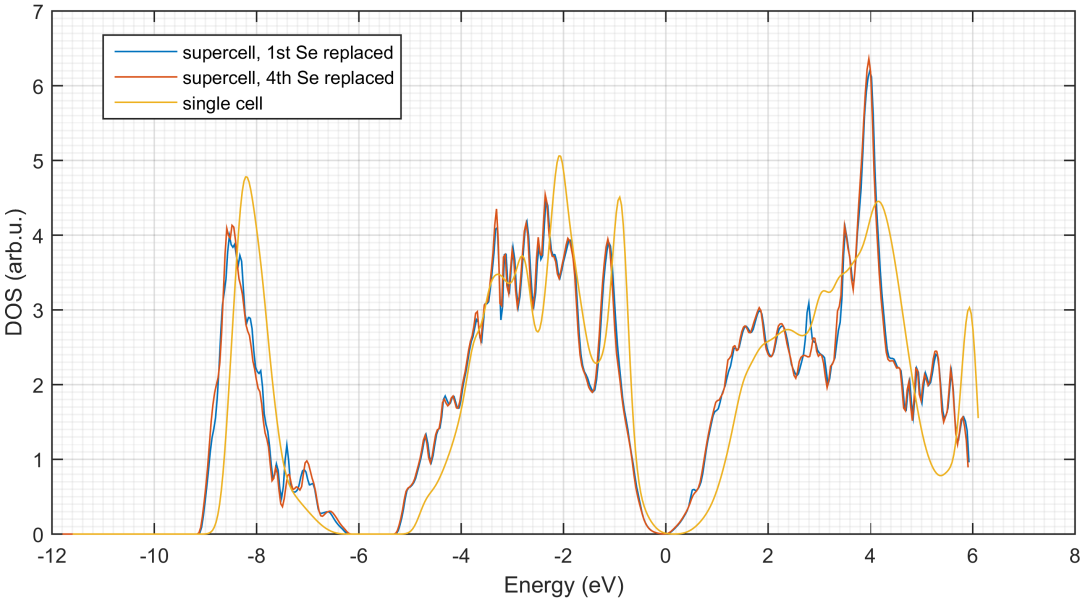

Figure 4.44: Density of states calculation of the regular primitive cell (7.5 meV broadening) and 8× supercell (2× in each direction). The supercell DOS were divided by 8 for easier comparison. All three curves reproduce the same spectral features such as the gap between 100 and 150 meV. Replacing different Se atoms produce very little change in the DOS but narrows the gap and shifts all spectral features to lower energies.

4.7 Search for surface states

The most salient feature of topological insulators is the conically dispersing Dirac-like surface states. It is thus in our interest to seek for any of their signatures in measured data. The primary question naturally becomes, where would they be expected? The general topological Hamiltonian is applicable to the entire material. To make it valid for the surface states, only a few modifications are required. We can quickly get the surface states dispersion formulas by excluding those terms that relate them to the bulk, i.e. the bandgap Δ and M. For the simplified case of $k_z = 0$, they read

$$E_{2D}(B,N) = \pm\sqrt{2\hbar e v_F^2 BN}, \tag{4.125}$$

and because of the electron-hole symmetry discussed in the chapter about the Hamiltonian for the bulk, the same simplifying rules apply. The excitations follow the standard electric-dipole selection rules in isotropic systems: $N \to N \pm 1$. All transitions of the surface states can be encompassed by

$$\hbar\omega_B(N) = E_{2D}(B,N) + E_{2D}(B,N+1), \tag{4.126}$$

with $N = 0, 1, 2, 3, \ldots$.

When the quantum limit of electrons in a conical band is approached, the fundamental cyclotron resonance (CR) mode emerges in the optical response. This mode comprises excitations of electrons among the $n = 0$ and 1 levels and becomes - in terms of the integral strength and absolute absorption -the most pronounced line in the transmission spectrum. This simple empirical rule can be justified using the standard linear-response theory. Therefore, we focused on this particular excitation in order to find a magneto-optical signature of the surface states in PbSnSe. We applied high magnetic fields to the samples to drive surface electrons close to their quantum limit. At the same time, their fundamental CR mode is expected to move above the reststrahlen band of $\mathrm{BaF_2}$. Hence, it should be traceable using the infrared magnetotransmission technique. One can estimate at what energies these transitions should occur. The CR excitations of the bulk for $k_z = 0$ case are described by $\Delta E = E_{N\pm1}^{val,\pm} - E_N^{val,\pm}$, and for the ground CR transition in particular

$$\hbar\omega_B = E_1^{val} - E_0^{val} = \sqrt{\left(\Delta + \frac{2M}{l_b^2}\right)^2 + 2v_F^2\hbar eB} - \Delta. \tag{4.127}$$

For the ground surface state transition,

$$\hbar\omega_B = v_F\sqrt{2\hbar eB}. \tag{4.128}$$

The latter fact is illustrated in Fig. 4.45. The LL spectra of bulk and surface electrons, expected for sample C, are shown in panel (a), along with the estimated Fermi energy. In panel (b), we present a false-color plot of magneto-absorbance of sample C overlaid with the expected energies of bulk and surface inter-LL resonances. The panel (b) shows that the fundamental CR mode of surface electrons should be accompanied by two bulk resonances at nearby energies – the fundamental bulk CR mode and the lowest bulk interband inter-LL transition.

These three excitations are marked by green, cyan and black vertical arrows in Fig. 4.45a. The same color-coding is used for curves in Figs. 4.45b. The dotted parts of the theoretical curves indicate the magnetic fields at which the final-state Landau level is occupied, and therefore, the transition should not appear due to Pauli blocking. Here we considered the bulk Fermi energy to determine the occupation of the surface LLs.

To explore the magneto-optical response in detail, the differential magneto-transmission spectra, $T_B/T_{B-\delta B}$, were analyzed (Fig. 4.47a-f). As discussed in the Sec. 4.4.2, the impact of a weakly field-dependent Fabry-Pérot interference pattern is partly suppressed in the differential spectra and we may better follow individual inter-LL resonances. Each transition manifested as a minimum in the relative magneto-transmission, T_B/T_0, is now expected to be seen as a derivative-like feature (a maximum followed by a minimum) in the differential spectra $T_B/T_{B-\delta B}$. To facilitate our analysis, the theoretically expected positions of the three lowest excitations are marked by vertical arrows in Fig. 4.47a-f, using the color-coding introduced in Fig. 4.45. The transparent arrows correspond to excitations blocked by the occupation effect. Again, we assume here that the occupation of the surface LLs is given by the bulk Fermi energy. Following these assumptions, the fundamental CR mode of surface electrons should be observable above the reststrahlen band of BaF_2 in all explored epilayers, except sample D.

Because of the volume of the bulk compared to the surface area, the surface state excitations are naturally expected to be weaker. The question is, just how much? We estimated their strength using a simple transfer-matrix method based on Yeh's formalism [121] similar to what was done for graphene multilayers [122]. In this method, the orthogonal input and output polarisations are related via the transform,

$$\begin{pmatrix} a_{N+1} \\ b_{N+1} \end{pmatrix} = M \begin{pmatrix} a_1 \\ b_1 \end{pmatrix} \tag{4.129}$$

with the master transfer matrix

$$M = D_{1\to 2}P(d_1)D_{2\to 3}P(d_2)...P(d_N)D_{N\to N+1}, \tag{4.130}$$

The interface and propagation matrices $D_{m\to n}$ and $P(\Delta z)$ are derived from field boundary conditions:

$$P(\Delta z) = \begin{pmatrix} e^{-ik_z\Delta z} & 0 \\ 0 & e^{ik_z\Delta z} \end{pmatrix}, \tag{4.131}$$

$$D_{m\to n,pol} = \frac{1}{2}\begin{pmatrix} 1+\eta_{pol}+\xi_{pol} & 1-\eta_{pol}-\zeta_{pol}\xi_{pol} \\ 1-\eta_{pol}+\zeta_{pol}\xi_{pol} & 1+\eta_{pol}-\xi_{pol} \end{pmatrix} \tag{4.132}$$

with η, ξ, ζ_{pol} representing either the s or p polarisation pol. These quantities are defined as follows: $\zeta_s = +1$ for s polarisation and $\zeta_p = -1$ for p polarisation, while

$$\eta_p = \frac{\epsilon_1 k_{2z}}{\epsilon_2 k_{1z}}, \xi_p = \frac{\sigma k_{2z}}{\epsilon_0\epsilon_2\omega}, \tag{4.133}$$

and

$$\eta_s = \frac{k_{2z}}{k_{1z}}, \xi_p = \frac{\sigma\mu_0\omega}{k_{1z}}, \tag{4.134}$$

with μ_0 the vacuum permeability. Because of the spin polarisation of the ground state, one component of the circular optical conductivity was considered inactive, setting $\sigma_1 = 0$. The other component σ_2 was calculated via the Kubo-Greenwod ofrmula. The transmittance is defined by the M_{11} matrix component:

$$t = \frac{1}{M_{11}}. \tag{4.135}$$

In experiment, to describe unpolarised light, again an average of the two resulting polarisations was used to keep the model correct. The PbSnSe epilayer was modeled as a dielectric slab with a thickness d and a refractive index of $n_{PbSnSe} = 5$. The optical response of the surface/interface states was described by the 2D dynamical magnetoconductivity. It comprised a single mode at $\hbar\omega = E_{2D}^{N=1}$, with the broadening parameter $\gamma = 2$ meV extracted from the bulk response, and the integral strength corresponding to the fourfold degeneracy. We assumed that this mode emerges when the bulk Fermi energy drops below the $n = 1$ LL of surface electrons. The substrate was represented by a dielectric slab with a thickness of 500 μm and a refractive index of $n_{\mathrm{BaF}_2} = 1.4$. The calculated differential spectra (cyan dotted lines) were then plotted along with experimental data for sample C in fig. 4.45 together with the explicit Landau level structure for the bulk and surface states. The experiment data and predicted Landau level transitions for all samples are plotted in fig. 4.46. The inflection point in the calculated curves matches the energy of the fundamental CR mode of surface electrons, marked by vertical cyan arrows. When the fundamental CR mode is Pauli blocked, the arrows are transparent. Due to the interference effect, the calculated amplitude of the surface CR mode varies with the thickness of the epilayers. Nevertheless, the theoretically expected signal clearly exceeds the noise level for all investigated samples. For the sake of completeness, let us note that the strength of the CR mode is much lower as compared to free-standing graphene [114]. The difference in the velocity parameters reduces the strength roughly by a factor of four, further reduction occurs due to PbSnSe bulk slab and BaF_2 substrate. It is the so-called dielectric effect which suppresses the strength of the response due to a surrounding dielectric material. In the case of graphene sample, this happens from one side (bottom of the sample) where graphene interfaces with the SiC substrate (for instance, the same effect has been observed in graphene grown on 4H SiC, see [123]). This reduces the total strength of transitions.

From the experimental viewpoint, the differential spectra measured on samples C and F reveal no signatures attributable to the signal from the surface states. For other samples, certain features develop just above the reststrahlen band of BaF_2. Nevertheless, their position, amplitude and shape do not correspond to the expectations for surface electrons. The relatively pronounced minimum observed for samples A and E (around $\hbar\omega \approx 100$ meV at 30 T) is most likely due to bulk interband inter-LL excitations ($n = 0 \rightarrow 1$). Their position seems to be slightly overestimated in the bulk data modelling (black vertical arrows). The shape – a minimum instead of derivative-like profile – may suggest the presence of some additional weaker excitations. However, there is no solid argument connecting them with the surface states. Below we discuss three different scenarios that allow us to explain why no clear signatures of surface electrons were found in the magneto-optical response: (i) an occupation effect, (ii) disorder and (iii) too simplistic theoretical modelling.

(i) The occupation of surface states, or in other words the distribution of electrons among the surface LLs, may differ considerably from the one expected from

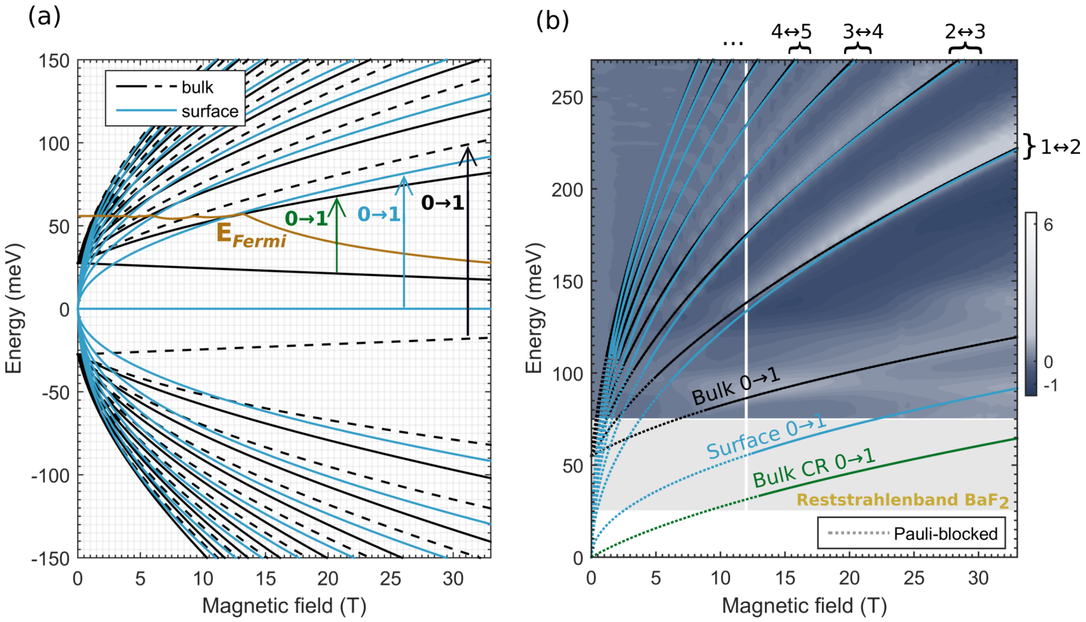

Figure 4.45: Part (a): Landau level spectrum of surface and bulk states and the expected Fermi energy in sample C as a function of B. The dashed and solid lines used for the LLs reflect the spin parameter $\alpha = -1$ and 1, respectively. The vertical arrows show three inter-LL excitations with lowest energies expected in the spectrum: the bulk interband $0 \rightarrow 1$ transition, and fundamental CR resonances of bulk and surface electrons. Part (b): False-color plot of relative magneto-absorbance measured on sample C compared to the theoretically expected positions of bulk (black and green) and surface (dark cyan) inter-LL resonances. The dotted lines correspond to the values of the magnetic field at which the transitions are not active due to occupation of the final-state LL (Pauli blocking). The vertical white line separates the data measured at low magnetic fields using a superconducting coil from the high-field data obtained with a resistive coil.

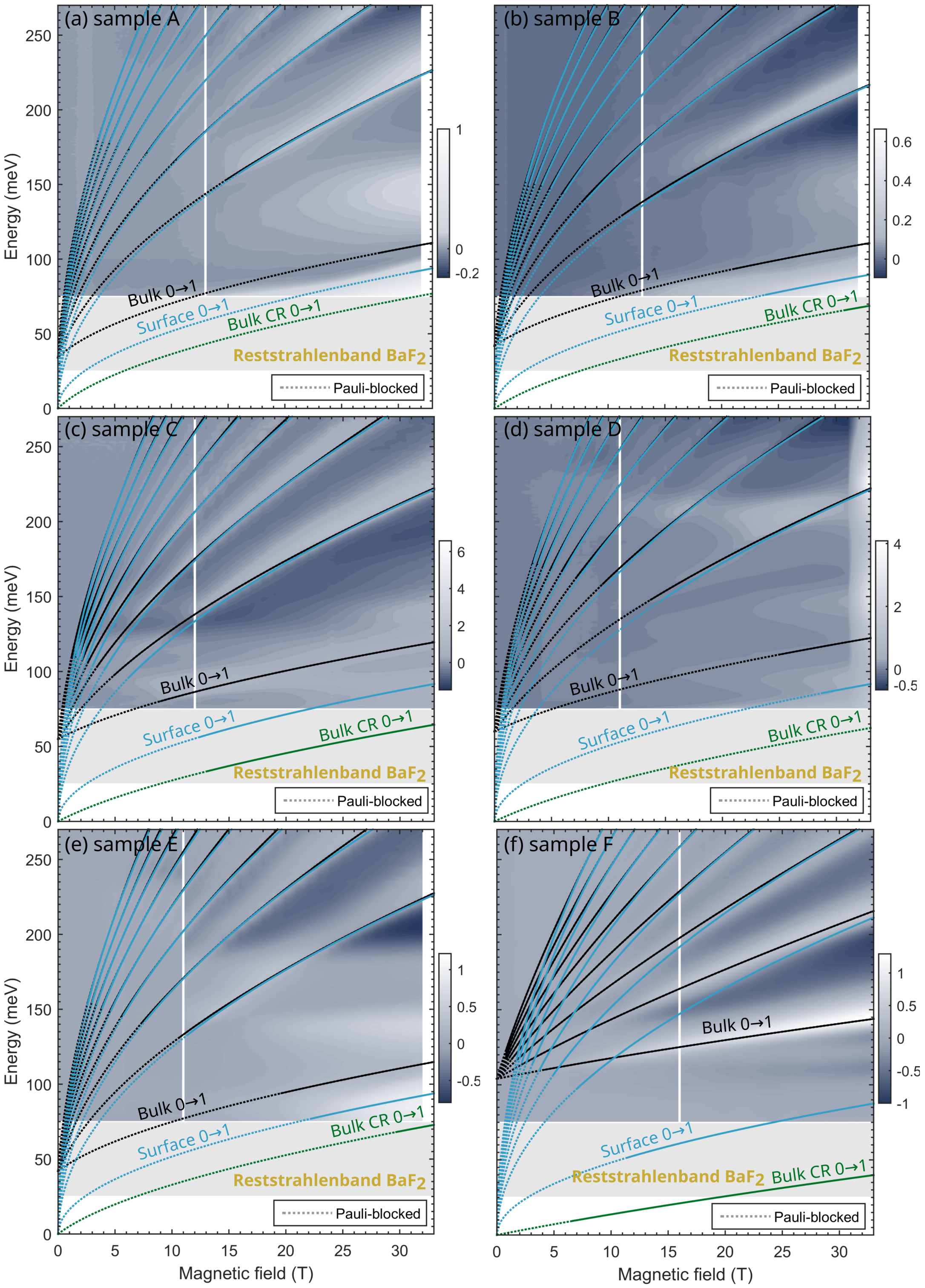

Figure 4.46: Experimental magneto-transmission maps with predicted bulk (black lines), bulk cyclotron resonance (green lines) and surface (cyan lines) Landau level transitions for all samples A-F. The dotted lines correspond to the values of the magnetic field at which the transitions are not active due to occupation of the final-state LL (Pauli blocking). The vertical white line separates the data measured at low magnetic fields using a superconducting coil from the high-field data obtained with a resistive coil.

the position of the bulk Fermi energy. The band bending close to the surface or interface of bulk crystals is a well-established phenomenon, often discussed in the context of topological (crystalline) insulators and other narrow-gap semiconductors. For instance, it might affect the emergence of the surface states because of existence of several well-defined surface transport channels with different mobilities and thicknesses due to strong bulk confinement [124]. ARPES, another technique of choice for directly probing the TIs bandstructure, is also affected, and can show distorted results [125]. This effect is governed by standard rules of electrostatics, and it may lead to the appearance of both depletion or accumulation of bulk electrons near the surface/interface [126]. The latter possibility could explain the lack of signatures of surface states in our data. Nevertheless, for the investigated samples with relatively large electron doping, and consequently large density of positively charged defects, a relatively narrow depletion layer and only a weak band-bending effect are expected. The penetration depth of the surface states can be estimated from the topological Hamiltonian eigenfunctions $\Psi \sim e^{\Lambda_\alpha z}$. The real part of Λ_α is the inverse localisation length, or alternatively, the penetration depth of surface states into the bulk d_α [127]:

$$d_{\alpha=-1} = \frac{\hbar v_F}{E_g}. \tag{4.136}$$

The estimated d values for our samples are presented in table 4.10.

Table 4.10: Estimated thicknesses of the surface states

Sample	$d_{\text{penetration}}$ (nm)	Ratio to sample thickness (%)
A	19.8	2.5
B	24.6	3.5
C	10.5	0.4
D	9.7	0.4
E	16.1	0.6
F	5.3	0.5

(ii) The topological protection makes surface states robust against the opening of a band gap, but they still remain sensitive to disorder, which is ubiquitous in a random alloy (note that Sn atoms do not replace Pb atoms in any periodic or regular manner). In magneto-optical experiments on 2D systems, the strength of disorder is directly reflected by the widths of inter-LL excitations. In our rule-of-thumb model for the fundamental CR mode of surface electrons, we considered the characteristic broadening equal to that of bulk states. In this way, we might have neglected additional sources of disorder, such as the surface/interface roughness or surface point defects. In fact, our transfer-matrix simulations suggest that an increase of γ by a factor of 3–5 brings the calculated magneto-optical signal of the surface states down to the experimental noise level. Disorder in the surface states thus may represent a plausible explanation of the apparently missing signal from the surface electrons.

(iii) The accuracy of the existing theoretical models represents another possible explanation. Clearly, there is no apparent reason to question their general validity [14, 128], notably, when they are convincingly corroborated by various experimental studies [94]. At the same time, however, it is not obvious to what extent these models account for the surface states quantitatively; strictly speaking, the concept of band structure does not even apply to a random alloy, which $Pb_{1-x}Sn_xSe$ is. Cushioning such fundamental doubts, the dispersion of the surface states does not need to have its Dirac point in the midgap position (reflecting the weak but present electron-hole asymmetry at the L point). This would effectively correspond to a higher Fermi level for the surface states, thus pushing the quantum limit to larger magnetic fields and making the fundamental CR mode of surface electrons hardly observable in our experiments. In addition, one may expect a certain deviation from the linearity of the conical band on the surface, which is not included in the simplest model [128]. The fundamental CR mode of surface electrons could thus have a lower energy and stay hidden within the reststrahlen band of the BaF_2 substrate even in the highest magnetic fields applied in our experiments. Hybridization of surface and bulk states is another possible effect. Sticking strictly to the standard theoretical model [128], the bulk and surface states are truly eigenstates of a semiinfinite crystal, and they do not mix with each other. At the same time, the discrete surface LLs coexist—apart from the interval in between zero-mode levels—with the quasicontinuum of bulk electronic states, and one may speculate about mechanisms that mediate their coupling. The hybridization of surface and bulk states (such as the one taking place in type-II surface states of the (001) projection [128]) may represent an explanation—an alternative to plain disorder—for spectrally broad features observed above the reststrahlen band of BaF_2 in the differential spectra of the A, B, D, and E samples.

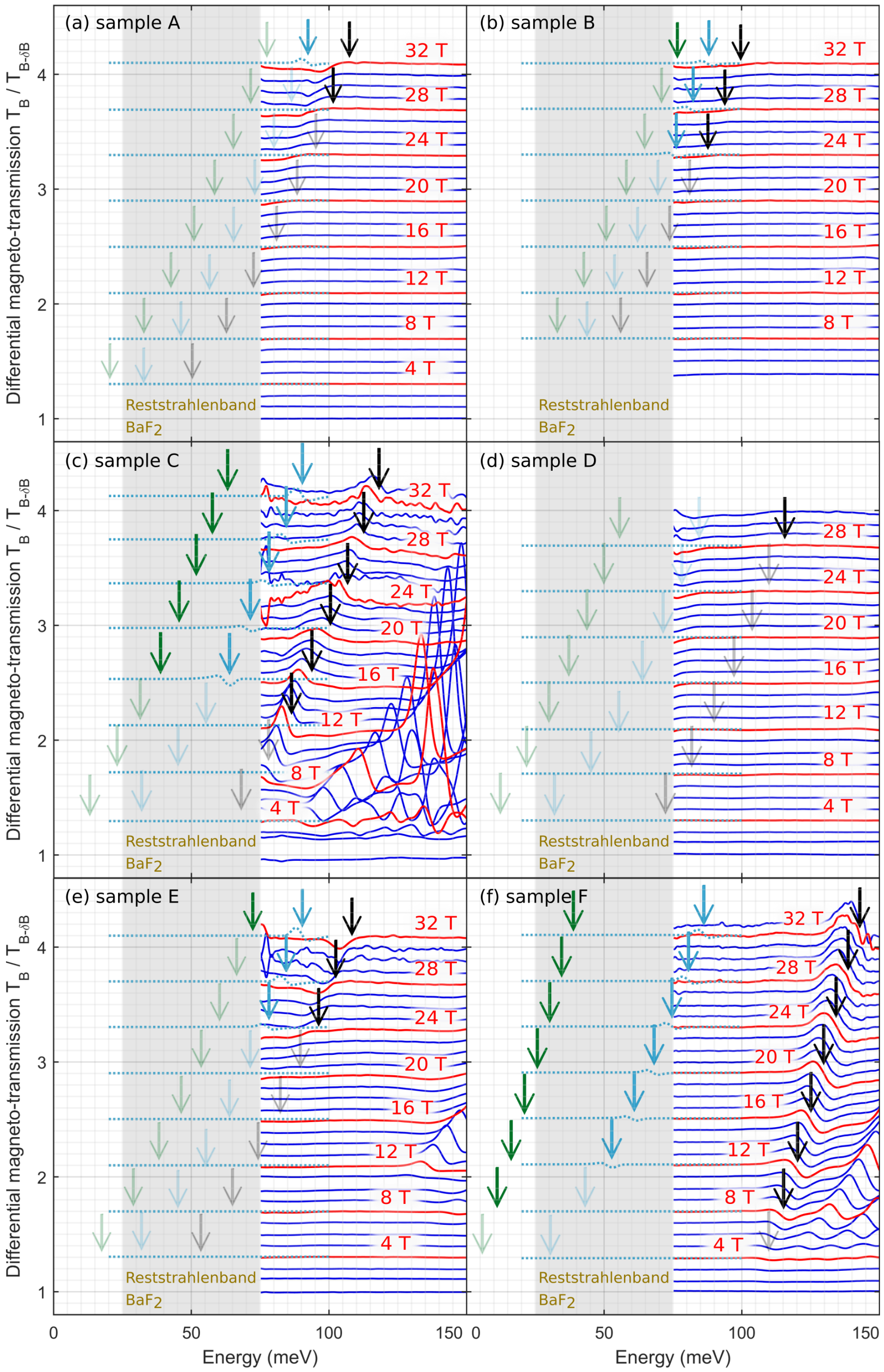

Figure 4.47: Differential magneto-transmission spectra, $T_B/T_{B-\delta B}$, plotted for all explored samples A, B, C, D, E, and F in parts (a)-(f), respectively, using the difference $\delta B = 1$ T. The spectra are shifted vertically, with the offset scaling linearly with B. The energies of three excitations having the lowest energy in the quantum limit of bulk and surface states are marked by the vertical arrows (cf. Fig. 4.45b): green – the bulk fundamental CR mode, dark cyan – the fundamental CR mode of surface electrons and black – the lowest interband inter-LL transition ($n = 0 \rightarrow 1$). Transitions are expected to emerge in the spectra (following the occupation effect) when transparent arrows change into solid ones. The dotted cyan line is the theoretically expected response, the differential magneto-transmission, due to the fundamental CR of surface electrons, calculated using the transfer-matrix method, see the text. Neither bulk inter-LL resonances, nor the presence of the reststrahlen band, are included in this model for simplicity.

V Epitaxial graphene

We now turn the attention to another material investigated in this thesis, graphene. The introduction its most general properties was given in the introductory chapter 2.3. In this part, we will concentrate on the experimental data performed on graphene manufactured in a particular, cost-effective manner, the epitaxial graphene.

5.1 Graphene manufacturing methods

The thesis part about graphene is based on [48]. Graphene is a single atomic sheet of graphite. The first extraction of a real graphene sample is attributed to Novoselov in 2005, when it was cleaved from graphite using a sticky tape [129, 130]. Naturally, this method is not suitable for high-scale production due to a small footprint. On the other hand, exfoliated graphene provides the highest quality in terms of physical parameters [131–133]. Chemical vapor deposition (CVD) allows growing graphene multilayers on various surfaces [134–136] but sometimes requires additional steps to transfer graphene from the growth substrate to the application substrate.

In this regard, graphitization of the top layers of silicon carbide by annealing is an easy and cheap shortcut to help pass these limitations for mass production of multi- and especially monolayers. SiC starts to decompose at 1150°C and above. Si atoms sublimate at the surface while C atoms forms stable bonds staying below the surface, forming epitaxial layers of graphite/graphene. This technique is called the sublimation growth/thermal decomposition [137].

The lowest graphitized layer is covalently bonded to the substrate surface (fig. 5.1 (a)). Its atomic arrangement identical to graphene [137]. The bonding reduces the electron mobility and does not allow to develop the linear dispersion. Furthermore, chemical potential strongly depends on temperature, most probably due to strong substrate-graphene phonon coupling [138]. Intercalation of the interface layer by hydrogen (fig. 5.1 (b)) is an already proven method to suppress these bonds and produce the so-called quasi-freestanding monolayers having all of the graphene properties [139]. In order to utilize graphene in industrial mass production of multilayered devices as transparent electrode, it is convenient to know its optical properties in the broadest spectral range possible.

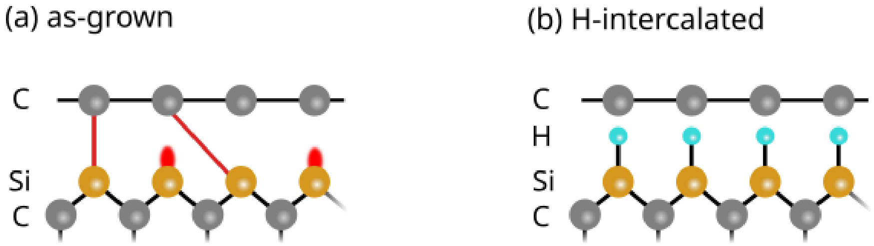

Figure 5.1: Annealed SiC with carbon atoms at the surface, held together by strong covalent bonds (a). Intercalation of the interface by hydrogen lifts off this layer from the substrate, forming true atomically flat sheet of graphene (b).

The graphitization is faster on the C-face but it also makes it difficult to ensure the growth of a single layer as usually multilayers are grown. Graphitization is slower and easier to control on the Si-face [140] because of more precisely controlled sublimation growth. A fixed orientation exists on SiC(0001) for the grown graphene layers while this is not the case for SiC($000\bar{1}$). Therefore, many prefer to grow graphene on the Si-face [137]. To the best of our knowledge, previous spectroscopic ellipsometry studies on graphene were focused on 3C-SiC and 4H-SiC allotropes [141–144]. There are only a few reports presenting optical properties of graphene grown on 6H-SiC in a limited spectral range [143, 145]. 6H-SiC is widely used in commercial device fabrication and could serve as the basis for graphene-based circuits and optoelectronic devices. Hence we examined the quasi-freestanding monolayer graphene obtained by the intercalation of Si-face 6H-SiC.

5.2 Graphene sample preparation and analysis

The investigated epitaxial quasi-freestanding monolayer graphene sample was prepared by annealing of 0.5 mm thick Si-face 6H-SiC at graphitization temperature of 1450°C and argon atmosphere. The quasi-freestanding graphene layer was obtained by hydrogen intercalation of a single layer of (0001) 6H-Si. The surface quality and morphology were measured by atomic force microscopy (AFM). Optical properties were investigated using a combination of J. A. Woollam's spectroscopic ellipsometers RC2 and V-VASE in order to cover to cover a broad spectral range. The RC2 ellipsometer allowed us to measure the Mueller matrix ellipsometry and unpolarised transmission data in the range from 0.7 to 5.5 eV. The transmission data served as an additional input allowing to account for the features near the SiC band gap such as the absorption edge, absorption tail etc. The V-VASE ellipsometer allowed to acquire experimental data in the IR region down to 0.150 eV. All measurements were preformed at room temperature under several angles of incidence ranging from 45 to 75 degrees. The light beam diameter was approx. 3 mm, yielding the average optical response from such an area. J. A. Woollam's 'CompleteEASE' software was used for advanced data processing. Obtained optical properties were compared to CVD grown graphene on silicon using standard approach.

5.3 SiC and graphitized SiC surface morphology

According to AFM measurements, the average width and height of SiC terraces of both sample and reference right after cleaving and an initial hydrogen etching is 1.243 µm and 0.75 nm (half unit cell; Fig. 5.2 (a)). This is caused by surface orientation not matching the nominally on-axis oriented SiC wafers. Typical step heights are 1 or 0.5 of a 6H unit cell [137]. It indicates a miscut angle of 0.03-0.04 degrees. Graphitization at temperatures above 1200°C promotes an additional microscopic surface restructuring, forming more steps. These steps tend to bunch together, and terraces become wider and higher on average. The final terrace morphology thus changes. Step bunching is a well-known phenomenon [137, 143, 146]. Sample surface area was about 5 × 5 mm, and in order to ensure statistically reliable surface morphology data of the graphitized hydrogen-intercalated sample, we have performed AFM measurements on 5 different places on the sample, each 20 × 20 µm: one in the centre and other four at every corner. The height of the terraces was estimated along the horizontal scanning direction so that any possible sample drift artifacts would be eliminated. According to the data, terraces became 1.4 nm high and 1.8 µm wide on average after bunching (Fig. 5.2 (b)). The terrace height was used as one of the input parameters for the ellipsometric data processing.

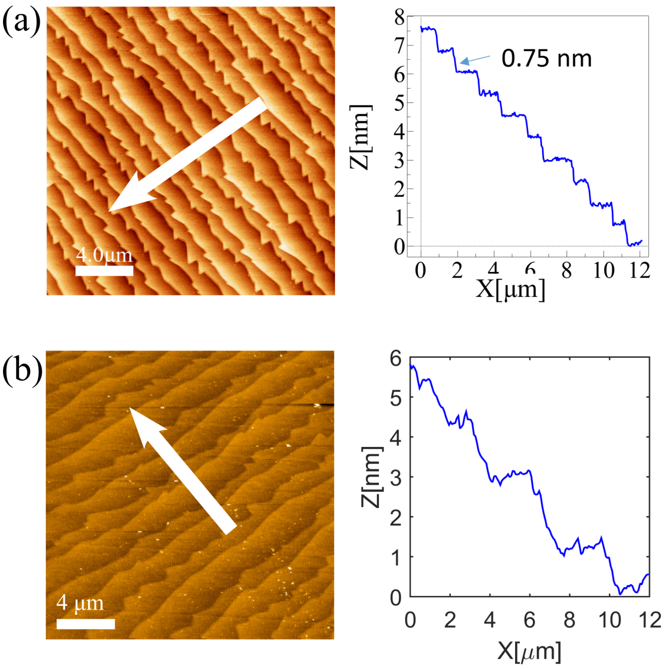

Figure 5.2: False color 2D AFM scan maps and selected profiles of intercalated reference SiC sample (a) and substrate + graphene sample (b). Only single profiles along the directions of the white arrows are shown for brevity. In (b), horizontal lines correspond to measurement artifacts. This complicated the baseline correction, distorting vertical distances in the subset on the right. To evaluate the precise average terrace height, raw uncorrected data at multiple spots were analyzed.

5.4 Spectroscopic ellipsometry data analysis

The reference bare SiC substrate and the graphitized sample, both prepared under the same conditions, were investigated. Prior to the graphitized sample, the optical properties of the bare substrate were characterized. Its optical response was then used as an input when fitting the dataset obtained on the graphitized sample. This decreased the set of parameters to be fit at once.

The reference SiC substrate was modelled as a bulk birefringent material. Its ordinary and extraordinary axes were modeled independently. Its permittivity was described by a sum of oscillators fulfilling the Kramers-Kronig relations. All substrate oscillators were chosen to be of Cody-Lorentz type as it allows to model a broad Lorentzian line shape with zero absorption below a defined absorption edge energy E_g. The definition of Cody-Lorentz oscillator is

$$\epsilon_{C-L} = \epsilon_1 + i\epsilon_2, \tag{5.1}$$

Table 5.1: Cody-Lorentz oscillator parameters for describing the reference 6H-SiC substrate dispersion.

Oscillator #	A (arb.u.)	γ (eV)	E_0 (eV)	E_g (eV)	E_p (eV)	E_t (eV)	E_u (eV)
ordinary axis:							
	$\epsilon_\infty = 1$						
1	112.930	0.851	7.403	2.939	5.725	0.0526	0.0598
2	4.850	12.095	12.207	2.939	14.304	0	0.0200
extra-ordinary axis:							
	$\epsilon_\infty = 1.371$						
1	60.907	0.581	7.202	2.929	3.333	0	0.187
2	56.422	0.122	5.371	2.929	15	0	0.154

The imaginary term in region $0 < E \leq (E_g + E_t)$ is

$$\epsilon_2(E) = \frac{E_1}{E} \exp\left(\frac{E - E_g - E_t}{E_u}\right), \tag{5.2}$$

while in the other region $E > (E_g + E_t)$ it is

$$\begin{aligned}\epsilon_2(E) =& G(E) \cdot L(E) = \\ & \frac{(E - E_g)^2}{(E - E_g)^2 + E_p^2} \cdot \frac{A E_0 \gamma E}{(E^2 - E_0^2)^2 + \gamma^2 E^2}.\end{aligned} \tag{5.3}$$

In the above equation, $G(E)$ represents the near-bandgap function and Cody absorption behavior while $L(E)$ is the Lorentz function. Here, $E_1 = (E_{gn} + E_{tn}) G(E_{gn} + E_{tn}) L(E_{gn} + E_{tn})$. Parameters A, γ and E_0 characterize a Lorentzian absorption peak. E_p describes absorption transition from Lorentzian to Cody behavior and E_t absorption transition from Cody to Urbach behavior. The absorption edge is described by E_g. The real part is analytically related via the Kramers-Kronig integral

$$\epsilon_1 = \frac{2}{\pi} P \int_0^\infty \frac{E' \epsilon_2(E')}{E'^2 - E^2} \mathrm{d}E'. \tag{5.4}$$

Several independent oscillators were required for each optical axis. The optical absorption edge energy parameter E_g was shared among all of them. The fitting procedure used all of the experimental data (ellipsometric quantities Ψ and Δ at multiple angles of incidence and IR optical transmission) simultaneously, resulting in the best set of oscillator parameters (amplitudes, energies and broadenings). The explicit parameters that gave the best match with experimental ellipsometry data are listed in table 5.1. The resulting permittivity follows the spectral trends reported in other studies on 6H SiC [147–152], and the absorption edge energy fitted to 2.93 eV.

Because the SiC substrate was polished from both sides and is transparent in almost the entire measured spectral range, backreflections from the back side of the substrate were observed, thus complicating data processing. The combination of the uniaxial anisotropy and reflections from the backside of the SiC substrate is responsible for the interference pattern below the SiC bandgap. This is also visible in graphene sample - see (Fig. 5.3 (a) and (b)).

The thicknesses of the surface terrace steps in all investigated samples estimated by the AFM measurement were in the order of several nm, much lower than the wavelength of the probing radiation. Light is thus unable to distinguish the exact structure of layers so thin. The terraces are hence treated as a separate surface roughness layer on top of the sample. It uses the Bruggemann Effective Medium Approximation (EMA) to describe the mixing of the optical response of the surrounding materials [153, 154]. It was composed of 50% air and 50% underlying SiC. Its initial thickness was set to the step height fas measured by the AFM. A reasonable fit was achieved and the interference pattern in the spectra of ellipsometeric parameters was reproduced well (not shown here).

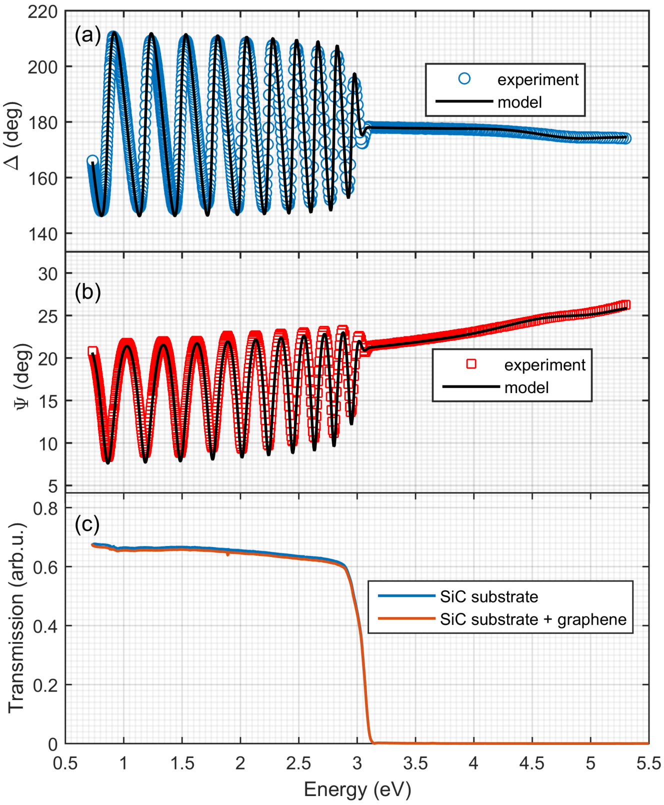

Figure 5.3: Comparison of experimental data and modelled spectra of the SiC substrate and graphene at 55 deg. of incidence. The main ellipsometric angles Δ (a) and Ψ (b) are provided. They exhibit oscillations induced by backside reflections. Transmission data of SiC substrate and SiC substrate + graphene sample (c).

Several model structures have been proposed to describe graphene sample. The thickness of monolayer graphene is taken as an interlayer spacing in graphite, e.g. 0.35 nm. In this case, it is much smaller than the height of the terrace steps (1.4 nm). We have evaluated various approaches to model the sample structure and to best fit the experimental data. The simplest models treated the structure as stratified layers of substrate and graphene with a potential additional surface roughness component. These approaches failed to deliver physically meaningful optical properties or did not fit to realistic layer thicknesses. Similar results and numerically unstable fits were obtained for more complicated model structures consisting of substrate, void layer and graphene, which supposed to reflect the terrace structure of the top layers.

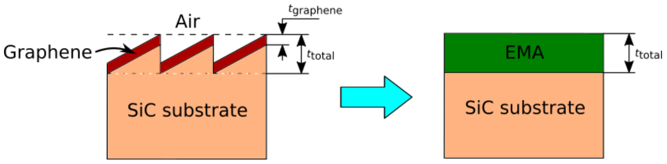

Figure 5.4: Schematic sketch of the chosen model structure used for the parametrization of optical properties of graphene layer.

Due to the atomic thickness of graphene and low terrace height, the light experiences an averaged refractive index of all involved materials at the surface. To maximally reflect the graphene layer structure with thin terrace steps, we have chosen model structure consisting of the SiC substrate covered with a Bruggemann EMA layer composed of 3 materials – the underlying SiC, graphene and air, as depicted in Fig. 5.4. The inclusion of air reflects the surface roughness. The optical properties of this layer are adjusted via the volume ratios of its components. The volume ratios of graphene, v_{graphene}, and interpenetrating air/substrate, v_{air} and $v_{\text{substrate}}$, range from 0 to 100% and are coupled. For low terrace angles they can be related to the total thickness t_{total} (in nm) of the top layer in the following way:

$$v_{\text{graphene}} + v_{\text{air}} + v_{\text{substrate}} = 100\%. \tag{5.5}$$

The air and substrate filling factors/ratios in the EMA model are the same according to a simple geometric argument:

$$v_{\text{air}} = v_{\text{substrate}}, \tag{5.6}$$

estimated as

$$v_{\text{air/substrate}} = \frac{(t_{\text{total}} - 0.35)}{t_{\text{total}}} \cdot \frac{1}{2} \cdot 100\%. \tag{5.7}$$

The initial thickness t_{total} of the top EMA layer was set to the step height as measured by AFM. Both its thickness and compositional parameters were varied in the fitting procedure to account for the variation in the step height or intercalated graphene coverage inhomogeneity throughout the sample.

In this thesis, a reliable Model Dielectric Function (MDF) of graphene over the entire investigated spectral range is proposed. The MDF is composed of several Kramers-Kronig consistent oscillator terms:

$$\epsilon = \epsilon_\infty + \epsilon_{\text{L1}} + \epsilon_{\text{G}} + \epsilon_{\text{L2}}, \tag{5.8}$$

where $\epsilon = \epsilon_1 + i\epsilon_2$. L stands for Lorentz and G for Gaussian oscillators. Adapted variants of these were used in this work. The Lorentz oscillator is defined as

$$\epsilon_{Lorentz}(E) = \frac{A\gamma E_0}{E_0^2 - E^2 - iE\gamma}, \tag{5.9}$$

Table 5.2: Fitted parameters of spectral dispersion of optical properties of quasi-freestanding graphene monolayer on 6H-SiC.

Oscillator type	*Amp* (arb.u.)	γ (eV)	E_0 (eV)
ϵ_∞	2.259		
Lorentz$_1$	16588.6	3.1482	0.001
Gaussian	4.8	4.6778	4.121
Lorentz$_2$	11.7	0.7369	4.581

while the Gaussian oscillator as

$$\begin{aligned}\epsilon_{Gaussian}(E) =& A\left[\Gamma\left(\frac{E-E_0}{\sigma}\right)+\Gamma\left(\frac{E+E_0}{\sigma}\right)\right]+\\ & i\cdot A\left[\exp\left(-\left(\frac{E-E_0}{\sigma}\right)^2\right)-\exp\left(-\left(\frac{E+E_0}{\sigma}\right)^2\right)\right]\end{aligned} \tag{5.10}$$

with

$$\sigma = \frac{\gamma}{2\sqrt{\ln(2)}}. \tag{5.11}$$

Here A stands for the amplitude, γ is the broadening parameter and E_0 is the central energy. The Γ function is a convergence series that produces a Kramers-Kronig consistent line shape for ϵ_1. The term L_1 qualitatively describes the permittivity in the lowest energy range that is affected by interference oscillations. We thus do not assign a deep physical interpretation to the fitted parameters of these oscillators. They serve purely to provide the spectral dependence of the MDF. Information about electronic parameters such as relaxation time etc. could be obtained by other more suitable experimental techniques, e.g., electronic transport measurements or Landau level spectroscopy.

The parameters of these dispersion terms were fit simultaneously with the t_{total} and volume ratios to the ellipsometric experimental data and optical transmission (see Fig. 5.3). The fit with the mean square error of 14.9 was achieved and the final step height was fitted to be 1.68 nm, close to the initial value of 1.4 nm. Resulting model spectrum of the ellipsometric angle Δ is also included in Fig. 5.3 a for comparison. Experimental and model spectra of the ellipsometric angles Δ and Ψ are shown in Fig. 5.3 (a), and transmittance in Fig. 5.3 (b). The resulting spectral dependence of the dielectric function of monolayer graphene compared to several spectra taken from literature is shown in Fig. 5.5. Included in the comparison is the CVD graphene grown on Si substrate. Its dielectric function was determined similarly by spectroscopic ellipsometry.

The fitted spectral dependence of monolayer graphene permittivity (shown in Fig. 5.5) clearly exhibits a narrow peak located at 4.56 eV. This energy corresponds to the critical point associated with the van Hove singularity in the joint density of states. It is related to the interband transitions between $\pi - \pi^*$ hybridized orbitals in the vicinity of the M point of the graphene Brillouin zone. Several reports have shown that in multilayer graphene systems, the position and appearance of multiple van Hove singularities can be tailored by twisting individual graphene layers, dramatically increasing light-matter interaction [57, 59**?**].

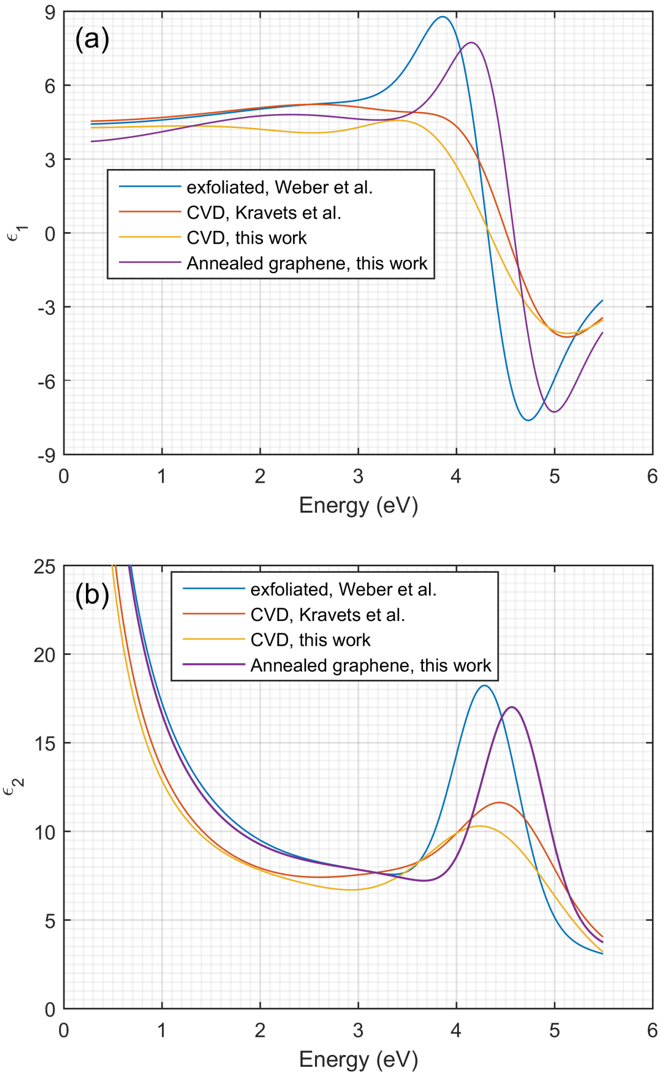

Figure 5.5: Real (a) and imaginary (b) parts of the epitaxial graphene dielectric function compared to literature spectra. Exfoliated graphene constants by Weber et al. are taken from [133] and CVD graphene by Kravets et al. from [132].

The main peak of the investigated sample is comparably as narrow as in exfoliated graphene, yet blue-shifted as in CVD graphene. When comparing the optical properties of the investigated sample with exfoliated graphene, one can see that the transition energy near the M point in the investigated sample is slightly increased, which might be the consequence of changes induced in the lattice during graphitization and step bunching. However, carbon covalent *sp* bonds are known to be very strong and robust, rendering this option unlikely. In the single-particle picture, the maximum of the absorption is theoretically expected around 5.1-5.2 eV [155]. Depending on the substrate and doping, the Coulomb interaction in graphene may remain, to a great extent, unscreened. This allows the charge interaction to take place. When excitonic effects and electron-electron interaction are taken into account [57, 132, 155**?**], they suppress and red-shift the peak which is observable in pristine exfoliated and CVD graphene samples. In a freestanding graphene, the shift has a well-defined value of $\sim$ 600 meV, down to 4.5-4.6 eV [132, 155–157]. For bilayer graphene, the red-shift is even stronger,

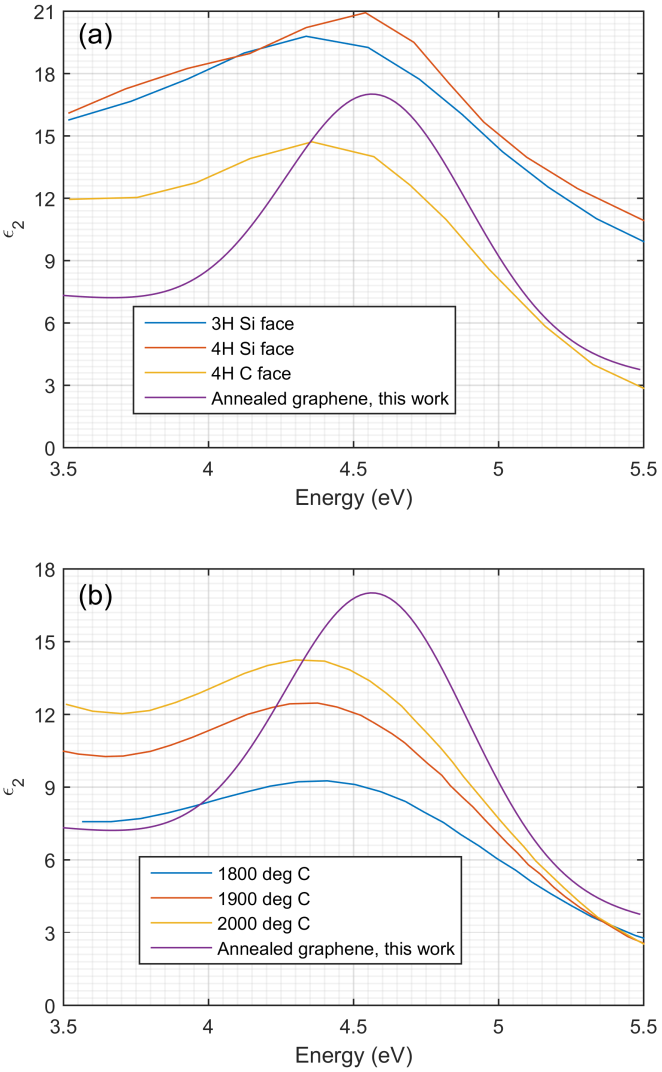

Figure 5.6: The imaginary part of the dielectric function in the region of the 4.5 eV peak for several polymorphs of SiC (a) and for the C face 4H SiC annealed at various temperatures complemented by the spectra of annealed graphene obtained in this work (b). The dielectric functions of SiC polymorphs were taken from [141] and that of intercalated at different temperatures from [144].

$\sim$ 800 meV in [158]. The peak shifts further with increasing number of layers, eventually reaching the known graphite value of 4.5 eV. Apparently, the peak position also depends on the polymorph of the SiC substrate, as was indicated in a report examining epitaxial graphene grown on Si-face 3C and Si-/C-face 4H. There is a clear indication showing that the peak in ϵ_2 tends to shift below 4.5 eV in C-face and to higher energy in Si-face case (Fig. 5.6 (a), [141]). Besides that, there is an inverse dependence between the substrate annealing temperature and the peak position, as was shown by examining graphene produced on C-face 4H substrate (Fig. 5.6 (b), [144]). In this regard, our findings would be consistent with the reports, in particular concerning the Si-face on which the graphene was grown. On the other hand, intercalation should suppress bonding with the substrate. The blue-shift might be related to the effect of intercalation itself. As a matter of fact, the charge carriers present in the substrate may lead to screening

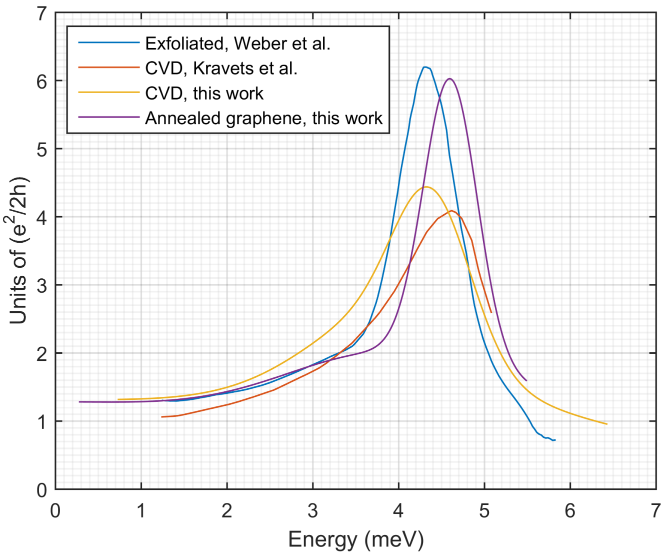

Figure 5.7: Real part of the optical conductivity of epitaxial graphene and its comparison with other types of graphene. The conductivity of exfoliated grpahene by Weber et al. was calculated from [133] and that of CVD graphene by Kravets et al. from [132].

between graphene and the substrate material. The distinction is evident when comparing insulating and conducting substrates such as silicon/quartz vs copper. In samples with metallic substrates, the shift of the peak, as compared to the single-particle prediction, is weaker, yielding the peak energy of 4.8-4.9 eV. Screening also affects the peak shape: without any, the peak is asymmetric with higher value below the critical point; with a high degree of screening, the peak becomes more symmetric [135, 159]. The sharpness of the peak thus confirms good quality of the sample. Even though intercalation reduces bonding between the layers, hydrogen atoms close to graphene might induce electrostatic interactions and doping of graphene layer, resulting in the blue-shift.

To make better comparison with literature in terms of optical conductivity, we calculated the real part of sheet optical conductivity. How to relate the 3D (bulk) and 2D (sheet) cases? For a bulk material, doubling its volume by increasing the thickness would accordingly double the total resistance. Similarly, if a bulk resistance is normalised to some volume element, say m^3, then some chosen thin layer t would exhibit

$$R_{2D} = \frac{1}{t} R_{3D}. \tag{5.12}$$

Inverting the above relation, we can express it in terms of the conductivity:

$$\sigma_{2D} = t\sigma_{3D}. \tag{5.13}$$

It reveals an additional fundamental feature of graphene. Namely, it should exhibit a universal value of conductivity $\sigma_0 = e^2/2h$ at IR energies [62, 63]. In Fig. 5.7, we compare the resulting optical conductivity with two cases from literature, exfoliated [133] and CVD graphene [134], as well as the CVD sample. Apart from higher conductivity values at UV energies arising from interband transitions, the conductivity of the investigated sample approaches unity and closely resembles exfoliated graphene at energies below 3 eV.

To summarize, the overall spectral dependence of the dielectric function from infrared to visible energies, narrowness and the magnitude of the main peak, and approaching the universal value of optical conductivity at IR energies allows us to conclude that annealing and intercalation of the (0001) surface of 6H-SiC allows to produce large-area excellent quality graphene monolayers. The investigated sample is very close to those prepared by exfoliation from the optical point of view. The spectral dependence of optical constants can be utilized in theoretical design of nano optoelectronic devices with graphene working in a broad spectral range.

Summary and conclusions

This thesis dealt with investigating the fundamental optical and magneto-optical properties of Dirac materials using spectroscopic techniques such as ellipsometry and Landau level spectroscopy. This allowed to probe their magneto-optical response in a nondestructive, contactless manner.

1) The first material was the lead tin salt $\mathrm{PbSn}_{1-x}\mathrm{Se}_x$ with a predicted non-trivial topological states under certain stoichiometric ratio and temperature conditions. A simple four-band theoretical model was presented to describe the main features of a system with massive Dirac states. It is able to characterize a given material with only 3 parameters capturing the fundamental solid-state crystal parameters such as the width of the bandgap, Fermi velocity and the diagonal dispersive term M that characterizes the topological regime (trivial or non-trivial, determined solely by its sign). The model was applied to IR measurement data of a series of $\mathrm{PbSn}_{1-x}\mathrm{Se}_x$ samples with different content of Sn. It allowed to determine the dependency of these essential physical parameters on the doping. It showed that interesting physical effects connected to the crossing of the bulk energy bands should manifest at fields between 50-150 T. This was beyond the achievable magnetic fields and mostly available in pulsed field experiments at the time.

An efficient and accurate algorithm was developed to simulate the infrared magneto-optical transmission of such a system. It allowed to investigate the influence of the broadening. The best match with observed experimental data was found with the broadening increasing linearly with the field, similar to an empirical rule deduced for interband Landau level excitations in graphene. The model also allowed to cross-check the carrier density values against those measured using electric transport technique, and in turn, determine the bulk Fermi energy dependence on sample parameters and magnetic field.

According to the extracted band structure parameters and our model, the surface states, if any, would be present at similar energies like the bulk states in most of the spectral region. They would only be clearly distinct at the lowest levels around the ground transitions of the bulk and the Reststrahlen band. A detailed examination of the magneto-optical spectra did not reveal any signs of the surface states, in contrast to other reports with similar materials under similar conditions. This result was attributed to a different occupation of the surface states (essentially, a band bending at the surface interface), disorder and finally, not perfect applicability of the proposed model to a random alloy which $\mathrm{Pb}_{1-x}\mathrm{Sn}_{1-x}\mathrm{Se}$ is.

2) Graphene was another investigated material. Owing to its potential impact to the electronics industry, it is important to identify a reliable and cheap manufacturing method for mass production. Graphitization of the top layers of SiC can offer such a bridge between desired sample quality and ease of manufacturing. Using spectroscopic ellipsometry, we have developed a geometrical model to describe a thin graphene layer positioned over a stepped bulk surface. We have also provided an effective Model Dielectric Function to describe the optical response over the entire visible and near-IR spectral region using three physical oscillators. The intercalation of the top layers of graphitized SiC can provide material with optical properties closest to that of an exfoliated graphene. Namely,

its narrowness and position of the main absorption peak are unrivaled compared to another popular CVD graphene.

Proposed further steps:

Dirac-like and nontrivial topological states of matter remain an interesting field of physics providing a playground for unusual spectral, electric and magnetic field dependencies of their physical parameters. The investigation presented in this thesis shows that both bulk and non-trivial states are, ironically, non-trivial to observe, even under conditions where they were reported by others. Therefore, to proceed with the research into those states, higher magnetic fields are required. This aspect is constantly pushed forward by institutions such as EMFL, and the required magnetic fields could be achieved in routine experiments in foreseeable future. On the other hand, another proposed approach is to try out a wider range of $\mathrm{PbSn}_{1-x}\mathrm{Se}_x$ stoichiometric configurations, such as $x > 0.33$, which might bring about the required conditions for the bulk (anti)crossing and surface states to appear even under the currently available experimental conditions. Band closure and reopening could be enforced by varying the ambient temperature for a given stoichiometric ratio (see for example fig. 2.5). All of these effects should manifest as features in observable IR spectra.

The conclusions of this thesis are the following:

- A four-band topological Hamiltonian was derived and allowed to describe all the essential features of the energy band structure in three parameters: gap, Fermi velocity and quadratic diagonal term M. The analysis allowed to extract these parameters as well as carrier concentration and the bulk Fermi energy with high precision for an array of $\mathrm{Pb}_{1-x}\mathrm{Sn}_x\mathrm{Se}$ samples with different tin content.

- Using band structure parameters and optical modelling, optimal conditions for unambiguous observation of the topologically protected surface states were determined. The window proved to be rather narrow, requiring magnetic fields of at least 20 T and a limited spectral range just above the reststrahlen band, between 75-100 meV. At higher energies, surface states overlap with the bulk states and become difficult to distinguish.

- Early onset of observable interband Landau level transitions at fields as low as 2 T indicated an excellent quality of the samples. Even these excellent conditions did not guarantee the appearance of the surface states, however. Their absence was attributed to i) different occupation factors than the bulk, ii) disorder in the surface states and iii) accuracy of theoretical models.

- A parametrised model dielectric function to describe epitaxial quasi-free-standing monolayer graphene on Si-face 6H-SiC permittivity has been provided over a spectral region from 0.150 to 5.5 eV.

- Its features, especially the narrowness and position of the main absorption peak located at 4.5 eV, suggests the optical properties of this graphene to be superior to those of CVD graphene, and also closest to the best quality exfoliated graphene.

References

[1] What is Topology? University of Waterloo, `https://uwaterloo.ca/pure-mathematics/about-pure-math/what-is-pure-math/what-is-topology` (checked 14th November 2022).

[2] Press release: The Nobel Prize in Physics 2016, the Nobel Foundation, `https://www.nobelprize.org/prizes/physics/2016/press-release/` (checked 11th November 2022).

[3] The Nobel Prize for Physics goes to topology – and mathematicians applaud, The Conversation Media Group Ltd, `https://theconversation.com/the-nobel-prize-for-physics-goes-to-topology-and-mathematicians-applaud-66532` (checked 11th November 2022).

[4] J. E. Avron, D. Osadchy, R. Seiler, A Topological Look at the Quantum Hall Effect, Phys.Today **56**(8), 38 (2003).

[5] C. Day, Quantum spin Hall effect shows up in a quantum well insulator, just as predicted, Phys.Today **61**(1) 19 (2008).

[6] C. L. Kane, E. J. Mele, Quantum Spin Hall Effect in Graphene, Phys.Rev.Lett. **95**, 226801 (2005).

[7] M. Franz, U-turns strictly prohibited, Nature **466**, 323 (2010).

[8] A. H. Castro Neto, F. Guinea, N. M. R. Peres, K. S. Novoselov, A. K. Geim, The electronic properties of graphene, Rev.Mod.Phys. **81** 109-162 (2009).

[9] P. R. Wallace, The Band Theory of Graphite, Phys.Rev. **71**(9), 622-634 (1947).

[10] X.-L. Qi, S.-C. Zhang, The quantum spin Hall effect and topological insulators, Phys.Today **63**(1) 33 (2010).

[11] M. Konig, S. Wiedmann, C. Brune, A. Roth, H. Buhmann, L. W. Molenkamp, X.-L. Qi, S.-C. Zhang, Quantum Spin Hall Insulator State in HgTe Quantum Wells, Science **318**, 766 (2007).

[12] D. Hsieh, D. Qian, L. Wray, Y. Xia, Y. S. Hor, R. J. Cava, M. Z. Hasan, A topological Dirac insulator in a quantum spin Hall phase, Nature **452** 970-974 (2008).

[13] L. Fu, Topological Crystalline Insulators, Phys.Rev.Lett. **106**, 106802-1 (2011).

[14] T. H. Hsieh , H. Lin, J. Liu, W. Duan, A. Bansil, L. Fu, Topological crystalline insulators in the SnTe material class, Nature **3**, 982 (2012).

[15] `http://www.nyu.edu/classes/tuckerman/quant.mech/lectures/lecture_7/node1.html`.

[16] `http://www.southampton.ac.uk/~stefano/courses/PHYS6011/relQM.pdf`.

[17] K. K. Tikuišis, J. Wyzula, L. Ohnoutek, P. Cejpek, K. Uhlířová, M. Hakl, C. Faugeras, K. Výborný, A. Ishida, M. Veis, M. Orlita, Landau level spectroscopy of the PbSnSe topological crystalline insulator, Phys. Rev. B **103**, 155304 (2021).

[18] E. A. Albanesi, E. L. Peltzer y Blanca, A. G. Petukhov, Calculated optical spectra of IV–VI semiconductors PbS, PbSe and PbTe, Comp.Mat.Sci. **32**(1) 85-95 (2005).

[19] Y. Pei, A. LaLonde, S. Iwanaga, G. J. Snyder, High thermoelectric figure of merit in heavy hole dominated PbTe, Energy Environ.Sci. **4**(6) 1929-2324 (2011).

[20] J. Wang, J. Hu, X. Sun, A. M. Agarwal, L. C. Kimerling, D. R. Lim, R. A. Synowicki, Structural, electrical, and optical properties of thermally evaporated nanocrystalline PbTe films, J.Appl.Phys. **104** 053707 (2008).

[21] K. Biswas, J. He, I. D. Blum, C.-I Wu, T. P. Hogan, D. N. Seidman, Vinayak P. Dravid, M. G. Kanatzidis, High-performance bulk thermoelectrics with all-scale hierarchical architectures, Nature **489** 414–418 (2012).

[22] J. P. Heremans, V. Jovovic, E. S. Toberer, A. Saramat, K. Kurosaki, A. Charoenphakdee, S. Yamanaka, G. J. Snyder, Enhancement of Thermoelectric Efficiency in PbTe by Distortion of the Electronic Density of States, Science **321** 554-557 (2008).

[23] S. N. Girard, J. He, X. Zhou, D. Shoemaker, C. M. Jaworski, C. Uher, V. P. Dravid, J. P. Heremans, M. G. Kanatzidis, High Performance Na-doped PbTePbS Thermoelectric Materials: Electronic Density of States Modification and Shape-Controlled Nanostructures, J.Am.Chen.Soc. **133** 16588-16597 (2011).

[24] X.-B. Li, P. Guo, Y.-N. Zhang, R.-F. Peng, H. Zhanga, L.-M. Liu, High carrier mobility of few-layer PbX (X = S, Se, Te), J.Mater.Chem.C **3** 6284 (2015).

[25] S. J. Oh, N. E. Berry, J.-H. Choi, E. A. Gaulding, T. Paik, S.-H. Hong, C. B. Murray, C. R. Kaga, Stoichiometric Control of Lead Chalcogenide Nanocrystal Solids to Enhance Their Electronic and Optoelectronic Device Performance, ACS Nano **7**(3) 2413-2421 (2013).

[26] M. Aerts, T. Bielewicz, C. Klinke, F. C. Grozema, A. J. Houtepen, J. M. Schins, L. D.A. Siebbeles, Highly efficient carrier multiplication in PbS nanosheets, Nat.Comm. **5** 3789 (2014).

[27] Z. Hens, D. Vanmaekelbergh, E. S. Kooij, H. Wormeester, G. Allan, C. Delerue, Effect of Quantum Confinement on the Dielectric Function of PbSe, Phys.Rev.Lett. **92** 026808 (2004).

[28] R. Dalven, A review of the semiconductor properties of PbTe, PbSe, PbS and PbO, Infrared Phys. **9** 141-184 (1969).

[29] K. B. Masood, P. Kumar, R A Singh, J. Singh, Odyssey of thermoelectric materials: foundation of the complex structure, J.Phys.Comm. /textbf2 062001 (2018).

[30] E. A. Albanesi, C. M. I. Okoye, C. O. Rodriguez, E. L. Peltzer y Blanca, A. G. Petukhov, Electronic structure, structural properties, and dielectric functions of IV-VI semiconductors: PbSe and PbTe, Phys.Rev.B **61**(24) 16589-16595 (2000).

[31] A. Delin, P. Ravindran, O. Eriksson, J. M. Willis, Full-Potential Optical Calculations of Lead Chalcogenides, Int.J.Quantum Chem. **69** 349-358 (1998).

[32] H. Wang, Y. Pei, A. D. LaLonde, G. J. Snyder, Heavily Doped p-Type PbSe with High Thermoelectric Performance: An Alternative for PbTe, Adv.Mat. **23** 1366-1370 (2011).

[33] N. Suzuki, K. Sawai, S. Adachi, Optical properties of PbSe, J.Appl.Phys. **77**(3) 1249-1255 (1995).

[34] J. N. Zemel, J. D. Jensen, R. B. Schoolar, Electrical and Optical Properties of Epitaxial Films of PbS, PbSe, PbTe, and SnTe, Phys.Rev. **140**(1A) A330-A343 (1965).

[35] G. Martinez, M. Schlüter, M. L. Cohen, Electronic structure of PbSe and PbTe II. Optical properties, Phys.Rev.B **11**(2) 660-670 (1975).

[36] G. Martinez, M. Schlüter, M. L. Cohen, Electronic structure of PbSe and PbTe. I. Band structures, densities of states, and effective masses, Phys.Rev.B **11**(2) 651-659 (1975).

[37] C. E. Ekuma, D. J. Singh, J. Moreno, M. Jarrell, Optical properties of PbTe and PbSe, Phys.Rev.B. **85** 085205 (2012).

[38] V. H. Krebs, K. Grun, D. Kallen, Mischkristallsysteme zwischen halbleitenden Chalkogeniden der vierten Hauptgruppe, ZAAC **312**(5-6) 307-313 (2004).

[39] A. J. Strauss, Inversion of Conduction and Valence bands in $\mathrm{Pb}_{1-x}\mathrm{Sn}_x\mathrm{Se}$ Alloys, Phys.Rev. **157**(3) 608-611 (1967).

[40] G. Krizman, B. A. Assaf, T. Phuphachong, G. Bauer, G. Springholz, L. A. de Vaulchier, Y. Guldner, Dirac parameters and topological phase diagram of $\mathrm{Pb}_{1-x}\mathrm{Sn}_x\mathrm{Se}$ from magnetospectroscopy, Phys.Rev.B **98**, 245202 (2018).

[41] T. Phuphachong, B. A. Assaf, V. V. Volobuev, G. Bauer, G. Springholz, L.-A De Vaulchier, Y. Guldner, Dirac Landau Level Spectroscopy in $\mathrm{Pb}_{1-x}\mathrm{Sn}-x\mathrm{Se}$ and $\mathrm{Pb}_{1-x}\mathrm{Sn}_x\mathrm{Te}$ across the Topological Phase Transition: A Review, Crystals **7**(1), 29 (2017).

[42] J. O. Dimmock, I. Melngailis, A. J. Strauss, Band structure and laser action in $\mathrm{Pb}_x\mathrm{Sn}_{1-x}\mathrm{Te}$, Phys.Rev.Lett. **16**(26) 1193-1196 (1966).

[43] R. Grisar, D. Ball, H. M. Preier, A. K. Kar, Optical switching in PbSnSe at low temperature, Opt.Comm. **57**(2), 121-124 (1986).

[44] A. Ishida, K. Naruse, S. Nakashima, Y. Takano, S. Du, K. Hirakawa, Interband absorption in PbTe/PbSnTe-based type-II superlattices, Appl.Phys.Lett. **113**(7) 072103 (2018).

[45] A. Ishida, T. Yamada, T. Tsuchiya, Y. Inoue, T. Kita, Semimetallic properties of SnTe/PbSe type-II superlattices, Phys.Proc. **3** 1295-1298 (2010).

[46] P. Werle, F. Slemr, K. Maurer, R. Kormann, R. Mucke, B. Janker, Near- and mid-infrared laser-optical sensors for gas analysis, Opt.Las.Eng. **37** 101-114 (2002).

[47] K. V. Maremyanin, A. V. Ikonnikov, A. V. Antonov, V. V. Rumyantsev, S. V. Morozov, L. S. Bovkun, K. R. Umbetalieva, E. G. Chizhevskiy, I. I. Zasavitskiy, V. I. Gavrilenko, Long-wavelength injection lasers based on $\mathrm{Pb}_{1-x}\mathrm{Sn}_x\mathrm{Se}$ alloys and their use in solid-state spectroscopy, Semiconductors **49**(12) 1623-1626 (2015).

[48] K. K. Tikuišis, A. Dubroka, K. Uhlířová, F. Speck, T. Seyller, M. Losurdo, M. Orlita, M. Veis, Dielectric function of epitaxial quasi-freestanding monolayer graphene on Si-face 6H-SiC in a broad spectral range, Phys. Rev. Mat. **7**, 044201 (2023).

[49] K. S. Novoselov, A. K. Geim, S. V. Morozov, D. Jiang, Y. Zhang, S. V. Dubonos, I. V. Grigorieva, A. A. Firsov, Electric Field Effect in Atomically Thin Carbon Films, Science **306**, 666-669 (2004).

[50] K. I. Bolotin, K. J. Sikes, Z. Jiang, M. Klima, G. Fudenberg, J. Hone, P. Kim, H. L. Stormer, Ultrahigh electron mobility in suspended graphene, Solid State Commun. **146**, 351-355 (2008).

[51] C. Dean, A. Young, I. Meric, C. Lee, L. Wang, S. Sorgenfrei, K. Watanabe, T. Taniguchi, P. Kim, K. L. Shepard, J. Hone, Boron nitride substrates for high-quality graphene electronics, Nature Nanotech. **5**, 722–726 (2010).

[52] K. F. Mak, C. H. Lui, J. Shan, T. F. Heinz, Observation of an Electric-Field-Induced Band Gap in Bilayer Graphene by Infrared Spectroscopy, Phys. Rev. Lett. **102**, 256405 (2009).

[53] K. J. Tielrooij, L. Piatkowski, M. Massicotte, A. Woessner, Q. Ma, Y. Lee, K. S. Myhro, C. N. Lau, P. Jarillo-Herrero, N. F. van Hulst, F. H. L. Koppens, Generation of photovoltage in graphene on a femtosecond timescale through efficient carrier heating, Nat. Nanotechnol. **10**, 437-443 (2015).

[54] I. Khrapach, F. Withers, T. H. Bointon, D. K. Polyushkin, W. L. Barnes, S. Russo, M. F. Craciun, Novel Highly Conductive and Transparent Graphene-Based Conductors, Adv. Mater. **24**(21), 2844-2849 (2012).

[55] H. Kinoshita, I. Jeon, M. Maruyama, K. Kawahara, Y. Terao, D. Ding, R. Matsumoto, Y. Matsuo, S. Okada, H. Ago, Highly Conductive and Transparent Large-Area Bilayer Graphene Realized by MoCl5 Intercalation, Adv. Mat. **29**(41), 1702141 (2017).

[56] J. Zhou, Z. Ren, S. Li, Z. Liang, C. Surya, H. Shen, Semi-transparent Cl-doped perovskite solar cells with graphene electrodes for tandem application, Mat. Lett. 220, 82-85 (2018).

[57] R. W. Havener, Y. Liang, L. Brown, L. Yang, J. Park, Van Hove Singularities and Excitonic Effects in the Optical Conductivity of Twisted Bilayer Graphene, Nano Lett. **14**(6), 3353-3357 (2014).

[58] J. Yin, H. Wang, H. Peng, Z. Tan, L. Liao, L. Lin, X. Sun, A. L. Koh, Y. Chen, H. Peng, Z, Liu, Selectively enhanced photocurrent generation in twisted bilayer graphene with van Hove singularity, Nat.Commun. **7**, 10699 (2016).

[59] G. Li, A. Luican, J. M. B. Lopes dos Santos, A. H. Castro Neto, A. Reina, J. Kong, E. Y. Andrei, Observation of Van Hove singularities in twisted graphene layers, Nat.Phys. **6**, 109-113 (2010).

[60] T. Ando, Y. Zheng, H. Suzuura, Dynamical Conductivity and Zero-Mode Anomaly in Honeycomb Lattices, J.Phys.Soc.Jpn. **71**(5) 1318-1324 (2002).

[61] A. K. Geim, A. H. MacDonald, Graphene: Exploring carbon flatland, Phys.Today **60**(8) 35-41 (2007).

[62] L. A. Falkovsky, A. A. Varlamov, Space-time dispersion of graphene conductivity, Eur.Phys/J.B/ **56** 281-284 (2007).

[63] T. Stauber, N. M. R. Peres, A. K. Geim, Optical conductivity of graphene in the visible region of the spectrum, Phys.Rev.B **78** 085432 (2008).

[64] R. R. Nair, P. Blake, A. N. Grigorenko, K. S. Novoselov, T. J. Booth, T. Stauber, N. M. R. Peres, A. K. Geim, Fine Structure Constant Defines Visual Transparency of Graphene, Science **320**(5881) 1308 (2008).

[65] J. C. Slonczewski, P. R.Weiss, Band Structure of Graphite, Phys.Rev. **109**(2) 272-279 (1958).

[66] SPIE Optipedia, The Stokes polarisation Parameters, ¡`https://spie.org/publications/fg05_p12-14_stokes_polarisation_parameters`.

[67] SPIE Optipedia, The Poincaré Sphere, ¡`https://spie.org/publications/fg05_p10-11_poincare_sphere`.

[68] G. E. Jellison Jr, Ellipsometry (book chapter), Elsevier Academic Press 1999, p. 402-411.

[69] B. Johs, J. A. Woollam, C. M. Herzinger, J. N. Hilfiker, R. A. Synowicki, C.. L. Bungay, Overview of variable-angle spectroscopic ellipsometry (VASE): II. Advanced applications, Proc. SPIE 10294, Optical Metrology: A Critical Review, 1029404 (1999).

[70] J. A. Woollam, B. D. Johs, C, M. Herzinger, J. N. Hilfiker, R. A. Synowicki, C. L. Bungay, Overview of variable-angle spectroscopic ellipsometry (VASE): I. Basic theory and typical applications, Proc. SPIE 10294, Optical Metrology: A Critical Review, 1029402 (1999).

[71] H.. Fujiwara, Spectroscopic Ellipsometry: Principles and Applications, John Wiley & Sons (2007).

[72] H. G. Tompkins, J. N. Hilfiker, Spectroscopic Ellipsometry: Practical Application to Thin Film Characterization, Momentum Press (2016), p. 49-50.

[73] R, W. Collins, Measurement Technique of Ellipsometry. In: Fujiwara H., Collins R. (editors) Spectroscopic Ellipsometry for Photovoltaics. Springer Series in Optical Sciences vol 212., Springer International Publishing, Cham (2018), pp 19-58.

[74] I. D. Vagner, V. M. Gvozdikov, P. Wyder, Quantum mechanics of electrons in strong magnetic field, HIT Journal of Science and Engineering **3**(1), 5-55 (2006).

[75] LibreTexts, Chemistry, Introduction to Organic Spectroscopy, Infrared Spectroscopy, 4.3: Instrumentation, `https://chem.libretexts.org/Bookshelves/Organic_Chemistry/Book%3A_Introduction_to_Organic_Spectroscopy/04%3A_Infrared_Spectroscopy/4.03%3A_IR_Instrumentation`.

[76] IR Spectroscopy and FTIR Spectroscopy: How an FTIR Spectrometer Works and FTIR Analysis, `https://www.technologynetworks.com/analysis/articles/ir-spectroscopy-and-ftir-spectroscopy-how-an-ftir-spectrometer-works-and-ftir-analysis-363938`.

[77] Ocean Optics spectrometers, `https://www.oceaninsight.com/products/spectrometers/`.

[78] Hamamatsu mini-spectrometers, `https://www.hamamatsu.com/eu/en/product/optical-sensors/spectrometers/mini-spectrometer/selection-guide.html`.

[79] LibreTexts, Chemistry, Andre Clayborne and Vernon Morris, Physical Chemistry Laboratory, CHEM 174 Physical Chemistry Laboratory II: 14. Fourier Transform Infrared Spectroscopy (FTIR), `https://chem.libretexts.org/Courses/Howard_University/Howard%3A_Physical_Chemistry_Laboratory/14._Fourier_Transform_Infrared_Spectroscopy_%28FTIR%29`.

[80] M. Orlita, B. A .Piot, G. Martinez, N. K. Sampath Kumar, C. Faugeras, M. Potemski, C. Michel, E. M. Hankiewicz, T. Brauner, C. Drasar, S. Schreyeck, S. Grauer, K. Runner, C. Gould, C. Brune, L. W. Molenkamp, Magneto-Optics of Massive Dirac Fermions in Bulk Bi_2Se_3, Phys.Rev.Lett. **114**, 186401 (2015).

[81] Caltech, W. Herres, J. Gronholz, Understanding FTIR Data Processing, .

[82] D. L. Mitchell, R. F. Wallis, Theoretical Energy-Band Parameters for the Lead Salts, Phys. Rev. **151**(2), 581-595 (1966).

[83] G. Bauer, H. Pascher, W. Zawadzki, Magneto-optical properties of semimagnetic lead chalcogenides, Semicond. Sci. Technol. **7**, 703-723 1992.

[84] H. Zhang, C. Liu, X. Qi, X. Dai, Z. Fang, S.-C. Zhang, Topological insulators in Bi2Se3, Bi2Te3 and Sb2Te3 with a single Dirac cone on the surface, Nature Phys **5**, 438–442 (2009).

[85] C.-X Liu, X.-L. Qi, H. J. Zhang, X. Dai, Z. Fang, S.-C. Zhang, Model Hamiltonian for topological insulators, Phys. Rev. B **82**, 045122 (2010).

[86] O. Ly, D. M. Basko, Theory of electron spin resonance in bulk topological insulators Bi_2Se_3, Bi_2Te_3 and Sb_2Te_3, J. Phys. Condens. Matter **28**, 15508 (2016).

[87] J. P. Singh, R. K. Bedi, Tin selenide films grown by hot wall epitaxy, J.Appl.Phys. **68**, 2776-2779 (1990).

[88] S. Franchi, Molecular Beam Epitaxy: From Research to Mass Production, Chapter 1 - Molecular Beam Epitaxy: fundamentals, historical background and future prospects, Elsevier, pages 1-46 (2013).

[89] Molecular beam epitaxy (MBE), Zeljkovic Lab for Nanoscale Synthesis and Characterization of Quantum Materials, Boston College Department of Physics, `https://capricorn.bc.edu/wp/zeljkoviclab/research/molecular-beam-epitaxy-mbe/` (checked 2nd of November 2022).

[90] H. Sitter, A. Andreev, G. Matt, N. S. Sariciftci, How-wall-epitaxy - the method of choice for the growth of highly ordered organic epilayers, Mol.Cryst.Liq.Cryst. **385**, [171]51-[180]60 (2002).

[91] A. Lopez-Otero, How wall epitaxy, Thin Solid Films **49**, 3-57 (1978).

[92] Chemical Vapor Deposition Physics, MKS Instruments, `https://www.mks.com/n/cvd-physics` (checked 2nd of November 2022).

[93] Explained: chemical vapor deposition, MIT News, Massachusetts Institute of Technology, `https://news.mit.edu/2015/explained-chemical-vapor-deposition-0619` (checked 2nd of November 2022).

[94] P. Dziawa, B. J. Kowalski, K. Dybko, R. Buczko, A. Szczerbakow, M. Szot, E. Lusakowska, T. Balasubramanian, B. M. Wojek, M. H. Berntsen, O. Tjernberg, T. Story, Topological crystalline insulator states in $Pb_{1-x}Sn_xSe$, Nat.Mater. **11**, 1023 (2012).

[95] Electrons in SEM, Thermo Fisher Scientific Materials Science Learning Center, `https://www.thermofisher.com/lt/en/home/materials-science/learning-center/applications/sem-electrons.html` (checked 3rd of November 2022).

[96] EDX Analysis with SEM: How Does it Work?, Thermo Fisher Scientific, `https://www.thermofisher.com/blog/materials/edx-analysis-with-sem-how-does-it-work/` (checked 2nd November 2022).

[97] EDX Analysis and WDX Analysis, `https://www.eesemi.com/edxwdx.htm` (checked 2nd of November 2022).

[98] M. Scimeca, S. Bischetti, H. K. Lamsira, R. Bonfiglio, E. Bonanno, Energy Dispersive X-ray (EDX) microanalysis: A powerful tool in biomedical research and diagnosis, Eur.J.Histochem **62**(1), 2841 (2018).

[99] D. M. Korn, R. Braunstein, Reflectivity and Wavelength-Modulation-Derivative Reflectivity of $Pb_{1-x}Sn_xTe$, Phys.Rev.B **5**(12) 4837 (1972).

[100] H. Kanazawa, S. Adachi, Spectroscopic ellipsometry study of $Pb_{1-x}Eu_xSe$ ($0 \leq x \leq 0.45$), J.Appl.Phys. **86** 2611 (1999).

[101] C.-E. Blomqvist, P.-O. Nillson, Optical Properties of Epitaxial PbSe Films, Phys.Rev. **174**(3) 849-855 (1968).

[102] S. E. Kohn, P. Y. Yu, Y. Petroff, Y. R. Shen, Y. Tsang, M. L. Cohen, Electronic Band Structure and Optical Properties of PbTe, PbSe, and PbS, Phys.Rev.B **8**(4), 1477-1488 (1973).

[103] B. A. Assaf, T. Phuphachong, V. V. Volobuev, G. Bauer, G. Springholz, L.-A. de Vaulchier, Y. Guldner, Magnetooptical determination of a topological index, npj Quantum Mater. **2**, 26 (2017).

[104] G.Springholz, G.Bauer, Semiconductors, IV-VI, in Wiley Encyclopedia of Electrical and Electronics Engineering, edited by J. G. Webster (American Cancer Society, 2014), pp. 1–16.

[105] G. Bauer, Magnetooptical properties of iv–vi compounds, in Narrow Gap Semiconductors Physics and Applications, edited by W. Zawadzki (Springer, Berlin, 1980), pp. 427–446.

[106] B. A. Assaf, T. Phuphachong, V. V. Volobuev, A. Inhofer, G. Bauer, G. Springholz, L. A. de Vaulchier, Y. Guldner, Massive and massless Dirac fermions in $Pb_{1-x}Sn_xTe$ topological crystalline insulator probed by magneto-optical absorption, Sci.Rep. **6**, 20323 (2016).

[107] K. Murase, S. Shinomura, S. Takaoka, A. Ishida, H. Fujiyasu, On the type of superlattices in lead-tin-telluride system, Superlatt. Microstruct. **1**, 177 (1985).

[108] G. Krizman, B. A. Assaf, T. Phuphachong, G. Bauer, G. Springholz, L. A. de Vaulchier, Y. Guldner, Dirac parameters and topological phase diagram of $Pb_{1-x}Sn_xSe$ from magnetospectroscopy, Phys.Rev.B **98**, 245202 (2018).

[109] B. M. Wojek, P. Dziawa, B. J. Kowalski, A. Szczerbakow, A. M. Black-Schaffer, M. H. Berntsen, T. Balasubramanian, T. Story, O. Tjernberg, Band inversion and the topological phase transition in (Pb,Sn)Se, Phys.Rev.B **90**, 161202(R) (2014).

[110] B. A. Assaf, T. Phuphachong, E. Kampert, V. V. Volobuev, P. S. Mandal, J. Sanchez-Barriga, O. Rader, G. Bauer, G. Springholz, L. A. de Vaulchier, Y. Guldner, Negative Longitudinal Magnetoresistance from the Anomalous N=0 Landau Level in Topological Materials, Phys.Rev.Lett. **119**, 106602 (2017).

[111] M. Orlita, K. Masztalerz, C. Faugeras, M. Potemski, E. G. Novik, C. Brune, H. Buhmann, L. W. Molenkamp, Fine structure of zero-mode Landau levels in HgTe/Hg_xCd_{1-x}Te quantum wells, Phys.Rev.B **83**, 115307 (2011).

[112] G. Krizman, B. A. Assaf, M. Orlita, T. Phuphachong, G. Bauer, G. Springholz, G. Bastard, R. Ferreira, L. A. de Vaulchier, Y. Guldner, Avoided level crossing at the magnetic field induced topological phase transition due to spin-orbital mixing, Phys.Rev.B **980**, 161202(R) (2018).

[113] M. Orlita, C. Faugeras, R. Grill, A. Wysmolek, W. Strupinski, C. Berger, W. A. de Heer, G. Martinez, M. Potemski, Carrier Scattering from Dynamical Magnetoconductivity in Quasineutral Epitaxial Graphene, Phys.Rev.Lett. **107**, 216603 (2011).

[114] I. O. Nedoliuk, S. Hu, A. K. Geim, A. B. Kuzmenko, Colossal infrared and terahertz magneto-optical activity in a two-dimensional Dirac material, Nat.Nanotechnol. **14**, 756 (2019).

[115] Density Functional Theory, Synopsys Inc., `https://www.synopsys.com/glossary/what-is-density-functional-theory.html` (checked 9th November 2022).

[116] J. Coomer, Density functional theory for beginners, University of Exter Quantum systems and Nanomaterials group `http://newton.ex.ac.uk/research/qsystems/people/coomer/dft_intro.html` (checked 9th November 2022).

[117] P. Honenberh, W. Kohn, Inhomogeneous Electron Gas, Phys.Rev. **136**(3B) B864-B871 (1964).

[118] P. Blaha, K. Schwarz, F. Tran, R. Laskowski, G. K. H. Madsen, L. D. Marks, WIEN2k: An APW+lo program for calculating the properties of solids, J.Chem.Phys. **152** 074101 (2020).

[119] The Full Potential APW methods, WIEN2k, Institute of Materials Chemistry, TU Vienna `http://www.wien2k.at/lapw/index.html` (checked 9th November 2022).

[120] C. Ambrosch-Draxl, J. O. Sofo, Linear optical properties of solids within the full-potential linearized augmented planewave method, Comp.Phys.Commun. **175**(1), 1-14 (2006).

[121] P. Yeh, Optical Waves in Layered Media (Wiley, New Jersey, 2005).

[122] T. Zhan, X. Shi, Y. Dai, X. Liu, J. Zi, Transfer matrix method for optics in graphene layers, J.Phys.Conden.Matt. **25**, 215301 (2013).

[123] M. L. Sadowski, G. Martinez, M. Potemski, C. Berger, W. A. de Heer, Landau Level Spectroscopy of Ultrathin Graphite Layers, Phys. Rev. Lett. **97**, 266405 (2006).

[124] N. Bansal, Y. S. Kim, M. Brahlek, E. Edrey, S. Oh, Thickness-Independent Transport Channels in Topological Insulator Bi_2Se_3 Thin Films, Phys.Rev.Lett. **109** 116804 (2012).

[125] E. Frantzeskakis, S. V. Ramankutty, N. de Jong, Y. K. Huang, Y. Pan, A. Tytarenko, M. Radovic, N. C. Plumb, M. Shi, A. Varykhalov, A. de Visser, E. van Heumen, M. S. Golden, Trigger of the Ubiquitous Surface Band Bending in 3D Topological Insulators, Phys.Rev.X **7** 041041 (2017).

[126] M. Brahlek, N. Koirala, N. Bansal, S. Oh, Transport properties of topological insulators: Band bending, bulk metal-to-insulator transition, and weak anti-localization, Solid State Commun. **215-216**, 54-62 (2015).

[127] J. Linder, T. Yokoyama, A. Sudbø, Anomalous finite size effects on surface states in the topological insulator B_2Se_3, Phys.Rev.B **80** 205401 (2009).

[128] J. Liu, W. Duan, L. Fu, Two types of surface states in topological crystalline insulators, Phys.Rev.B **88** 241303(R) (2013).

[129] K. S. Novoselov, A. K. Geim, S. V. Morozov, D. Jiang, M. I. Katsnelson, I. V. Grigorieva, S. V. Dubonos, A. A. Firsov, Two-dimensional gas of massless Dirac fermions in graphene, Nature **438**, 197-200 (2005).

[130] K. S. Novoselov, D. Jiang, F. Schedin, T. J. Booth, V. V. Khotkevich, S. V. Morozov, A. K. Geim, Two-dimensional atomic crystals, Proc.Natl.Acad.Sci.USA **102** 10451-10453 (2005).

[131] A. Gray, M. Balooch, S. Allegret, S. De Gendt, W.-E Wang, Optical detection and characterization of graphene by broadband spectrophotometry, J. Appl. Phys. **104**, 053109 (2008).

[132] V. G. Kravets, A. N. Grigorenko, R. R. Nair, P. Blake, S. Anissimova, K. S. Novoselov, A.K . Geim, Spectroscopic ellipsometry of graphene and an exciton-shifted van Hove peak in absorption, Phys. Rev. B **81**, 155413 (2010).

[133] J. W. Weber, V. E. Calado, M. C. M. van de Sanden, Optical constants of graphene measured by spectroscopic ellipsometry, Appl. Phys. Lett. **97**, 091904 (2010).

[134] F. J. Nelson, V. K. Kamineni, T. Zhang, E. S. Comfort, J. U. Lee, A. C. Diebold, Optical properties of large-area polycrystalline chemical vapor deposited graphene by spectroscopic ellipsometry, Appl. Phys. Lett. **97**, 253110 (2010).

[135] M. Losurdo, M. M. Giangregorio, G. V. Bianco, P. Capezzuto, G. Bruno, How spectroscopic ellipsometry can aid graphene technology?, Thin Solid Films **571**(3), 389-394 (2014).

[136] O. Fursenko, M. Lukosius, G. Lupina, J. Bauer, C. Villringer, A. Mai, Development of graphene process control by industrial optical spectroscopy setup, Proc. SPIE **10330**, 1033017 (2017).

[137] F. Speck, M. Ostler, S. Besendörfer, J. Krone, M. Wanke, T. Seyller, Growth and Intercalation of Graphene on Silicon Carbide Studied by Low-Energy Electron Microscopy, Ann.Phys. **529**(11) 1700046 (2017).

[138] F. Speck, J. Jobst, F. Fromm, M. Ostler, D. Waldmann, M. Hundhausen, H.B. Weber, Th. Seyller, The quasi-free-standing nature of graphene on H-saturated SiC(0001), Appl. Phys. Lett. **99**, 122106 (2011).

[139] C. Riedl, C. Coletti, T. Iwasaki, A.A. Zakharov, U. Starke, Quasi-Free-Standing Epitaxial Graphene on SiC Obtained by Hydrogen Intercalation, Phys. Rev. Lett. **103**, 246804 (2009).

[140] K. V. Emtsev, A. Bostwick, K. Horn, J. Jobst, G. L. Kellogg, L. Ley, J. L. McChesney, T. Ohta, S. A. Reshanov, J. Rohrl, E. Rotenberg, A. K. Schmid, D. Waldmann, H. B. Weber, T. Seyller, Towards wafer-size graphene layers by atmospheric pressure graphitization of silicon carbide, Nature Mater. **8**, 203-207 (2009).

[141] A. Boosalis, T. Hofmann, V. Darakchieva, R. Yakimova, M. Schubert, Visible to vacuum ultraviolet dielectric functions of epitaxial graphene on 3C and 4H SiC polytypes determined by spectroscopic ellipsometry, Appl. Phys. Lett. **101**, 011912 (2012).

[142] I. Santoso, S. L. Wong, X. Yin, P. K. Gogoi, T. C. Asmara, H. Huang, W. Chen, A. T. S. Wee, A. Rusydi, Optical and electronic structure of quasi-freestanding multilayer graphene on the carbon face of SiC, Europhys. Lett. **108**, 37009 (2014).

[143] R. Yakimova, T. Iakimova, G. R. Yazdi, C. Bouhafs, J. Eriksson, A. Zakharov, A. Boosalis, M. Schubert, V. Darakchieva, Morphological and electronic properties of epitaxial graphene on SiC, Physica B **439**, 54-59 (2014).

[144] C. Bouhafs, V. Darakchieva, I. L. Persson, A. Tiberj, P. O. Å. Persson, M. Paillet, A.-A. Zahab, P. Landois, S. Juillaguet, S. Schöche, M. Schubert, R. Yakimova, Structural properties and dielectric function of graphene grown by high-temperature sublimation on 4H-SiC(000-1), J. Appl. Phys. **117**, 085701 (2015).

[145] F. Nelson, A. Sandin, D. B. Dougherty, D. E. Aspnes, J. E. Rowe, A. C. Diebold, Optical and structural characterization of epitaxial graphene on vicinal 6H-SiC(0001)–Si by spectroscopic ellipsometry, Auger spectroscopy, and STM, J. Vac. Sci. Technol. B **30**(4), 04E106 (2012).

[146] G. R. Yazdi, T. Iakimov, R. Yakimova, Epitaxial Graphene on SiC: A Review of Growth and Characterization, Crystals **6**(5), 53 (2016).

[147] K.-H. Lee, C. H. Park, B.-H. Cheong, K. J. Chang, First-principles study of the optical properties of SiC, Solid State Commun. **92**(11), 869-872 (1994).

[148] B. Adolph, K. Tenelsen, V. I. Gavrilenko, F. Bechstedt, Optical and loss spectra of SiC polytypes from ab initio calculations, Phys. Rev. B **55**(3), 1422-1429 (1997).

[149] S. Zollner, J. G. Chen, E. Duda, T. Wetteroth, S. R. Wilson, J. N. Hilfiker, Dielectric functions of bulk 4H and 6H SiC and spectroscopic ellipsometry studies of thin SiC films on Si, J. Appl. Phys. **85**, 8353 (1999).

[150] O. P. A. Lindquist, K. Järrendahl, H. Arwin, S. Peters, J.-T. Zettler, C. Cobet, N. Nesser, D. E. Aspnes, A. Henry, N. V. Edwards, Ordinary and extraordinary dielectric functions of 4H- and 6H-SiC in the .7 to 9.0 eV photon energy range, Mat. Rec. Soc. Symp. Proc. **640**, H5.24.1-6 (2001).

[151] S. Ninomiya, S. Adachi, Optical Constants of 6H–SiC Single Crystals, Jpn. J. Appl. Phys. **33** 2479-2482 (1994).

[152] C. Xie, P. Xu, F. Xu, H. Pan, Y. Li, First-principles studies of the electronic and optical properties of 6H–SiC, Physica B **336**(3-4), 284-289 (2003).

[153] D. A. G. Bruggeman, Berechnung verschiedener physikalischer Konstanten von heterogenen Substanzen. I. Dielektrizitätskonstanten und Leitfähigkeiten der Mischkörper aus isotropen Substanzen, Ann.Phys. **416**(7) 636-664 (1935).

[154] C. Millán, C. Santonja, M. Domingo, R. Luna, M. Á. Satorre, An experimental test for effective medium approximations (EMAs), A&A **628** A63 (2019).

[155] L. Yang, J. Deslippe, C.-H. Park, M. L. Cohen, S. G. Louie, Excitonic Effects on the Optical Response of Graphene and Bilayer Graphene, Phys. Rev. Lett. **103**, 186802 (2009).

[156] K. F. Mak, J. Shan, T. F. Heinz, Seeing Many-Body Effects in Single- and Few-Layer Graphene: Observation of Two-Dimensional Saddle-Point Excitons, Phys. Rev. Lett. **106**, 046401 (2011).

[157] Do.-H. Chae, T. Utikal, S. Weisenburger, H. Giessen, K. v. Klitzing, M. Lippitz, J. Smet, Excitonic Fano Resonance in Free-Standing Graphene, Nano Lett. 11(3), 1379-1382 (2011).

[158] Y.-C. Chang, C.-H. Liu, C.-H. Liu, Z. Zhong, T. B. Norris, Extracting the complex optical conductivity of mono- and bilayer graphene by ellipsometry, Appl. Phys. Lett. **140**, 261909 (2014).

[159] P. K. Gogoi, I. Santoso, S. Saha, S. Wang, A. H. C. Neto, K. P. Loh, T. Venkatesan, A. Rusydi, Optical conductivity study of screening of many-body effects in graphene interfaces, Europhys. Lett. **99**, 67009 (2012).

List of publications

Articles directly related to this thesis

- K. K. Tikuišis, A. Dubroka, K. Uhlířová, F. Speck, T. Seyller, M. Losurdo, M. Orlita, M. Veis, Dielectric function of epitaxial quasi-freestanding monolayer graphene on Si-face 6H-SiC in a broad spectral range, Phys. Rev. Mat. **7**, 044201 (2023).

- K. K. Tikuišis, J. Wyzula, L. Ohnoutek, P. Cejpek, K. Uhlířová, M. Hakl, C. Faugeras, K. Výborný, A. Ishida, M. Veis, M. Orlita, Landau level spectroscopy of the PbSnSe topological crystalline insulator, Phys. Rev. B **103**, 155304 (2021).

Other articles

- M. Veis, J. Minár, G. Steciuk, L. Palatinus, C. Rinaldi, M. Cantoni, D. Kriegner, K. K. Tikuišis, J. Hamrle, M. Zahradník, R. Antoš, J. Železný, L. Šmejkal, X. Marti, P. Wadley, R. P. Campion, C. Frontera, K. Uhlířová, T. Duchoň, P. Kužel, V. Novák, T. Jungwirth, K. Výborný, Band structure of CuMnAs probed by optical and photoemission spectroscopy, Phys. Rev. B **97**, 125109 (2018).

- K. K. Tikuišis, L. Beran, P. Cejpek, K. Uhlířová, J. Hamrle, M. Vaňatka, M. Urbánek, M. Veis, Optical and magneto-optical properties of permalloy thin films in 0.7-6.4 eV photon energy range, Mater. Des. **114**, 31-39 (2017).

Confernce presentations directly related to this thesis

- K. Tikuišis, Infrared magneto-spectroscopy of thin layer topological crystalline insulators (poster P41), EMFL Summer School: Science in High Magnetic Field, 26-30 September 2018, Arles, France.

- K. K. Tikuišis, L. Ohnoutek, M. Orlita, M. Hakl, A. Ishida, M. Veis, Magneto-optical properties of topological crystalline insulator $\mathrm{Pb_{0.75}Sn_{0.25}Se}$ (poster PS.1.003), 18th Joint European Magnetic Symposia (JEMS), 21-26 August 2016, Glasgow, United Kingdom.

Other conferences

- K. K. Tikuišis, L. Beran, P. Cejpek, K. Uhlířová, M. Urbánek, M. Vaňatka, M. Veis, Optical and magneto-optical interactions in permalloy thin and ultrathin films on Si substrates (poster), 20th International Conference on Magnetism (ICM), 5-10 July 2015, Barcelona, Spain.